



Contents lists available at ScienceDirect

Progress in Oceanography

journal homepage: www.elsevier.com/locate/pocean



Global observations of nonlinear mesoscale eddies

Dudley B. Chelton ^{*}, Michael G. Schlax, Roger M. Samelson

College of Oceanic and Atmospheric Sciences, 104 COAS Administration Building, Oregon State University, Corvallis, OR 97331-5503, United States

ARTICLE INFO

Article history:

Received 22 February 2010
Received in revised form 6 January 2011
Accepted 10 January 2011
Available online 28 January 2011



ABSTRACT

Sixteen years of sea-surface height (SSH) fields constructed by merging the measurements from two simultaneously operating altimeters are analyzed to investigate mesoscale variability in the global ocean. The prevalence of coherent mesoscale features (referred to here as “eddies”) with radius scales of O(100 km) is readily apparent in these high-resolution SSH fields. An automated procedure for identifying and tracking mesoscale features based on their SSH signatures yields 35,891 eddies with lifetimes ≥ 16 weeks. These long-lived eddies, comprising approximately 1.15 million individual eddy observations, have an average lifetime of 32 weeks and an average propagation distance of 550 km. Their mean amplitude and a speed-based radius scale as defined by the automated procedure are 8 cm and 90 km, respectively.

The tracked eddies are found to originate nearly everywhere in the World Ocean, consistent with previous conclusions that virtually all of the World Ocean is baroclinically unstable. Overall, there is a slight preference for cyclonic eddies. However, there is a preference for the eddies with long lifetimes and large propagation distances to be anticyclonic. In the southern hemisphere, the distributions of the amplitudes and rotational speeds of eddies are more skewed toward large values for cyclonic eddies than for anticyclonic eddies. As a result, eddies with amplitudes >10 cm and rotational speeds >20 cm s $^{-1}$ are preferentially cyclonic in the southern hemisphere. By contrast, there is a slight preference for anticyclonic eddies for nearly all amplitudes and rotational speeds in the northern hemisphere.

On average, there is no evidence of anisotropy of these eddies. Their average shape is well represented as Gaussian within the central 2/3 of the eddy, but the implied radius of maximum rotational speed is 64% smaller than the observed radius of maximum speed. In part because of this mismatch between the radii of maximum axial speed in the observations and the Gaussian approximation, a case is made that a quadratic function that is a very close approximation of the mode profile of the eddy (i.e., the most frequently occurring value at each radius) is a better representation of the composite shape of the eddies. This would imply that the relative vorticity is nearly constant within the interiors of most eddies, i.e., the fluid motion consists approximately of solid-body rotation.

Perhaps the most significant conclusion of this study is that essentially all of the observed mesoscale features outside of the tropical band 20°S – 20°N are nonlinear by the metric U/c , where U is the maximum circum-average geostrophic speed within the eddy interior and c is the translation speed of the eddy. A value of $U/c > 1$ implies that there is trapped fluid within the eddy interior. Many of the extratropical eddies are highly nonlinear, with 48% having $U/c > 5$ and 21% having $U/c > 10$. Even in the tropics, approximately 90% of the observed mesoscale features are nonlinear by this measure.

Two other nondimensional parameters also indicate strong degrees of nonlinearity in the tracked eddies. The distributions of all three measures of nonlinearity are more skewed toward large values for cyclonic eddies than for anticyclonic eddies in the southern hemisphere extratropics but the opposite is found in the northern hemisphere extratropics. There is thus a preference for highly nonlinear extra-tropical eddies to be cyclonic in the southern hemisphere but anticyclonic in the northern hemisphere.

Further evidence in support of the interpretation of the observed features as nonlinear eddies is the fact that they propagate nearly due west with small opposing meridional deflections of cyclones and anticyclones (poleward and equatorward, respectively) and with propagation speeds that are nearly equal to the long baroclinic Rossby wave phase speed. These characteristics are consistent with theoretical expectations for large, nonlinear eddies. While there is no apparent dependence of propagation speed on eddy polarity, the eddy speeds relative to the local long Rossby wave phase speeds are found to be about 20% faster in the southern hemisphere than in the northern hemisphere. The distributions of the propagation directions of cyclones and anticyclones are essentially the same, except mirrored about a central azimuth

* Corresponding author. Tel.: +1 541 737 4017; fax: +1 541 737 2064.

E-mail address: chelton@coas.oregonstate.edu (D.B. Chelton).

angle of about 1.5° equatorward. This small, but we believe statistically significant, equatorward rotation of the central azimuth may be evidence of the effects of ambient currents (meridional advection or the effects of vertical shear on the potential vorticity gradient vector) on the propagation directions of the eddies.

While the results presented here are persuasive evidence that most of the observed westward-propagating SSH variability consists of isolated nonlinear mesoscale eddies, it is shown that the eddy propagation speeds are about 25% slower than the westward propagation speeds of features in the SSH field that have scales larger than those of the tracked eddies. This scale dependence of the propagation speed may be evidence for the existence of dispersion and the presence of features that obey linear Rossby wave dynamics and have larger scales and faster propagation speeds than the nonlinear eddies. The amplitudes of these larger-scale signals are evidently smaller than those of the mesoscale eddy field since they are not easily isolated from the energetic nonlinear eddies.

© 2011 Elsevier Ltd. All rights reserved.

1. Introduction

High-resolution sea-surface height (SSH) fields constructed by merging measurements from two simultaneously operating altimeters (Ducet et al., 2000; Le Traon et al., 2003) have revealed that **SSH variability is dominated by westward-propagating nonlinear mesoscale eddies throughout most of the World Ocean** (Chelton et al., 2007). Prior to the availability of this merged dataset, interpretations of westward-propagating SSH variability were based on SSH fields constructed from TOPEX/Poseidon (T/P) data alone. The ground track spacing of the T/P orbit was too coarse to resolve the mesoscale variability that is evident in the merged altimeter dataset. The merged dataset is thus enabling observational studies of mesoscale ocean variability that were not previously possible using altimetry data. This investigation extends the global analysis of 10 years of these high-resolution SSH fields by Chelton et al. (2007) to include an additional 6 years of data, and presents a refined and more comprehensive summary of the characteristics of the observed mesoscale eddies detected using an improved eddy identification and tracking procedure.

While it is arguably a matter of semantics, the terminology adopted here refers to features that obey linear dynamics, perhaps modified by ambient conditions of mean flow or bottom topography, as Rossby waves. The term eddy is reserved for the coherent mesoscale features that are the focus of this study, which are shown in Section 6.1 to have maximum rotational fluid speeds U that exceed their translation speed c , and are therefore characterized by an advective nonlinearity ratio $U/c > 1$. The possible alternative terminology “nonlinear wave” for these features is purposely avoided in order to emphasize the distinction from linear waves. The mesoscale features for which $U/c > 1$ can advect a parcel of trapped fluid as they translate.

From an historical perspective, it is important to note that westward-propagating SSH variability could not be unambiguously identified by satellite altimetry prior to the launch of T/P. The T/P orbit was carefully designed to minimize the effects of tidal aliasing, thus allowing the detection of westward propagating features without the aliased tidal errors that contaminated SSH fields constructed from measurements from the Geosat altimeter that preceded T/P (Schlax and Chelton, 1994a,b, 1996; Parke et al., 1998). It was evident from the first few years of the SSH fields from T/P that westward propagation is nearly ubiquitous in the World Ocean (Chelton and Schlax, 1996), confirming the conclusions from previous analyses of upper-ocean thermal observations in the North Pacific during the 1970s and 1980s (see Fig. 9 of Fu and Chelton, 2001). Subsequent global analyses from a 10-year T/P data record (Fig. 14 of Fu and Chelton, 2001) and from the 16-year merged dataset analyzed in this study (see Section 7.2 and Fig. 22 below) have validated the strong tendency for westward propagation of SSH variability and fine-tuned the estimates of the propagation speeds.

The qualitative similarity between the latitudinal variation of the observed westward propagation speeds and the phase speeds expected for long baroclinic Rossby waves has led to widespread interpretation of the westward propagation as linear Rossby waves. Close scrutiny reveals that the propagation speeds outside of the tropics are somewhat faster than predicted by the classical theory for Rossby waves (Chelton and Schlax, 1996; Fu and Chelton, 2001, and references therein; Osychny and Cornillon, 2004, and numerous subsequent studies; see also Section 7.2 and Fig. 22 below). This has inspired numerous theoretical studies to understand the dynamics responsible for the speedup. While the relevance of these theories to the nonlinear mesoscale features that are shown here and by Chelton et al. (2007) to dominate the SSH variability is unclear, these theoretical studies have led to important improvements in the understanding of the dynamical effects of ambient conditions on Rossby waves. In particular, it has been shown that much of the discrepancy between the observed westward propagation speeds and those predicted by the classical theory may be accounted for by the vertical shear of background mean currents (e.g., Killworth et al., 1997; Dewar, 1998; de Szoeke and Chelton, 1999; Liu, 1999; Yang, 2000; Colin de Verdière and Tailleux, 2005), small-scale bottom roughness (Tailleux and McWilliams, 2001) or the combined effects of vertical shear and variable large-scale bottom topography (Killworth and Blundell, 2004, 2005, 2007).

To date, little attention has been paid to other inconsistencies between the observations and classical Rossby wave theory. In particular,

- (1) It was apparent even from the T/P data that the observed westward-propagating SSH over most of the ocean (especially poleward of about 20° of latitude) was dominated by “blobby” structures rather than the latitudinally β -refracted continuous crests and troughs that are expected for long Rossby waves and are sometimes evident in the altimeter data.
- (2) The observed variability comprises a broad continuum of time and space scales, with little or no evidence in most regions of a spectral peak at the annual period that might have been expected for long Rossby waves forced by the strong annual cycles of wind and thermal forcing and has been sought in numerous past studies.
- (3) There is little evidence in the time-longitude structure of SSH variability for the dispersion expected for linear Rossby waves; the blobby features propagate westward for long distances as coherent structures.
- (4) There is little evidence for the meridional propagation expected for Rossby waves with the finite meridional scales of the blobby structures apparent in the SSH fields.

These characteristics are all consistent with the conclusion of Chelton et al. (2007) that the westward propagating variability

consists mostly of nonlinear eddies rather than linear Rossby waves. The focus on Rossby wave interpretations in earlier studies was a consequence of the coarse resolution of SSH fields constructed from T/P data alone (see the top panel of Fig. 1 and [Appendix A.1](#)). The distinction between linear Rossby waves and nonlinear eddies is important since the latter can transport water parcels and their associated physical, chemical and biological properties, while linear Rossby waves cannot. Eddies can thus have important influences on heat and momentum fluxes and on marine ecosystem dynamics.

The SSH fields analyzed here span the 16-year period 14 October 1992 through 31 December 2008 and were constructed by SSALTO/DUACS at 7-day intervals on a Mercator grid with a nominal spacing of $1/3^\circ$ using measurements from two simultaneously operating altimeters, one in a 10-day exact repeat orbit (T/P, followed by Jason-1 and presently by Jason-2) and the other in a 35-day exact repeat orbit (ERS-1 followed by ERS-2 and presently by Envisat). The SSALTO/DUACS processing (see [Appendix A.2](#)) includes removal of the 7-year mean SSH (1993–1999) to eliminate the unknown geoid. These SSH fields are distributed and referred to by AVISO as the “Reference Series.” (See the Acknowledgments for definitions of the above acronyms associated with the dataset analyzed here.) The analysis presented here is based on the version of this Reference Series that was available in early 2010 and included SSH fields for the 14 October 1992–31 December 2008 time period (see the footnote in [Appendix A.2](#)). Except in the left panels of [Fig. A3](#) in [Appendix A.3](#) for reasons explained in the caption, the analysis presented here is based on the anomaly SSH fields that were interpolated by SSALTO/DUACS from their $1/3^\circ$ Mercator grid onto a globally uniform $1/4^\circ$ latitude by $1/4^\circ$ longitude grid.

It is shown in [Appendix A.3](#) that the objective analysis procedure used to construct the SSH fields of the AVISO Reference Series has half-power filter cutoff wavelengths of about 2° in latitude by 2° in longitude. For eddies with Gaussian shape, this corresponds approximately to an e-folding radius of about 0.4° , or roughly 40 km (see [Appendix A.3](#)). Even a cursory comparison of the SSH fields of the AVISO Reference Series with the low-resolution SSH fields from T/P data alone reveals a fundamentally different perspective on the nature of SSH variability ([Fig. 1](#)). The T/P data resolve only very large scales while the SSH fields of the AVISO Reference Series are rich in mesoscale cyclonic and anticyclonic features (negative and positive SSH, respectively) with $0(100 \text{ km})$ radius scales that are too small to be detected by the T/P sampling pattern, except when these features are near the crossovers of ascending and descending ground tracks. The eddy detection algorithm developed and applied to the AVISO dataset for this study ([Appendix B.2](#)) identifies 3291 mesoscale eddies in [Fig. 1](#) alone, 2398 of which were trackable for 4 weeks or longer. This is typical of the number of eddies that are detectable and trackable at any given time in this dataset.

We note that AVISO also provides SSH fields with higher accuracy and potentially higher resolution than the Reference Series analyzed here. These fields, referred to by AVISO as the “Updated Series,” were constructed from measurements by all of the altimeters available at any given time. The most well-sampled time period is the 3-year period October 2002 through September 2005 during which four altimeters were operating simultaneously (Jason-1, T/P in an orbit interleaved with the Jason-1 ground tracks, Envisat and Geosat Follow-On). While three altimeters were operating simultaneously at various other times during the 16-year data record analyzed here, only two altimeters were operating most of the time, in which case the SSH fields of the Updated Series are identical to those of the Reference Series. The superiority of the SSH fields of the Updated Series when more than two altimeters were in operation has been demonstrated by [Pascual et al. \(2006\)](#). For the purpose of this investigation, however, the

homogeneous resolution of the SSH fields of the AVISO Reference Series over the 16-year data record is preferable to the temporally varying resolution of the Updated Series. The potentially larger amplitudes and smaller scales (because of improved resolution) of eddies in the Updated Series during periods when more than two altimeters were operating could complicate the statistical analysis of mesoscale eddies presented here. A comparison of the results of this study with the eddy characteristics deduced from the Updated Series during periods of higher resolution SSH fields is deferred to a future investigation.

While it is visually apparent from the middle panel of [Fig. 1](#) that much of the SSH variability is composed of energetic mesoscale features, there is also evidence at latitudes lower than about 20° in the Pacific for the long crests and troughs that are expected for Rossby waves, distorted into westward-pointing chevron patterns by β refraction. Although they are relatively small in amplitude and are “speckled” by much more energetic mesoscale features, these telltale chevron patterns are identifiable across much of the South Pacific, arguably to latitudes as high as 50°S in the eastern, and possibly the central, part of the basin. In the North Pacific, they are less evident in the middle panel of [Fig. 1](#) because of an overall higher SSH in the northern hemisphere in this map, as expected from the steric effects of summertime heating of the upper ocean during the August time period of the map. Depending on the details of the filtering, the chevron patterns can become more evident in the eastern North Pacific as far north as about 50°N when the SSH fields are spatially high-pass filtered to remove the steric effects of large-scale heating and cooling (e.g., the one-dimensional zonal high-pass filtering used for [Fig. 1](#) of [Chelton et al., 2007](#)), but they generally do not penetrate more than about 2000 km westward from the eastern boundary in the North Pacific ([Fu and Qiu, 2002](#)). These chevron patterns are mostly eliminated with the two-dimensional high-pass filtering applied to isolate the mesoscale eddies for this investigation (bottom panel of [Fig. 1](#); see Section 2 for a description of this filtering).

The abundance of mesoscale features in the SSH fields of the AVISO Reference Series confirms globally the view of the ocean posited from regional field programs during the 1970s, referred to by [Wunsch \(1981\)](#) as the “decade of the mesoscale”. Observations in the western North Atlantic from the Mid-Ocean Dynamics Experiment (MODE Group, 1978) and POLYMODE ([McWilliams et al., 1983](#)) were interpreted as evidence that mid-ocean variability is dominated by mesoscale eddies (see also [Robinson, 1983](#)). Satellite altimetry has thus advanced to the point where observational studies of mesoscale dynamics that have been feasible only from regional in situ datasets can now be addressed globally from multiple satellite altimeters operating simultaneously, with the caveat that only the surface characteristics can be observed by altimetry.

This paper is organized as follows. The resolution of the SSH fields of the AVISO Reference Series and the automated eddy identification procedure developed for this study are summarized in Section 2; the details of the assessment of the resolution are given in [Appendix A](#) and the details of the eddy identification and tracking procedure and an assessment of the biases of the eddy amplitude estimates are presented in [Appendices B and C](#), respectively. Census statistics for the $\sim 36,000$ eddies with lifetimes of 16 weeks and longer identified and tracked in the 16-year data record by this automated procedure are presented in Section 3: their lifetimes, propagation distances, trajectories, geographical distributions, and polarities (cyclonic versus anticyclonic). The kinematic properties (amplitudes, scales, rotational speeds and estimated Rossby numbers) of these robust mesoscale eddies are summarized in Section 4 and the composite average eddy shape is investigated in Section 5. The nonlinearity of the mesoscale eddies is assessed in Section 6 from three different metrics, and their propagation

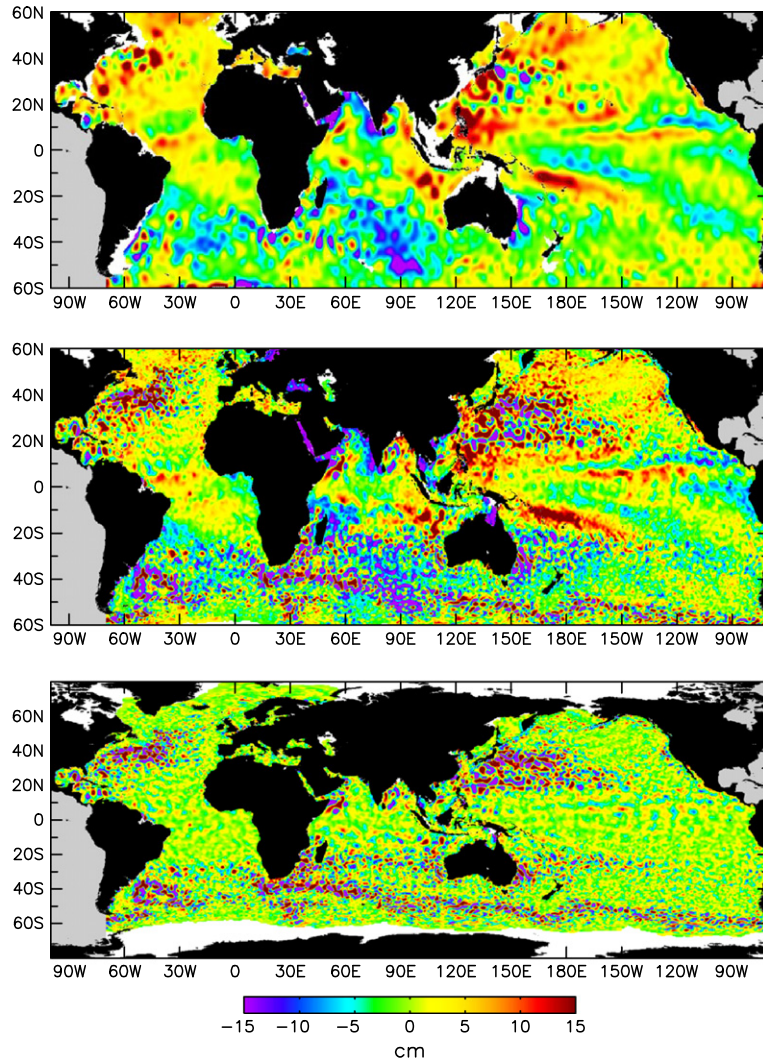


Fig. 1. An example of global maps of SSH on 28 August 1996 constructed from TOPEX/Poseidon (T/P) data only (top) and from the merged T/P and ERS-1 data in the AVISO Reference Series (middle). The bottom panel is the SSH field from the merged T/P and ERS-1 data after spatially high-pass filtering with half-power filter cutoffs of 20° of longitude by 10° of latitude. The automated procedure described in Appendix B.2 identifies 3291 eddies in the bottom panel, of which 2398 were trackable as described in Appendix B.4 for 4 weeks or longer.

characteristics (direction and speed) are summarized in Section 7. This wealth of information about mesoscale eddies deduced from the 16-year dataset is summarized in Section 8.

2. Feature resolution and automated eddy detection

It is shown in Appendix A.3 that features with wavelength scales shorter than 3° are attenuated in the SSH fields of the AVISO Reference Series analyzed in this study. The variance attenuation is about a factor of 2 at a wavelength of about 2° , which we interpret as the approximate half-power filter cutoff of the objective analysis procedure used to construct the AVISO fields. This filter cutoff wavelength can be expressed in terms of the approximate scales of the mesoscale features that can be resolved by considering an idealized eddy that has the form of a two-dimensional axisymmetric Gaussian, which is shown in Section 5 to be a reasonable approximation on average, at least over the central 2/3 of the eddies, and is adequate for present purposes. A wavelength resolution of 2° corresponds to a Gaussian eddy with an e-folding radius of about 0.4° (see Appendix A.3). We thus conclude that the SSH fields of the AVISO Reference Series have been filtered to attenuate Gaussian-like features with e-folding radii shorter than

roughly 40 km. It should be kept in mind, however, that only those features with e-folding radii larger than about 60 km are unattenuated by the filtering. (This is the e-folding scale of a Gaussian that corresponds to the 3° wavelength at which there is no attenuation of the SSH fields of the AVISO Reference Series.) The amplitudes of features with smaller e-folding radii are increasingly attenuated with decreasing scale; the amplitude attenuation (as opposed to variance attenuation) is about a factor of $2^{-1/2}$ at the e-folding radius of ~ 40 km.

The oceanic mesoscale can be characterized as consisting of variability with radius scales of 10–500 km. The lower end of the range of spatial scales of mesoscale variability is thus not addressable from the ~ 40 km feature resolution of the SSH fields analyzed here. The conclusions of this study are therefore restricted to mesoscale eddies with relatively large radii.

Evidence is presented in Appendix A.3 that the smoothing in the objective analysis procedure used to produce the SSH fields of the AVISO Reference Series (see Appendix A.2) may not be quite sufficient. The SSH variance in these fields is locally higher near the T/P crossovers where SSH variability is best resolved in the merged dataset, and lower in the centers of the diamonds formed by the T/P ground track pattern where SSH observations are limited to

just the altimeter in the 35-day repeat orbit (see the bottom panels of Fig. A1). These inhomogeneities in SSH variance from spatially varying resolution capability of the sampling pattern of the two simultaneously operating altimeters from which the SSH fields of the AVISO Reference Series are constructed can spuriously modulate estimates of the amplitude, radius and the location of the centroid of a propagating eddy (see, for example, Pascual et al., 2006), which can interrupt the tracking of the eddy. It is not possible to say how frequently this occurs in the 16-year global dataset analyzed here, but we believe that any such problems do not strongly influence the general conclusions of this study.

A new eddy identification procedure was developed for this study. As described in Appendix B.2, this procedure is based on defining the eddies in terms of SSH, thus obviating the need to differentiate the SSH fields and avoiding the associated deleterious effects of noise that are problematic in the procedure based on products of second derivatives of SSH in the Okubo-Weiss parameter (see Appendix B.1) that has been used in numerous previous studies, including Chelton et al. (2007). The assessment in Appendix A.3 of the filtering properties of the objective analysis procedure used to construct the SSH fields of the AVISO Reference Series that are analyzed in this study is incorporated into the SSH-based eddy identification and tracking procedure to set a minimum area for the mesoscale features that are tracked from one time step to the next. The new procedure yields significantly more eddies than found by Chelton et al. (2007) and these eddies have longer lifetimes (see Fig. B3). For the eddies with lifetimes of 16 weeks and longer that are the focus of this study (see Section 3.1), the new procedure yields about twice as many eddies. For lifetimes longer than a year, there are about five times more eddies in the new eddy dataset.

Automated detection and tracking of mesoscale features in the SSH fields is complicated by several factors. The most apparent of these is the presence of large-scale SSH variability from the steric effects of heating and cooling of the upper ocean that result in large-scale SSH variations that often mask the more subtle signatures of eddies, especially in the open ocean away from the regions of energetic mesoscale variability associated with unstable currents. While such signals occur on a wide range of time scales, they are dominated by the large-scale annual cycle of summertime heating and wintertime cooling. The effects of this annual steric heating and cooling are readily apparent from the hemispheric differences in large-scale sea level in the top and middle panels of Fig. 1 (high in the northern hemisphere and low in the southern hemisphere in these summertime maps). A cyclonic eddy (concave upward SSH) that is clearly identifiable during the wintertime can be more difficult to detect in summer when SSH is high over the entire ocean basin. Likewise, anticyclonic eddies can be more difficult to detect during the wintertime when SSH is low over the entire ocean basin. These difficulties are easily seen from time-longitude plots of SSH variability, in which the angled patterns associated with westward propagating eddies are interrupted annually by horizontal bands of zonally coherent and large-amplitude SSH fluctuations from seasonal heating and cooling (see, for example, Fig. 11 of Fu and Chelton, 2001). To facilitate eddy identification, the AVISO SSH fields were therefore spatially high-pass filtered in two dimensions to remove variability with wavelength scales larger than 20° of longitude by 10° of latitude. This filtering is very effective at removing steric heating and cooling effects, as well as other large-scale variability (compare the middle and bottom panels of Fig. 1). Analogous high-pass filtering has been applied in all previous investigations of westward-propagating SSH variability, although usually in the form of one-dimensional (zonal) filtering.

Other factors that limit the accuracy of eddy identification are more difficult to contend with. The most significant is the practical

difficulty of defining an eddy boundary. Since eddies are continually evolving, time-dependent fluid structures that do not have persistent, clearly demarcated boundaries, there is inevitably some arbitrariness both in the fundamental definition of an eddy structure and in the specific eddy boundaries defined by any automated procedure. Because of the mesoscale complexity of the SSH field that generally surrounds an identified eddy feature, SSH along the outer boundary of a compact feature as defined by the automated procedure usually has a non-zero value of SSH. As a consequence, the residual SSH fields after subtracting the eddy contributions to SSH within all of the defined eddy boundaries consists of “plateaus” of constant SSH across the interior of the eddy (locally higher than the ambient SSH for anticyclones and locally lower for cyclones). These plateaus are typically interconnected to the residual plateaus of other eddies by ridges and valleys that are part of the overall mesoscale variability, presumably arising from the spectral continuum of the up-scale energy cascade of geostrophic turbulence (e.g., Kraichnan, 1967; Batchelor, 1969; Charney, 1971; Rhines, 1975, 1979; Stammer, 1997; Scott and Wang, 2005). From a dynamical or kinematical standpoint, some or all of this residual variability should perhaps be more properly considered to be part of the eddy structures, although this would result in eddy boundaries with non-compact form. Exclusion of this residual SSH from the interiors of defined eddy perimeters thus introduces what arguably might be interpreted as bias in the estimated amplitudes of the tracked eddies.

The adequacy of the estimated amplitudes of the eddies obtained from the automated procedure described in Appendices B.2–B.4 is assessed in Appendix C. It is concluded that the above-noted mesoscale variability with non-compact form accounts for much of the SSH variance. Any eddy identification algorithm that defines eddies based on a conceptual notion of compact structures in SSH will therefore unavoidably leave much of the total SSH variance unaccounted for, even if each defined eddy-like feature encapsulates all of the SSH topography within the portion of the defined eddy that has compact form. The bias of the estimated amplitudes of the mesoscale features with compact form is shown in Appendix C to be usually less than 1 cm outside of the regions of most energetic mesoscale variability (see Figs. C2 and C3). The bias in regions of energetic mesoscale variability may sometimes be 1 or 2 cm, but only occasionally more than that, in the energetic regions.

3. Census statistics of mesoscale coherent structures

3.1. Eddy lifetimes and propagation distances

Global histograms and upper-tail cumulative histograms (i.e., the number of eddies with lifetimes greater than or equal to each particular value along the abscissa) of the eddy lifetimes are shown separately for cyclones and anticyclones in Fig. 2. In total, the automated procedure summarized in Appendices B.2–B.4 detected $\sim 177,000$ eddies with lifetimes of 4 weeks or longer over the 16-year data record; eddies with lifetimes shorter than 4 weeks were discarded. The eddy counts drop off rapidly with increasing lifetime. The numbers of eddies with lifetimes that exceeded 16, 26, 52, 78 and 104 weeks were 35,891, 17,252, 4396, 1494 and 620, respectively. There is a slight preference for cyclonic over anticyclonic eddies with lifetimes of 60 weeks or less (bottom left panel of Fig. 2). Eddies with lifetimes of 78 weeks and longer were preferentially anticyclonic. Overall, there were 6% more cyclones than anticyclones for lifetimes of 16 weeks and longer, but 21% more anticyclones than cyclones for lifetimes of 78 weeks and longer (bottom right panel of Fig. 2).

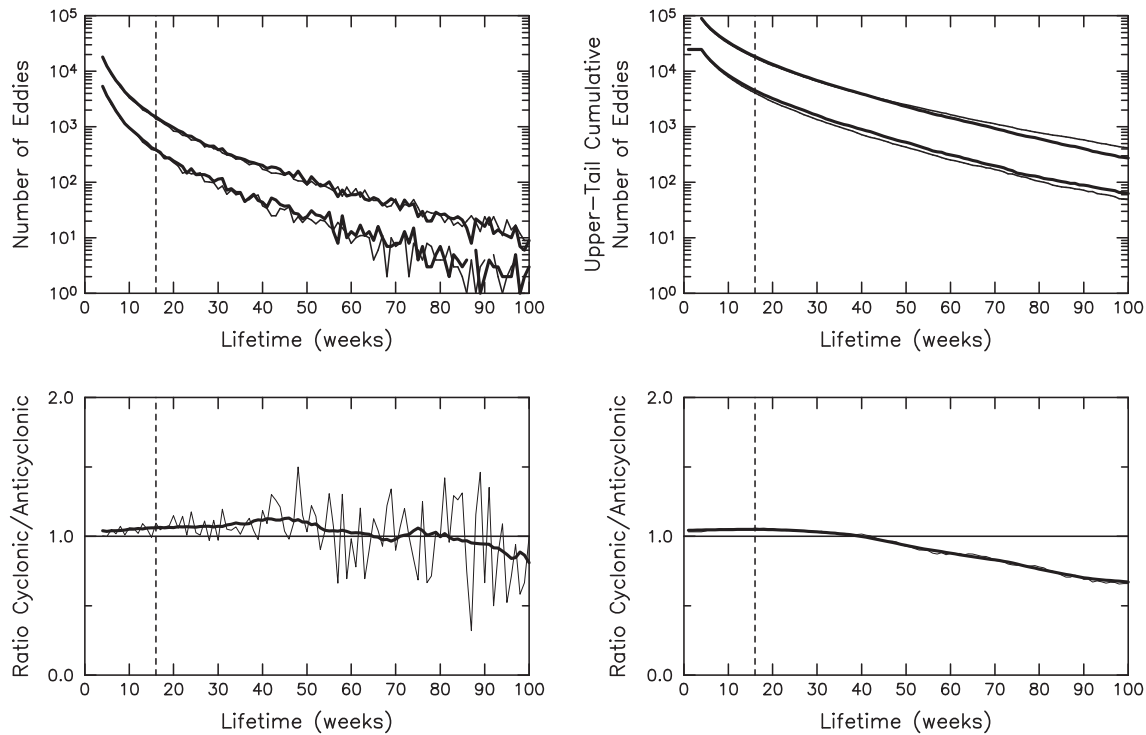


Fig. 2. Histograms (left) and upper-tail cumulative histograms (right) of the lifetimes of the cyclonic (upper thick lines) and anticyclonic (upper thin lines) eddies over the 16-year period October 1992–December 2008. The ratios of these histogram values are shown by the thin lines in the bottom panels and the thick lines in the bottom panels are 21-week running averages of the ratios. (The two lines are almost indistinguishable in the ratio of the upper-tail cumulative histograms.) The lower thick and thin lines in the top panels are, respectively, for only those cyclonic and anticyclonic eddies for which the net displacement was eastward. The vertical dashed lines indicate the 16-week lifetime cutoff for the eddies that are the focus of this study.

To alleviate concerns that imperfections of the detection and tracking procedure may affect the conclusions of this study, we focus attention on the robust eddies, which we define to be eddies with lifetimes of 16 weeks and longer. These ~36,000 eddies have an average lifetime of 32 weeks and their average propagation distance is 550 km. Histograms and upper-tail histograms of the eddy propagation distances for these eddies are shown separately for cyclones and anticyclones in Fig. 3. The eddy counts drop off rapidly with increasing propagation distance. The numbers of eddies with propagation distances that exceeded 500, 1000, 2000, 3000 and 4000 km were 13,211, 4886, 1066, 326 and 129, respectively. Consistent with the notion that eddy lifetime and propagation distance are correlated, there is a small preference for cyclones over anticyclones for propagation distances of 2500 km or less (bottom left panel of Fig. 3). Eddies that propagated longer distances were preferentially anticyclonic. Overall, there were 59% more anticyclones than cyclones with propagation distances of 3500 km and longer.

3.2. Eddy trajectories

More than 75% of the ~36,000 eddies analyzed here (Fig. 4a) propagated westward. The 8606 eddies that had a net eastward displacement (Fig. 4b) occurred primarily in the strong eastward Antarctic Circumpolar Current, the Gulf Stream and its extension northeast of Grand Banks, and in the region of confluence of the Kuroshio and Oyashio Currents and their eastward extensions. These regions of eastward propagation have previously been noted by Fu (2009), and were identified for the Antarctic Circumpolar Current region by Hughes et al. (1998). This is to be expected from advection of the eddies by the strong eastward currents in these regions. Histograms and upper-tail histograms of the lifetimes and propagation distances of the eastward propagating cyclonic and anticyclonic eddies are shown by the lower thick and thin

lines, respectively, in the top panels of Figs. 2 and 3. They account for about 25% of the tracked eddies with short lifetimes, decreasing to about 15% for the longest lifetimes (Fig. 2). The most notable characteristic of the eastward-propagating eddies is that they have much shorter propagation distances than the westward propagating eddies (Fig. 3). Fewer than 20 eddies of each polarity propagated eastward more than 1000 km and none propagated eastward more than 1800 km.

Except in some of the low-latitude regions, the high density of the eddy tracks in Fig. 4a obscures individual eddy trajectories. To see the propagation of individual eddies better, the eddy trajectories with successively longer minimum lifetimes of 26, 52, 78 and 104 weeks are shown in Figs. 4c–f. The numbers of eddies of each polarity are labeled at the top of each panel. The anticyclonic preferences for eddies with long lifetimes and large propagation distances are visually evident from Fig. 4e and f. Close inspection reveals that cyclones and anticyclones tend to have opposing small meridional deflections, poleward for cyclones and equatorward for anticyclones. As shown by Morrow et al. (2004), this phenomenon is most clearly evident off the west coasts of Australia, North America, and South Africa. It can also be seen off the west coast of South America. While more difficult to see in the mid-ocean regions because of the high density of eddy tracks, opposing meridional drifts of cyclones and anticyclones occur throughout the World Ocean. These meridional deflections are investigated in detail in Section 7.1.

3.3. Geographical distribution of the eddies

A census of the ~36,000 eddies with lifetimes ≥ 16 weeks that are analyzed here is shown in Fig. 5. The upper panel shows the number of eddy centroids that propagated across each $1^\circ \times 1^\circ$ region over the 16-year data record. Within the eddy-rich regions,

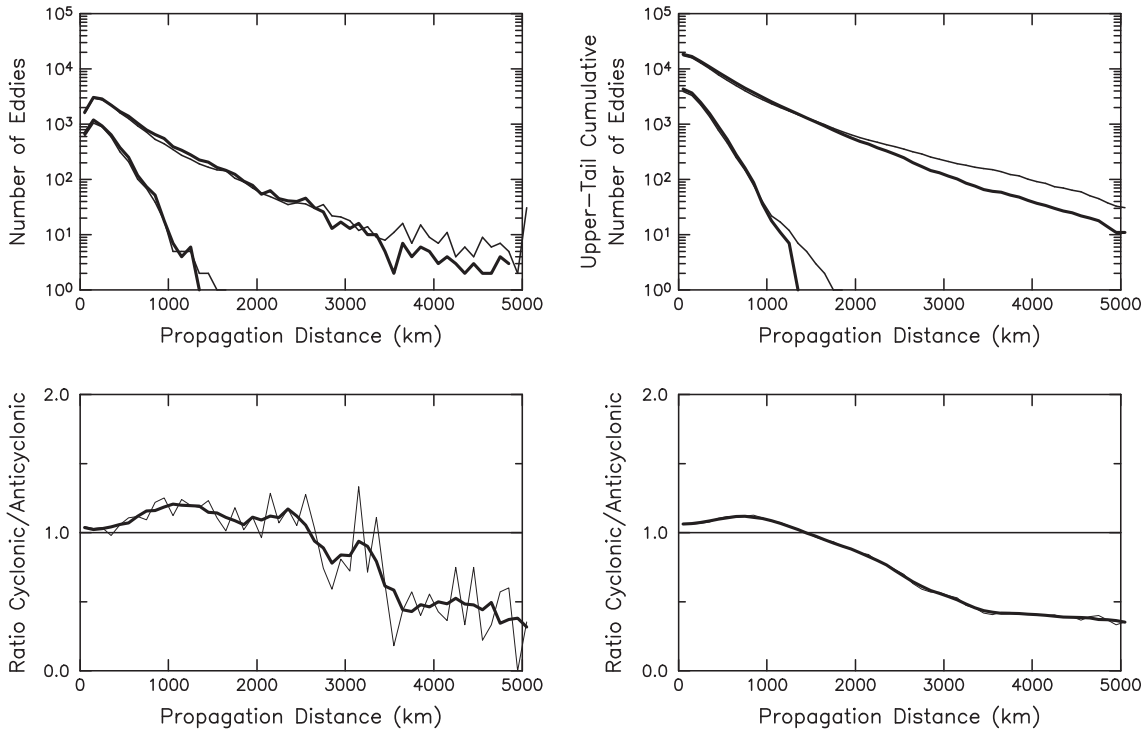


Fig. 3. Histograms (left) and upper-tail cumulative histograms (right) of the great-circle propagation distances of cyclonic (thick lines) and anticyclonic (thin lines) eddies with lifetimes ≥ 16 weeks over the 16-year period October 1992–December 2008. The ratios of these histogram values are shown by the thin lines in the bottom panels and the thick lines in the bottom panels are 500-km running averages of the ratios. (The two lines are almost indistinguishable in the ratio of the upper-tail cumulative histograms.) The lower thick and thin lines in the top panels are, respectively, for only those cyclonic and anticyclonic eddies for which the net displacement was eastward.

about 15–30 eddy centroids were typically observed, i.e., about one to two per year, on average. Almost no eddy centroids were observed in the regions centered at about 50°N, 160°W in the northeast Pacific and at about 50°S, 95°W in the southeast Pacific. These “eddy deserts” have been noted previously by Chelton et al. (2007). If eddies exist in these regions, their amplitudes or scales are too small to be detected and tracked or their lifetimes were shorter than the minimum 16-week lifetime considered here.

A notable feature of the upper panel of Fig. 5 is the small number of eddies observed throughout the equatorial region. The spatial scales of eddies and eddy-like features at these low latitudes are large because of the large Rossby radius of deformation (see the right panel of Fig. 12 below). As represented in the SSH fields of the AVISO Reference Series, the SSH topography within the interiors of these large-scale features often consists of considerable small-scale irregularity with small amplitude, likely due at least in part to noise in these SSH fields constructed from two simultaneously operating altimeters (Pascual et al., 2006; see also the bottom panels of Fig. A1 and the related discussion in Appendix A.3). As a consequence, the automated procedure described in Appendix B.2 often identifies multiple small eddies within the interiors of the large low-latitude features. In combination with the observed rapid evolution of the irregular SSH topography (again suggestive of noise) and the fast westward propagation of the large-scale features at these low latitudes, this poses difficult challenges for automated eddy identification and tracking procedures. The procedure described in Appendix B.2 could be modified to track only the large-scale aspects of the features that are of interest at these low latitudes (e.g., tropical instability waves) but this is deferred to a future study. The emphasis here is therefore on mesoscale variability at latitudes higher than about 10° at which propagation speeds and irregularities in the SSH topography within eddy interiors are less problematic for automated eddy identification and tracking.

The eddy centroid census in the upper panel of Fig. 5 is a conservative estimate of the number of eddies that influence SSH at

any given location. The lower panel shows the census of eddy interiors that propagated across every 1° × 1° region during the 16-year data record. The interiors are defined here to be the portion of each identified eddy within the closed contour of SSH around which the average geostrophic speed is maximum (see Appendix B.3), which corresponds approximately to a contour of zero relative vorticity. On average, this speed-based eddy scale is about 70% of the effective radius of the area enclosed by the eddy boundary as defined by the automated eddy identification procedure (see Fig. B2b). The geographical pattern of the census of eddy interiors is very similar to that of the census of eddy centroids. The number of tracked eddies during the 16-year data record that influence SSH within any particular 1° × 1° region is four to six eddies per year, on average, in the eddy-rich regions, i.e., about three times larger than the number of eddy centroids that propagate through the region as shown in the top panel of Fig. 5.

The reduced number of eddies along the axes of the Gulf Stream, the Agulhas Return Current, and the Kuroshio Extension (especially the latter two) that is evident in Fig. 5 is noteworthy. Comparatively large numbers of eddies occurred in bands that straddle both sides of the cores of these jet-like currents, presumably from the shedding of eddies in the form of detached meanders on both sides of the meandering currents. The mesoscale variability within the cores of the currents consists mostly of meanders of the jet-like currents rather than isolated vortices. Because the analysis is performed on 20° × 10° spatially high-pass filtered anomaly SSH, meanders resemble vortices in any particular snapshot. Unlike coherent vortices, however, the shapes of meanders in the anomaly SSH fields can deviate from the compact forms assumed by our eddy identification procedure. Moreover, they can evolve more rapidly in time and may therefore not be trackable for the minimum lifetime of 16 weeks for the mesoscale features analyzed in this study. For both of these reasons, the numbers of tracked eddies are somewhat lower in the cores of the jet-like currents than on their flanks.

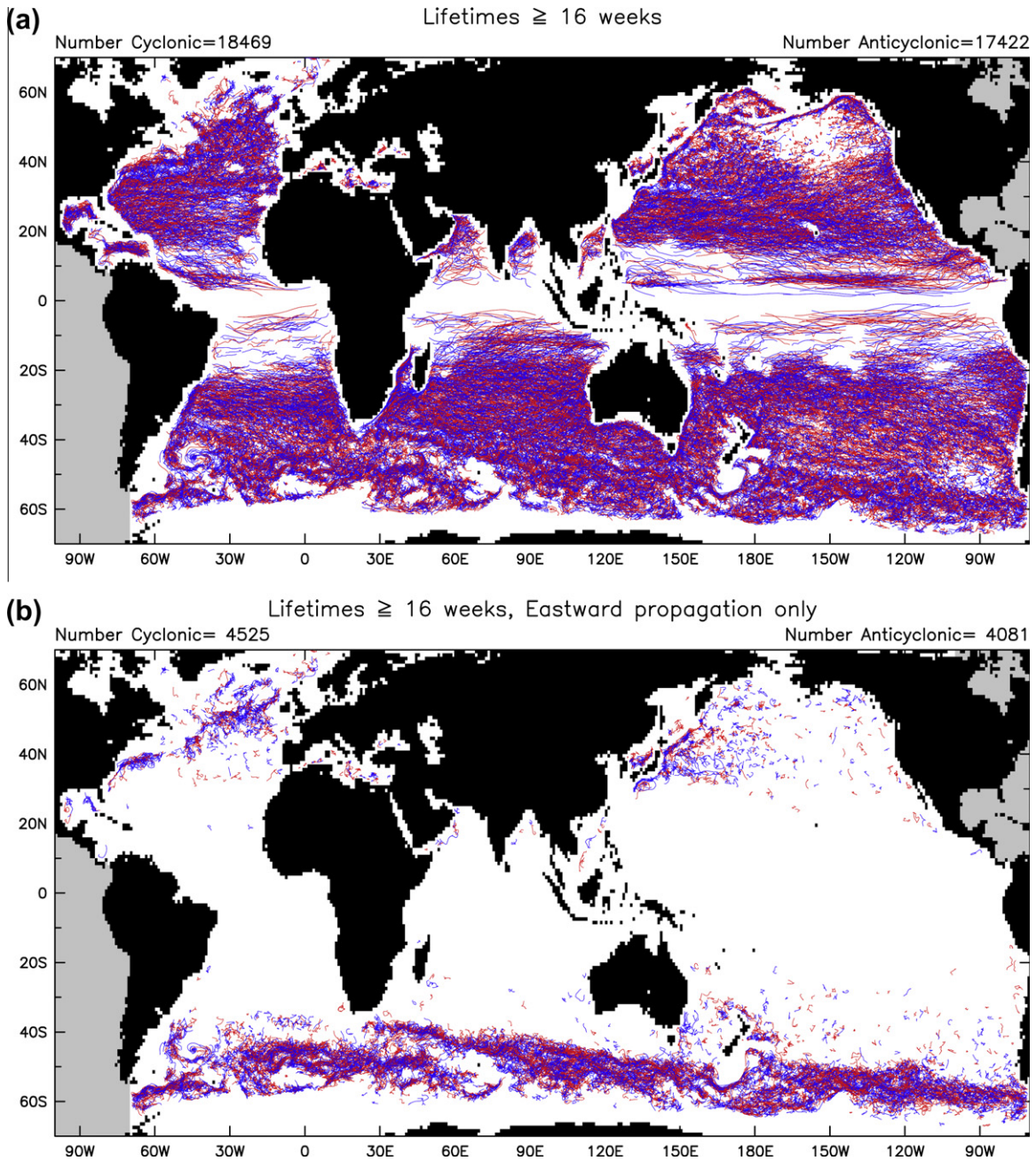


Fig. 4a and b. The trajectories of cyclonic (blue lines) and anticyclonic (red lines) eddies over the 16-year period October 1992–December 2008 for (a) lifetimes ≥ 16 weeks and (b) lifetimes ≥ 16 weeks for only those eddies for which the net displacement was eastward. The numbers of eddies of each polarity are labeled at the top of each panel.

3.4. Eddy origins and terminations

A census of eddy origins is shown in the upper panel of Fig. 6. The most clearly defined regions of frequent eddy formation are along the eastern boundaries of the ocean basins. These eddies most likely form as meanders that pinch off of the eastern boundary currents and undercurrents or from other manifestations of baroclinic instability in these regions of vertically sheared currents. Outside of these eastern boundary regions, eddies apparently form throughout most of the open-ocean regions where propagating eddies are observed (Figs. 4a and 5). This is consistent with the conclusions of Gill et al. (1974), Robinson and McWilliams (1974), Stammer (1998) and Smith (2007b) and others that nearly all of the World Ocean is baroclinically unstable, particularly in regions where the flow is non-zonal (Spall, 2000; Arbic and Flierl, 2004; Smith, 2007a).

The large number of eddies formed along the various seamount chains northwest of Hawaii is notable. This may be an indication of interaction between bottom topography and the flow field, which could include Rossby waves incident from the eastern basin. Or it may be attributable to abrupt amplification of westward propagating eddies that are too small to detect in the eastern basin and only become trackable when their amplitudes increase as they encounter these bathymetric features.

It should be kept in mind that some of the apparent eddy formations in the upper panel of Fig. 6 may actually be the reappearance of eddies that are temporarily lost to the tracking procedure because of a variety of factors (e.g., noise in the SSH fields or because the shapes of the eddies become temporarily too distorted from interactions with other nearby mesoscale features). Based on animations of the tracked eddies, we do not feel that this is a major problem, but we are not able to quantify how frequently this occurs.

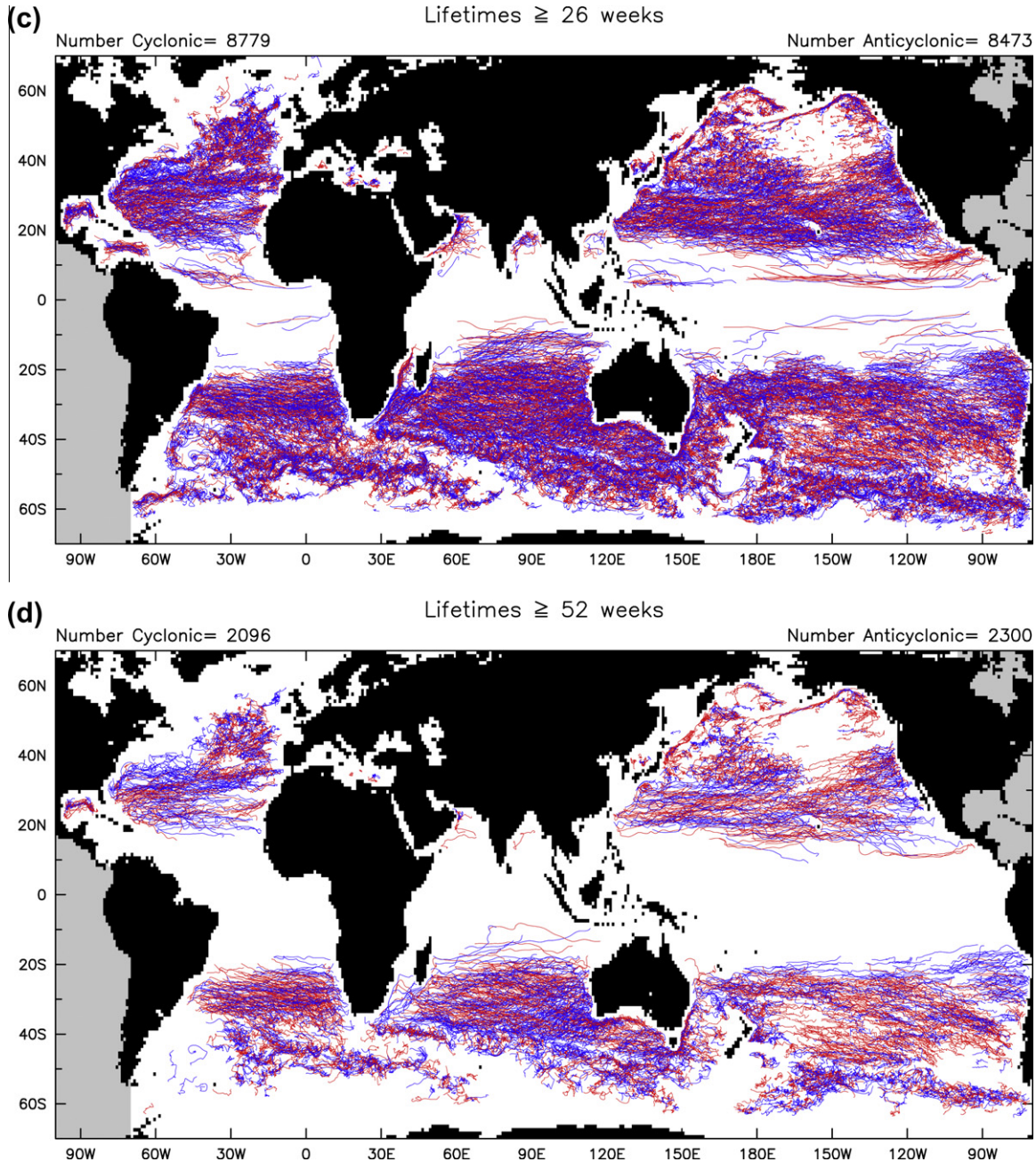


Fig. 4c and d. The same as Fig. 4a, except: (c) lifetimes ≥ 26 weeks and (d) lifetimes ≥ 52 weeks.

A census of eddy terminations is shown in the lower panel of Fig. 6. Like the eddy formation census in the upper panel, eddy terminations occur throughout the regions where eddies are observed. Not surprisingly, terminations are more frequent near most of the western boundaries, especially in the Gulf Stream and Brazil Current and along the Hawaiian Island Chain. The terminations in the open ocean could occur for a variety of reasons, including frictional decay and coalescence with other eddies as a consequence of the up-scale energy cascade of geostrophic turbulence. Some of these terminations may also occur from temporary or permanent loss of an eddy by the tracking procedure because of noise in the SSH field or imperfections of the tracking algorithm.

3.5. Eddy contributions to SSH variance and eddy kinetic energy

Because of the spatial high-pass filtering described in Section 2 that was applied to the raw SSH fields obtained from AVISO, features with wavelength scales larger than about 20° of longitude by 10° of latitude have been attenuated. As previously discussed in Section 2 and shown in detail in Appendix A.3, features with wavelength scales smaller than about $3^\circ \times 3^\circ$ have been attenuated by the filtering of the objective analysis procedure used to construct the SSH fields of the AVISO Reference Series. The half-power filter cutoff of this filtering is estimated in Appendix A.3 to be about $2^\circ \times 2^\circ$. The filtered SSH fields analyzed here thus retain variability with zonal wavelength scales between about 2°

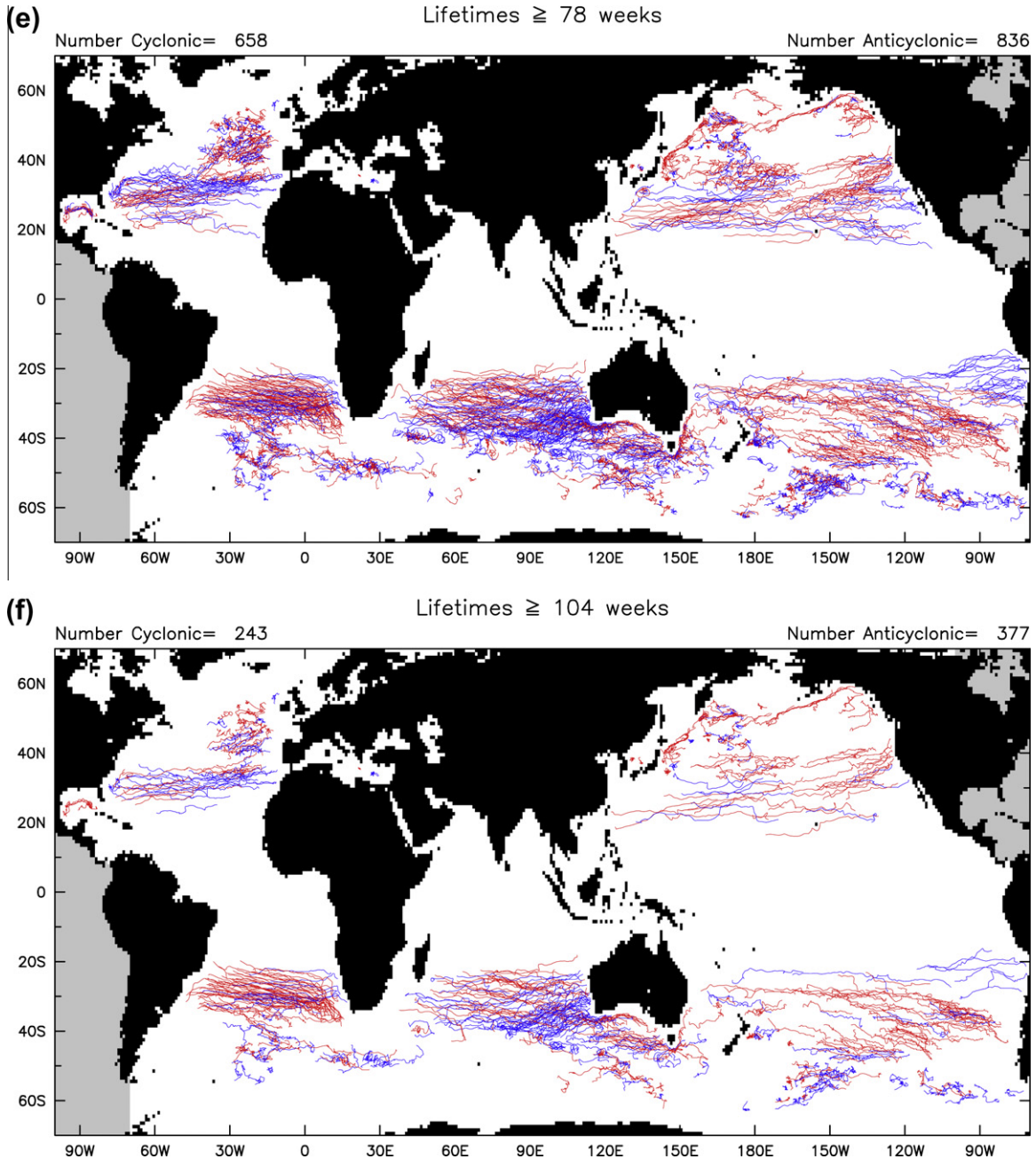


Fig. 4e and f. The same as Fig. 4a, except: (e) lifetimes ≥ 78 weeks and (f) lifetimes ≥ 104 weeks.

and 20° of longitude and meridional wavelength scales between about 2° and 10° of latitude. Numerous physical processes contribute to the variance and eddy kinetic energy of the mesoscale variability that is resolvable by these SSH fields. In addition to the eddies with compact form that are the focus of this study, there are meanders of hydrodynamically unstable currents and the interconnecting ridges and valleys between eddies discussed previously that are part of the up-scale energy cascade. There is also large-scale variability of SSH that is unrelated to the eddy field. The objective of this section is to assess the contributions to the filtered SSH variability from the resolvable vortices with compact form.

The fraction of SSH variance that is accounted for by compact eddies is more difficult to determine than it may at first seem. This depends critically on how well the eddy boundaries can be defined. To appreciate the difficulty, consider the $20^\circ \times 10^\circ$ high-pass filtered SSH at a location (x, y) and time t_i , which we denote as

$h(x, y, t_i)$. The sample mean of this SSH over the $N = 847$ gridded fields at 7-day intervals in the 16-year AVISO Reference Series analyzed here is

$$\bar{h}(x, y) = \frac{1}{N} \sum_{i=1}^N h(x, y, t_i). \quad (1)$$

In view of the removal of the 7-year (1993–1999) average SSH as part of the processing by SSALTO/DUACS (see Appendix A.2) and the $20^\circ \times 10^\circ$ high-pass filtering applied here to the raw AVISO SSH fields, it is not surprising that this mean is found to be less than a few centimeters everywhere. The total variance of the $20^\circ \times 10^\circ$ high-pass filtered SSH fields is

$$\sigma_{\text{tot}}^2(x, y) = \frac{1}{N} \sum_{i=1}^N [h(x, y, t_i) - \bar{h}(x, y)]^2. \quad (2)$$

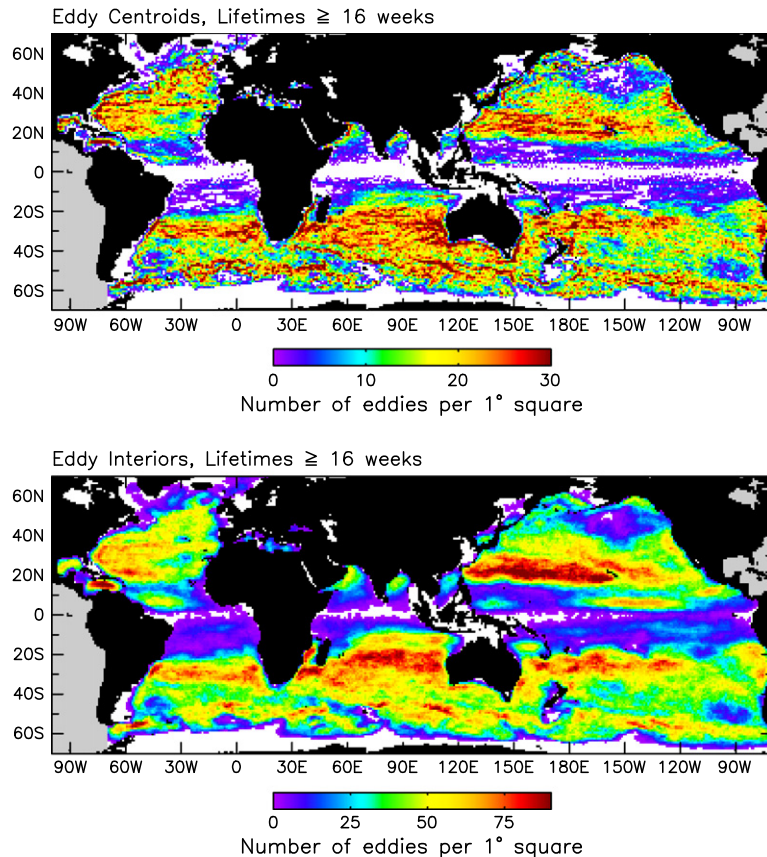


Fig. 5. Census statistics for the numbers of eddy centroids (top) and eddy interiors (bottom) for eddies with lifetimes ≥ 16 weeks that passed through each $1^\circ \times 1^\circ$ region over the 16-year period October 1992–December 2008. The eddy interiors are defined by the contour of SSH around which the average geostrophic speed is maximum (corresponding approximately to a contour of zero relative vorticity).

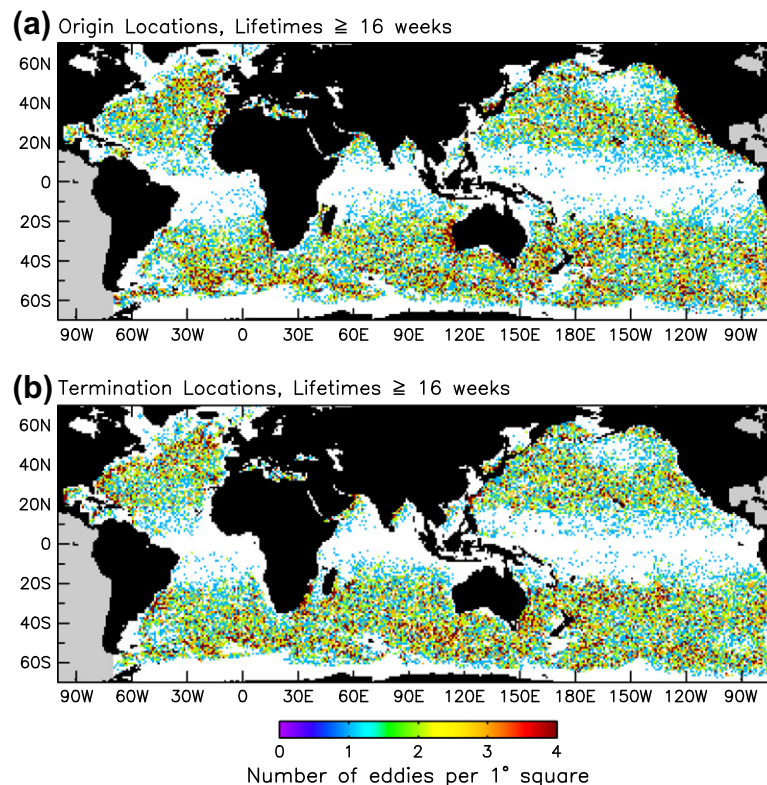


Fig. 6. Census statistics for eddies with lifetimes ≥ 16 weeks showing the numbers of (a) eddy originations and (b) eddy terminations for each $1^\circ \times 1^\circ$ region over the 16-year period October 1992–December 2008.

A very liberal estimate of the contributions of compact eddies to SSH variance can be obtained by assuming that all of the SSH within the boundary of each eddy can be attributed to that eddy (e.g., Chelton et al., 2007). In this case, the eddy variance is

$$\sigma_{hi}^2(x, y) = \frac{1}{N} \sum_{i=1}^N \delta(x, y, t_i) [h(x, y, t_i) - \bar{h}(x, y)]^2, \quad (3)$$

where $\delta(x, y, t_i) = 1$ if the location (x, y) is within an eddy at time t_i and 0 otherwise. This effectively assumes that the basal value of each eddy is zero. If an eddy is embedded in a region of non-zero larger-scale ambient SSH from other causes or is interconnected to neighboring eddies by non-compact mesoscale variability in the form of the ridges and valleys of the spectral continuum of the up-scale energy cascade, as is often the case (see Figs. C2 and C3), this ascribes too much SSH variance to the eddies. The eddy contribution to SSH variance given by Eq. (3) that was reported by Chelton et al. (2007) is therefore biased high.

An estimate of the variance of eddies with compact form that takes into account any local background SSH outside the defined eddy boundaries includes only the portion of SSH within each eddy relative to the basal value of the eddy. For a particular eddy, define $h_0(x, y, t_i)$ to be the basal value associated with every location (x, y) that is interior to the eddy at time t_i . In practice, h_0 is defined to be the average SSH over the piecewise continuous perimeter pixels of each eddy (see Appendix B.3). The estimate of eddy variance adjusted for the basal value of each of the compact eddies in the dataset is

$$\sigma_{lo}^2(x, y) = \frac{1}{N} \sum_{i=1}^N \delta(x, y, t_i) [h(x, y, t_i) - h_0(x, y, t_i)]^2. \quad (4)$$

If this concept of localized eddies superimposed on a regional background SSH unrelated to the eddy field were correct and it were possible to define and determine each eddy boundary unambiguously and accurately, this approach would provide an accurate assessment of the eddy contributions to SSH variance.

In practice, eddies do not have well-defined boundaries. As discussed in Appendix C, the outer perimeter of an eddy becomes especially difficult to define when the eddy is interacting with other eddies nearby. Estimated eddy boundaries may therefore not encapsulate all of the SSH attributable to the eddies, i.e., the $h_0(x, y, t_i)$ are conservative estimates of the true basal heights; the estimates are likely to be biased high for anticyclonic eddies and low for cyclonic eddies, resulting in underestimation of eddy amplitudes and residual plateaus after subtracting the SSH relative to the estimated basal heights. The eddy variance in Eq. (4) is thus necessarily biased low because of this incomplete eddy removal. It is shown in Appendix C that these biases in the estimated amplitudes of eddies with compact form are seldom more than 1 cm outside of regions of energetic mesoscale variability and may be 1 or 2 cm, but only occasionally more than that, in the energetic regions (Figs. C2 and C3). Much of the background SSH outside of these compact features consists of larger-scale variability that is unrelated to the eddy field, as well as the previously noted interconnecting ridges and valleys of SSH between eddies (Figs. C2 and C3). The eddy identification procedure summarized in Appendix B.2 has been specifically designed to exclude these non-compact structures since they do not have a form that resembles the usual notion of an eddy.

The two approaches in Eqs. (3) and (4) to estimating the eddy contributions to SSH variance could be cautiously interpreted as upper and lower bounds on the actual SSH variance that is attributable to eddies. However, a better assessment of the performance of the automated eddy identification and tracking procedure can be obtained from the eddy kinetic energy determined from the velocity components u and v computed from SSH by the geostrophic

Eqs. (B.3a) and (B.3b) in Appendix B.1. The large-scale SSH and much of the non-compact mesoscale variability are effectively filtered out by the spatial high-pass filtering of the derivative operations applied to the SSH fields to compute geostrophic velocity to determine the eddy kinetic energy. The total eddy kinetic energy from the $20^\circ \times 10^\circ$ high-pass filtered SSH at location (x, y) is

$$\text{EKE}_{\text{tot}}(x, y) = \frac{\rho}{2} \frac{1}{N} \sum_{i=1}^N [u(x, y, t_i) - \bar{u}(x, y)]^2 + [v(x, y, t_i) - \bar{v}(x, y)]^2, \quad (5)$$

where ρ is the water density and $\bar{u}(x, y)$ and $\bar{v}(x, y)$ are defined following Eq. (1) for the mean SSH, $\bar{h}(x, y)$, to be the sample mean geostrophic velocity components at location (x, y) over the $N = 847$ gridded SSH fields analyzed here. The eddy kinetic energy attributable to the mesoscale features with compact form (eddies) can be estimated by including only the geostrophic velocities within eddy interiors,

$$\text{EKE}_{\text{lo}}(x, y) = \frac{\rho}{2} \frac{1}{N} \sum_{i=1}^N \delta(x, y, t_i) ([u(x, y, t_i) - \bar{u}(x, y)]^2 + [v(x, y, t_i) - \bar{v}(x, y)]^2), \quad (6)$$

where $\delta(x, y, t_i)$ is defined as in Eq. (3). Since the estimated eddy boundaries may not encapsulate all of the SSH attributable to the eddies as discussed above (see also Appendix C), this is a lower-bound estimate of the eddy kinetic energy attributable to the eddies.

The value of EKE_{lo} computed by Eq. (6) and expressed as a percentage of the total eddy kinetic energy EKE_{tot} of the $20^\circ \times 10^\circ$ high-pass filtered SSH fields computed by Eq. (5) is shown in the top panel of Fig. 7 for the case of the eddies with lifetimes of 16 weeks and longer that are the focus of this study. In the eddy-rich regions, the eddies typically account for more than 40% of the eddy kinetic energy, with more than 70% explained in some regions (e.g., the regions southwest of Australia, to the west of South Africa, in the Alaska Stream along the Aleutian Island Chain, in portions of the Antarctic Circumpolar Current in the South Pacific and South Indian oceans, and in the Kuroshio Current and Gulf Stream just east of where they separate from the western boundaries). About 30% of the eddy kinetic energy is accounted for in the more quiescent regions.

Some of the unexplained eddy kinetic energy in the top panel of Fig. 7 is attributable to the $\sim 140,000$ compact eddies that have lifetimes between 4 and 16 weeks (see Fig. 2) that, except where noted, are not considered in the analyses presented in this study. The value of EKE_{lo} expressed as a percentage of EKE_{tot} for eddies with lifetimes of 4 weeks and longer (the minimum retained by the tracking algorithm) is shown in the bottom panel of Fig. 7. The percentage of eddy kinetic energy explained increases to more than 60% in most of the eddy-rich regions and is typically about 40% or more in the quiescent regions. Since the bias of the estimated amplitudes of the compact forms that we define to be eddies is sometimes 1 or 2 cm and only occasionally more than that (Appendix C), much of the remaining unexplained eddy kinetic energy in the bottom panel of Fig. 7 consists of the elongated interconnecting ridges and valleys between eddies. Some is attributable transient eddies with lifetimes shorter than the 4-week minimum retained by the tracking algorithm.

3.6. Geographical distribution of eddy polarity

The final census statistic presented here reveals an interesting inhomogeneity in the geographical distribution of eddy polarity. While the histograms in Figs. 2 and 3 indicate only small

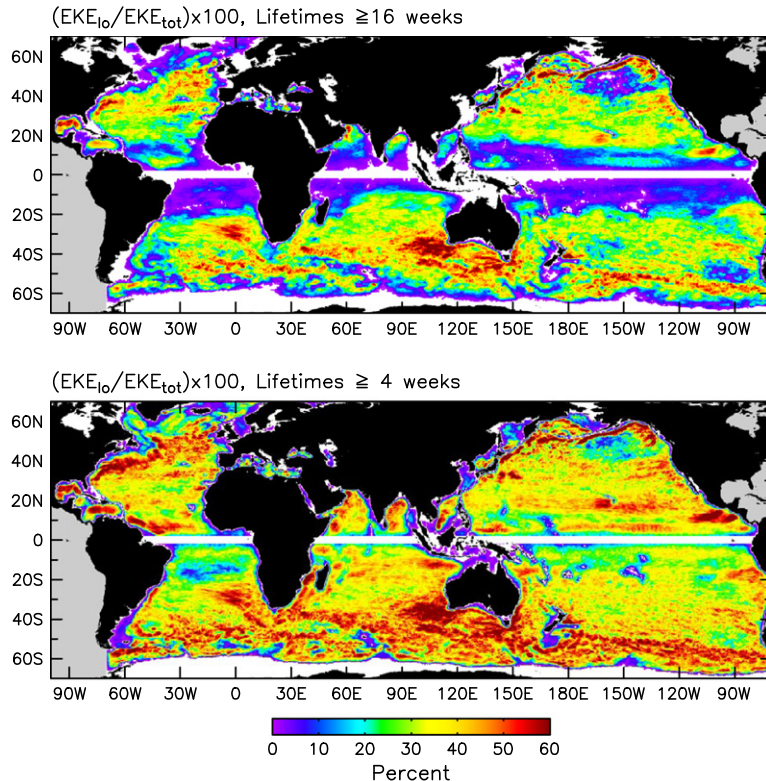


Fig. 7. Lower-bound estimates of the percentage of eddy kinetic energy that is accounted for by eddies with lifetimes ≥ 16 weeks (upper panel) and lifetimes ≥ 4 weeks (lower panel).

differences between the numbers of cyclones and anticyclones in a global census for the lifetimes ≥ 16 weeks considered here, the partitioning of eddy polarity can be very inhomogeneous regionally. Overall, the ratio of cyclonic to anticyclonic eddies is rather noisy (Fig. 8), but some patterns do emerge. For example, mesoscale variability is predominantly cyclonic on the equatorward sides of strong, meandering eastward currents such as the Gulf Stream, the Kuroshio Extension and the Agulhas Return Current. Likewise, there is a predominance of anticyclonic eddies on the poleward sides of these currents, although these regions of preference for anticyclones are narrower and somewhat less well defined than their counterpart regions of preference for cyclonic eddies.

The parallel bands of preference for opposing eddy polarity on the equatorward and poleward sides of the meandering flows are to be expected because the meanders that pinch off to form closed vortices have cyclonic vorticity on the equatorward side and anticyclonic vorticity on the poleward side of the unstable flows. The less well-defined bands of anticyclonic eddies may be an indication that the anticyclones on the poleward sides of the currents have shorter lifetimes than the cyclones on the equatorward sides, perhaps because they tend to be reabsorbed into the currents, as is known to be the case for the Gulf Stream region. In part, this is likely due to the tendency for westward propagating anticyclonic eddies to deflect equatorward, and hence toward the cores of the currents.

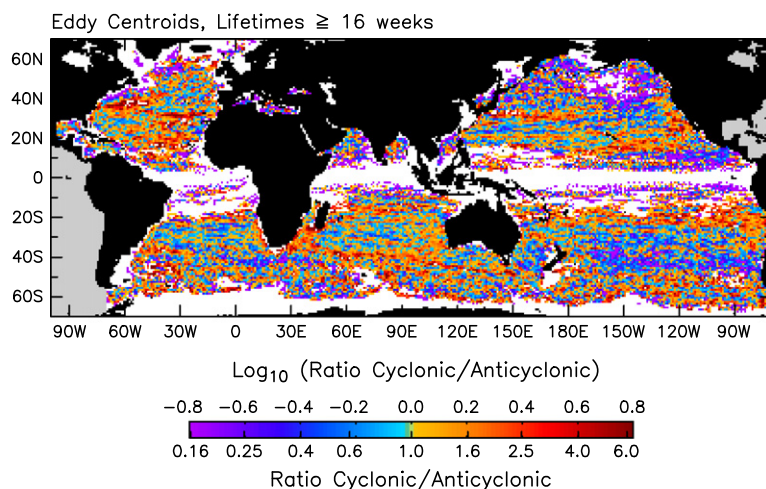


Fig. 8. The ratio of the numbers of cyclonic to anticyclonic eddy centroids for eddies with lifetimes ≥ 16 weeks that propagated through each $1^\circ \times 1^\circ$ region over the 16-year period October 1992–December 2008. A logarithmic scale is used for the color bar in order to give equal emphasis to the ratios r and $1/r$.

Analogous patterns of preference for eddy polarity are found in association with other major meandering currents in the World Ocean. For example, mesoscale variability off the west coast of the US is predominantly cyclonic on the offshore side of the equatorward California Current, presumably from offshore meanders of the flow pinching off to form cyclones. Patches of preferred anticyclonic eddies occur on the inshore side of the California Current near the major capes.

An intriguing feature of Fig. 8 is the pattern of quasi-zonal bands of alternating preference for cyclones and anticyclones in many mid-ocean regions. There are reasons to expect a preferred eddy polarity in some regions. Examples include a preference for anticyclones to the west of the Central American wind jets (e.g., Palacios and Bograd, 2005; Zamudio et al., 2006; Willett et al., 2006) and the anticyclones that form at the Agulhas Retroflection and propagate across the entire South Atlantic (e.g., Byrne et al., 1995; Schouten et al., 2000). The two bands of preferentially anticyclonic eddies separated by a band of preferentially cyclonic eddies to the west-southwest of the Hawaiian Islands are generated by wind forcing from the wind stress curl patterns that are associated with the westward wind jet at the southern tip of the island of Hawaii and the gap winds between the islands of Hawaii and Maui (e.g., Holland and Mitchum, 2001; Lumpkin and Flament, 2001; Calil et al., 2008; Yoshida et al., 2010). The band of preferential cyclonic eddies along 34°N in the North Atlantic coincides with the Azores Front (e.g., Pingree and Sinha, 2001; Mouriño et al., 2003). In most other open-ocean regions, no simple explanations exist for the banded structures of alternating polarity preference.

Whether the bands of alternating preference for eddy polarity in the open ocean in Fig. 8 are persistent features or are attributable to inadequate sampling of the energetic mesoscale eddy field with the 16-year data record analyzed here is an open question. These quasi-zonal structures are reminiscent of the alternating quasi-zonal jets or striations in time averages of velocity that have received a great deal of attention in recent years (e.g., Maximenko et al., 2008 and references therein). Such alternating jets are predicted as the end result of the up-scale cascade of energy from geostrophic turbulence theory (Rhines, 1975). Dynamical interpretation of these features is complicated by the presence of the energetic mesoscale eddy field that is the subject of this study. Striations with characteristics very similar to those reported in the literature as quasi-zonal jets can arise purely as artifacts of the limited sampling of a completely random eddy field (Schlax and Chelton, 2008). The amplitudes of these artifacts diminish as the record length of the time averages increase. The present duration of the SSH fields of the AVISO Reference Series is not sufficient to resolve the issue of whether the apparent alternating jets are real or artifacts of an inadequately sampled eddy field.

The bands of alternating preference for eddy polarity evident in Fig. 8 further complicate the interpretation of quasi-zonal jets. An isolated propagating eddy generates a pair of opposing zonal velocity structures in time averages of the velocity field owing to the opposing zonal velocities in the northern and southern portions of the eddy (see Fig. 10 of Scott et al., 2008). The opposing meridional velocities in the western and eastern portions of the eddy cancel from the combination of westward propagation and time averaging, thus resulting only in the pair of opposing zonal velocity structures in the time average. While these are true features of the time-averaged velocity field, they clearly cannot be interpreted as quasi-zonal jets since they do not exist in jet-like form in any instantaneous snapshot. A zonal band of preferred eddy polarity can likewise be expected to result in a pair of opposing zonal velocity structures in long time averages. To at least some extent, the quasi-zonal jets deduced from time averages of the SSH fields of the AVISO Reference Series could thus be simply the inevitable

consequence of the bands of alternating polarity preference in Fig. 8.

4. Kinematic properties of the observed eddies

The automated eddy identification and tracking procedure described in Appendices B.2–B.4 provides estimates of eddy amplitude, scale and rotational speed as defined in Appendix B.3 at each 7-day time step along an eddy trajectory. These kinematic properties and estimates of the Rossby numbers of the tracked eddies over the 16-year data record analyzed here are summarized in this section.

4.1. Eddy amplitudes

The amplitude A of an eddy is defined here to be the magnitude of the difference between the estimated basal height of the eddy boundary and the extremum value of SSH within the eddy interior (Appendix B.3). Since the eddy identification procedure strives to identify the eddies as compact mesoscale features, the basal height represents the larger-scale ambient SSH around the perimeter of the compact features, thus resulting in amplitudes that are much smaller than those relative to a reference of zero SSH, as discussed previously in Sections 2 and 3.5 (see also Appendix C). The amplitudes defined in this manner are mostly quite small. Histograms and upper-tail cumulative histograms of the eddy amplitudes are shown separately for cyclones and anticyclones in the top two panels of the left column of Fig. 9a for the northern hemisphere and Fig. 9b for the southern hemisphere. The modes of the distributions (i.e., the most frequently occurring amplitude) are about 4 cm for both polarities in both hemispheres. The distributions are strongly skewed toward large values; the mean amplitudes are about double the modes of the distributions. Globally, about 40% of the tracked eddies have amplitudes of $A < 5$ cm and 25% have $A > 10$ cm.

From the map of average eddy amplitude in the top left panel of Fig. 10, the large-amplitude eddies occur only in the relatively confined regions of highly unstable currents such as the Gulf Stream and its extension around Grand Banks, the Kuroshio Extension, the Agulhas Current and the Agulhas Return Current, the Antarctic Circumpolar Current, the Brazil–Malvinas Confluence region, the East Australia Current, and the Loop Current in the Gulf of Mexico. A band of large mean eddy amplitude extends west of the Central American wind jets. Over the rest of the ocean, the mean eddy amplitudes are generally less than 10 cm.

The predominance of small eddy amplitudes may raise concerns that the distribution of observed eddy amplitudes is influenced by the unavoidable bias toward underestimation of eddy amplitude discussed in Section 3.5. From the binned scatter plot in the bottom right panel of Fig. 10, however, there is close geographical agreement between the average eddy amplitudes in the top left panel and the standard deviation of $20^\circ \times 10^\circ$ high-pass filtered SSH in the bottom left panel. The standard deviation can be considered a measure of the magnitude of the typical value of the SSH anomaly contributing to variability in the spatially high-pass filtered SSH fields. If the standard deviation were larger than the average eddy amplitudes, this would be a clear indication that the observed eddies do not account for much of the mesoscale SSH variability. That the standard deviation and the average eddy amplitude are nearly the same suggests that the standard deviation of spatially high-pass filtered SSH is largely attributable to the eddies. It also lends confidence that the bias of the estimated eddy amplitudes is not large in the open-ocean regions, at least not for the eddies with lifetimes ≥ 16 weeks that are the focus of this investigation. The flattening of the relation between average eddy amplitude and

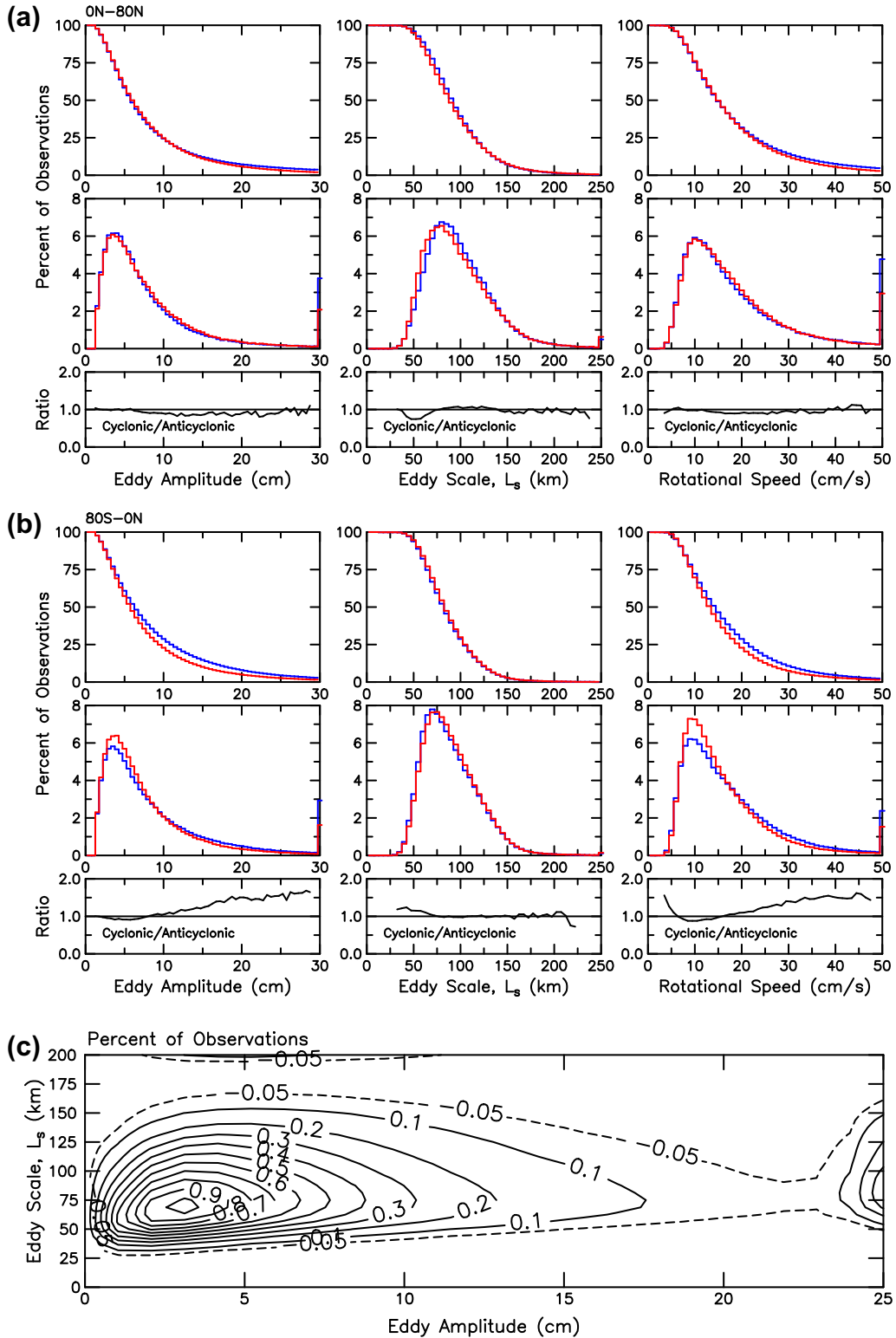


Fig. 9. The distributions of the amplitudes A , speed-based radius scales L_s , and rotational speeds U (left to right) of eddies with lifetimes ≥ 16 weeks in (a) the northern hemisphere and (b) the southern hemisphere. Upper-tail cumulative histograms and histograms are shown in the first and second rows of panels, respectively, with blue and red lines corresponding, respectively, to histograms for cyclonic and anticyclonic eddies. The ratios of cyclonic to anticyclonic eddies are shown in the third rows of panels. The global two-dimensional histogram of the joint distribution of the amplitudes A and scales L_s is shown in panel (c). The contours near the far right and near the top of this two-dimensional histogram arise because all of the eddies with amplitudes and scales larger than the maximum values of the abscissa and ordinate have been placed in the last bins along each axis (see the spikes in the last bins of the individual histograms in the second rows of panels (a) and (b)).

SSH standard deviation in the bottom right panel of Fig. 10 for average amplitudes larger than about 20 cm is likely attributable

to the tendency of our eddy identification procedure to underestimate the amplitudes of eddies in the regions of most energetic

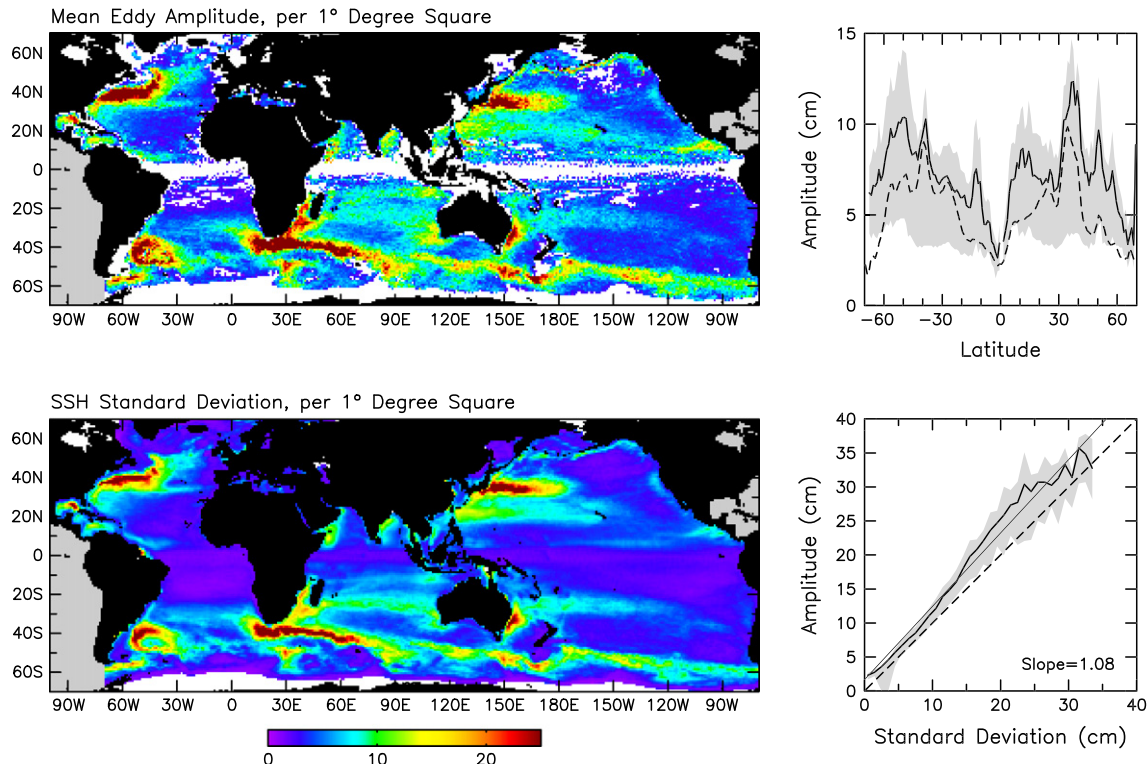


Fig. 10. Maps of the average amplitude of eddies with lifetimes ≥ 16 weeks (top left) and the standard deviation of the $20^\circ \times 10^\circ$ spatially high-pass filtered SSH from which the eddies are identified (bottom left) for each $1^\circ \times 1^\circ$ region. The upper right panel shows meridional profiles of the average (solid line) and the interquartile range of the distribution of eddy amplitudes within each 1° latitude bin (i.e., the 25 and 75% points of each distribution, shown by the gray shading) and the zonal average of the SSH standard deviation (dashed line). The lower right panel shows binned averages of the eddy amplitudes from the top left panel as a function of the standard deviation of spatially high-pass filtered SSH from the bottom left panel, with the interquartile range of the distribution in each bin overlaid as gray shading.

mesoscale variability because the size constraint imposed by our algorithm for global identification of eddies is too restrictive in these regions. From the discussion in Appendix C, this can lead to biases of 1 or 2 cm in these regions but seldom more than that, at least for the compact forms of mesoscale eddies assumed by our eddy identification procedure.

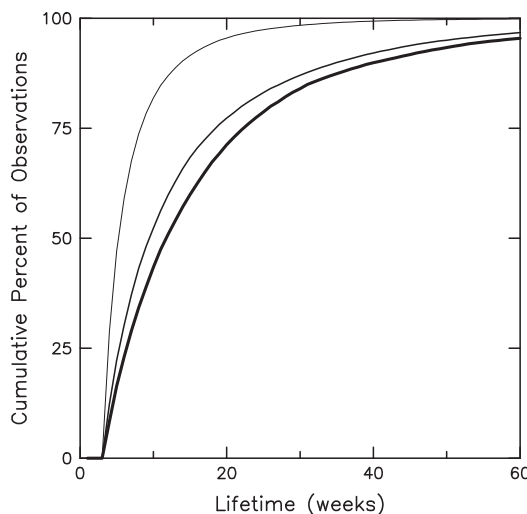


Fig. 11. Cumulative histograms of the lifetime distributions of all of the tracked eddies (lifetimes ≥ 4 weeks) within the lower, middle and upper 25 percentiles of the distribution of eddy amplitudes averaged over the lifetime of each eddy: $A < 3.6$ cm (thin line), $4.6 \leq A \leq 7.6$ cm (medium line thickness), and $A > 10.1$ cm (thick line).

The lifetime distributions of eddies for three different classes of eddy amplitude (averaged over the lifetime of each eddy) are shown in Fig. 11. The observed eddies with the 25% smallest amplitudes ($A < 3.6$ cm) have short lifetimes; 74% have lifetimes ≤ 8 weeks and only 7% have lifetimes longer than the 16-week threshold of the eddies analyzed in this study. Eddies within the middle 25% of the distribution of amplitudes ($4.6 \text{ cm} \leq A \leq 7.6 \text{ cm}$) are much longer lived; 43% have lifetimes ≤ 8 weeks and 29% have lifetimes ≥ 16 weeks. For eddies with the 25% largest amplitudes ($A > 10.1$ cm), 34% have lifetimes ≤ 8 weeks and 47% have lifetimes ≥ 16 weeks.

The latitudinal variation of the zonally averaged eddy amplitude is shown along with the zonally averaged SSH standard deviation in the upper right panel of Fig. 10. Like the overall distributions of the eddy amplitudes in Fig. 9a and b, a positive skewness of the distribution of eddy amplitudes within each latitude band is evident from the relationship between the latitudinal profiles of the mean and the interquartile ranges of the distributions that are shown by gray shading (i.e., the 25% and 75% points of the distribution at each latitude); the mean at each latitude is skewed toward large values within the interquartile range of variability.

The peak in the latitudinal profile of mean eddy amplitude in the upper right panel of Fig. 10 that occurs between about 36°N and 42°N corresponds to the latitude range of the Gulf Stream Extension and the Kuroshio Extension. The broad peak of smaller amplitude centered near 15°N is associated with the eddies to the west of Central America (e.g., Palacios and Bograd, 2005; Willert et al., 2006) that are generated by the Central American wind jets over the Gulfs of Tehuantepec and Papagayo and possibly by instabilities of the nearshore currents triggered by downwelling coastally trapped waves of equatorial origin (Zamudio et al.,

2006). These eddies originate near the coast but often reach their maximum amplitude well away from the coast, suggesting the importance of baroclinic instability of the North Equatorial Current (Farrar and Weller, 2006). The narrow peak centered at about 12°S in the upper right panel of Fig. 10 is associated with eddies that are generated between Australia and Indonesia and propagate westward across much of the south tropical Indian Ocean (Birol and Morrow, 2001; Feng and Wijffels, 2002; Nof et al., 2002). The narrow peak at about 38°S and the broader peak centered near 50°S correspond to the Agulhas Return Current and the Antarctic Circumpolar Current, respectively.

A significant characteristic of the amplitude histograms in Fig. 9b is that the distribution of the amplitudes of cyclonic eddies in the southern hemisphere is more skewed toward large values than for anticyclonic eddies. As a result, eddies with amplitudes larger than 10 cm are preferentially cyclonic (see the bottom left panel of Fig. 9b). This result is perhaps surprising in view of the previously discussed fact that the eddies with the longest lifetimes and the largest propagation distances are preferentially anticyclonic (Figs. 2 and 3). Amplitude is evidently not the sole factor that determines the longevity of an eddy. A preference for large-amplitude eddies to be cyclonic is expected from the gradient wind effect of centrifugal force that pushes fluid outward in rotating eddies (e.g., Gill, 1982), thus intensifying the low pressure at the centers of cyclones and weakening the high pressure at the centers of anticyclones. However, this cannot account for the differences between cyclonic and anticyclonic eddies in the northern hemisphere where there is a slight preference for anticyclonic eddies for nearly all amplitudes (see the bottom left panel of Fig. 9a). We are not able to explain this hemispheric difference in the amplitude dependence on polarity.

4.2. Eddy scales

The characterization of eddy scale used here is the speed-based radius estimate L_s , defined in Appendix B.3 to be the radius of a circle with area equal to that within the closed contour of SSH in each eddy that has the maximum average geostrophic speed. This eddy scale corresponds approximately to the radius at which the relative vorticity within the eddy is zero. If the eddies had Gaussian shapes, this would occur at a radius of $2^{-1/2}L_e$, where L_e is the e-folding scale of the radial dependence r of a Gaussian profile of height h expressed in the form $h(r) = A \exp(-r^2/L_e^2)$.

We also investigated an alternative definition of eddy scale based on a Gaussian approximation of each eddy. It is shown in

Appendix B.3, however, that estimates of the Gaussian e-folding scale L_e resulted in radii of corresponding maximum rotational speed that were 64% smaller on average than the empirically determined radius L_s of actual maximum speed within each eddy. This indicates that, while a Gaussian shape is a good approximation for the average eddy profile over the inner 2/3 of the eddies (see Section 5), the rotational speeds within eddy interiors are not well represented by Gaussian approximations, at least not over their entire interiors. The shapes of the observed eddies are examined in detail in Section 5.

Histograms and upper-tail cumulative histograms of the radius scales of the eddies are shown separately for cyclones and anticyclones in the top two panels of the middle column of Fig. 9a for the northern hemisphere and Fig. 9b for the southern hemisphere. Unlike the amplitude distributions in Fig. 9, there are no significant differences between the distributions of the speed-based eddy scale L_s for cyclones and anticyclones in either the northern or the southern hemisphere (bottom panels of the middle columns of Fig. 9a and b, respectively). The modes of both distributions occur at about 75 km (somewhat larger in the northern hemisphere and smaller in the southern hemisphere). Globally, more than 90% of the tracked eddies had scales between 50 and 150 km. For both eddy polarities, the mean values of L_s are 96 km in the northern hemisphere and 87 km in the southern hemisphere.

The geographical distribution of the mean eddy scale (left panel of Fig. 12) is characterized as an essentially monotonic decrease from about 200 km in the near-equatorial regions to about 75 km at 60° latitude in both hemispheres. This simple latitudinal dependence is further evident from the relatively narrow interquartile range of variability within each latitude band shown by gray shading in the right panel of Fig. 12. As previously found by Stammer (1997) and Chelton et al. (2007) and others, this approximate factor-of-2.5 decrease in eddy scale is much smaller than the approximate factor-of-25 decrease of the Rossby radius of deformation over the same latitude range (Chelton et al., 1998), which is shown by the dotted line in the right panel of Fig. 12. The large scales of the observed mesoscale eddies compared with the Rossby radii at middle and high latitudes are consistent with the up-scale transfer of kinetic energy from a source with scales near the Rossby radius of deformation that is expected from geostrophic turbulence theory (e.g., Kraichnan, 1967; Batchelor, 1969; Charney, 1971; Rhines, 1975, 1979; Stammer, 1997; Scott and Wang, 2005).

There is a significant hemispheric distinction between the distributions of eddy scale. For both cyclonic and anticyclonic eddies, the distributions are less skewed toward large values in

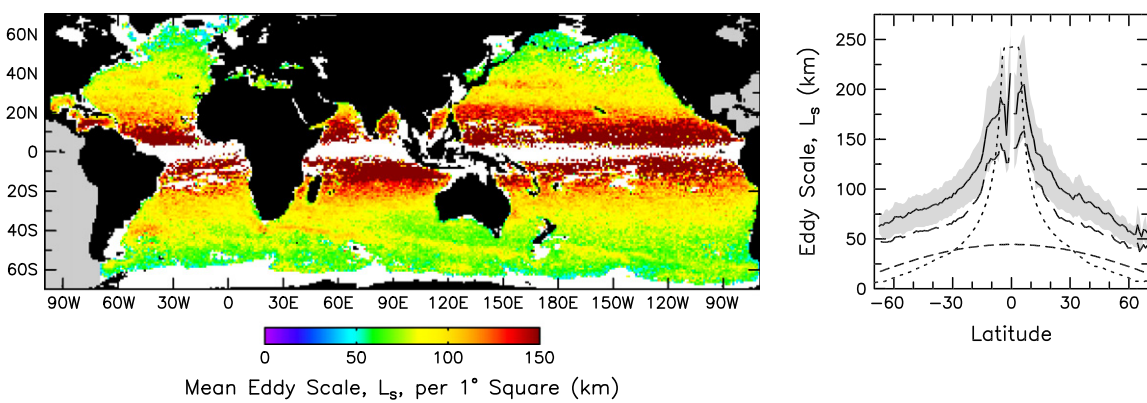


Fig. 12. Map of the average speed-based radius scale L_s for eddies with lifetimes ≥ 16 weeks (left) for each $1^\circ \times 1^\circ$ region. The right panel shows meridional profiles of the average (solid line) and the interquartile range of the distribution of L_s (gray shading) in 1° latitude bins. The long dashed line is the meridional profile of the average of the e-folding scale L_e of a Gaussian approximation of each eddy (see Appendix B.3). The short dashed line represents the 0.4° feature resolution limitation of the SSH fields of the AVISO Reference Series for the zonal direction (see Appendix A.3) and the dotted line is the meridional profile of the average Rossby radius of deformation from Chelton et al. (1998).

the southern hemisphere than in the northern hemisphere. This explains the smaller mean value of L_s in the southern hemisphere noted above. The hemispheric difference in the distributions of eddy scale is likely attributable to the general decrease in L_s with increasing latitude and the much greater expanse of ocean at high latitudes in the southern hemisphere.

An important point to be noted from the right panel of Fig. 12 is that the estimated eddy scales are much larger everywhere than the minimum scale of features that can be resolved by the SSH fields of the AVISO Reference Series, which is shown in Appendix A.3 to be equivalent to an e-folding radius of about 0.4° (corresponding to approximately 40 km) for an eddy with Gaussian shape (shown by the bottom dashed line in the right panel of Fig. 12). This is true regardless of whether the eddy scales are characterized by the speed-based scale L_s that is our preference (the solid line in the right panel of Fig. 12) or the e-folding scale L_e of a Gaussian approximation of each eddy estimated as described in Appendix B.3 (the long dashed line in Fig. 12). The large scales of the eddies obtained from the automated eddy identification and tracking procedure are thus not artifacts of resolution limitations of the SSH fields of the AVISO Reference Series. On the other hand, the histograms of eddy scales in Fig. 9 would likely change substantially at the lower range if the SSH fields analyzed here were capable of resolving features with scales smaller than 40 km.

The lifetime distributions of eddies for three different classes of eddy scale L_s (averaged over the lifetime of each eddy) are shown in Fig. 13. To avoid misinterpretation from latitudinal variations in the eddy scales and lifetimes, only midlatitude eddies between latitudes of 20° and 40° of both hemispheres are considered in Fig. 13. Eddies at lower latitudes were excluded because they are predominantly large scale with fast propagation speeds and relatively short lifetimes because of the difficulties tracking eddies at low latitudes discussed in Section 3.3. Likewise, eddies at higher latitudes have been excluded because they are also difficult to track owing to their smaller scales, very slow propagation speeds, and their interactions with other eddies that often result in substantial distortions of the eddy boundary from one time step to the next.

It is evident from Fig. 13 that the observed midlatitude eddies with the 25% smallest scales ($L_s < 67$ km) have very short lifetimes; 81% have lifetimes ≤ 8 weeks and only 4% have lifetimes longer than the 16-week threshold of the eddies analyzed in this study.

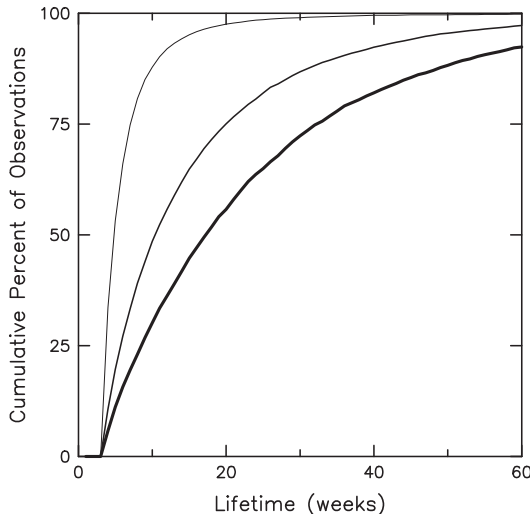


Fig. 13. Cumulative histograms of the lifetime distributions of all of the tracked eddies (lifetimes ≥ 4 weeks) in the latitude range $20\text{--}40^\circ$ of both hemispheres within the lower, middle and upper 25 percentiles of the distribution of speed-based eddy scales averaged over the lifetime of each eddy: $L_s \leq 67$ km (thin line), $75 \text{ km} \leq L_s \leq 95$ km (medium line thickness), and $L_s > 107$ km (thick line).

This may be attributable at least in part to the attenuation of these small-scale eddies by the filtering inherent in the objective analysis procedure used to produce the SSH fields of the AVISO Reference Series (see Appendices A.2 and A.3). Eddies within the middle 25% of the distribution of scales ($75 \text{ km} \leq L_s \leq 95$ km) are much longer lived; 39% have lifetimes ≤ 8 weeks and 33% have lifetimes ≥ 16 weeks. For eddies with the 25% largest scales ($L_s > 107$ km), only 23% have lifetimes ≤ 8 weeks and 53% have lifetimes ≥ 16 weeks.

It is seen from Figs. 11 and 13 that the lifetimes of the meso-scale eddies depend on the horizontal scales of the eddies in a manner that might have been anticipated: eddies with small amplitude or horizontal scale have short lifetimes while eddies with large amplitude or horizontal scale generally have longer lifetimes.

The global joint distribution of eddy amplitudes A and scales L_s in Fig. 9c shows a surprisingly weak correlation between the two. The eddy amplitudes A are broadly distributed for any particular eddy scale L_s . The overall correlation between A and L_s over the $\sim 36,000$ eddies with lifetimes ≥ 16 weeks is only 0.13. There is very little latitudinal variation of this low correlation; when computed within 10° bands of latitude, the correlation is less than 0.16 at all latitudes. This indicates that there is not a universal, self-similar structure for these eddies; instead, amplitude and horizontal scale apparently vary independently.

4.3. Eddy rotational speeds

The rotational speed U of an eddy is characterized here by the maximum of the average geostrophic speeds around all of the closed contours of SSH inside the eddy, i.e., the average geostrophic speed around the same SSH contour that defines the eddy scale L_s discussed in Section 4.2 and described in detail in Appendix B.3. Histograms and upper-tail cumulative histograms of U are shown separately for cyclones and anticyclones in the top two panels of the right column of Fig. 9a for the northern hemisphere and Fig. 9b for the southern hemisphere. The modes of the skewed distributions are about 10 cm s^{-1} for both polarities in both hemispheres. Globally, about 50% of the observed eddies had U values between 10 and 20 cm s^{-1} and 5% had $U \geq 40 \text{ cm s}^{-1}$.

Eddy rotational speed can be roughly characterized as proportional to the ratio of the eddy amplitude A to the eddy scale L_s . In view of the cyclonic preference of eddies with large amplitudes in the southern hemisphere (Section 4.1) and the lack of polarity preference for eddy scale (Section 4.2), it is not surprising that the distribution of rotational speeds in the southern hemisphere is more skewed toward large values for cyclonic eddies than for anticyclonic eddies. As a result, eddies with fast rotational speeds of $U > 20 \text{ cm s}^{-1}$ were preferentially cyclonic in the southern hemisphere (see the bottom right panel of Fig. 9b). Consistent with the distributions of eddy amplitude discussed in Section 4.1, there is a slight preference for anticyclonic eddies for all rotational speeds in the northern hemisphere (see the bottom right panel of Fig. 9a). We are not able to explain this hemispheric difference in the dependence of rotational speeds on polarity.

4.4. Rossby number

The Rossby number is defined to be the ratio of material advection to the Coriolis term in the momentum equation. Using the speed-based eddy scale L_s and maximum rotational speed U summarized in Sections 4.2 and 4.3, the Rossby number can be characterized as $\text{Ro} = U/(fL_s)$, where f is the Coriolis parameter. The histograms and upper-tail cumulative histograms of Ro defined in this way are shown in Fig. 14 for three different latitude bands: the northern hemisphere extratropics ($20^\circ\text{N}\text{--}60^\circ\text{N}$), the tropics

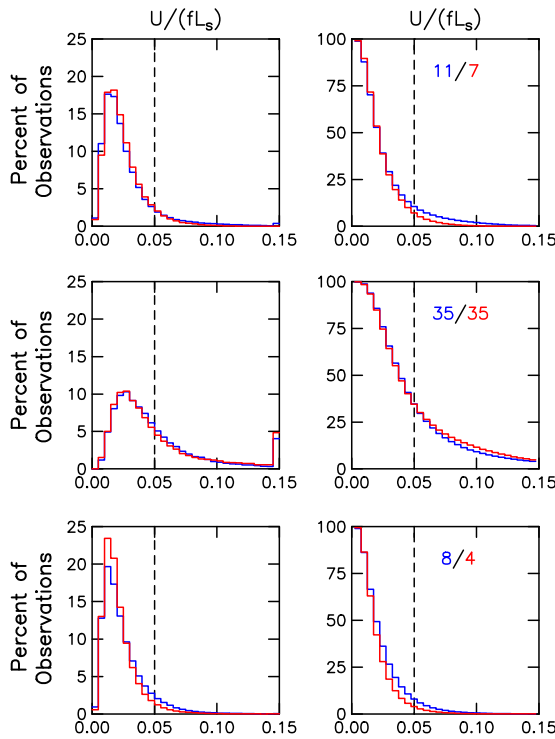


Fig. 14. Histograms (left) and upper-tail cumulative histograms (right) of estimates of the Rossby number, $U/(fL_s)$, of the observed mesoscale features with lifetimes ≥ 16 weeks for three different latitude bands. Top to bottom: 20°N – 60°N , 20°S – 20°N , and 60°S – 20°S . The blue and red lines in each panel correspond to cyclonic and anticyclonic eddies, respectively. The labels on the right panels, color coded to their associated line color, indicate the percentages of eddies of each polarity for which the Rossby number exceeds the value of 0.05 indicated by the vertical dashed line. See text for details.

(20°S – 20°N), and the southern hemisphere extratropics (60°S – 20°S). The percentages of combined cyclonic and anticyclonic mesoscale features in these three latitude bands with $\text{Ro} > 0.05$ are 9%, 35% and 6%, respectively. Only about 1% of the extratropical eddies and about 10% of the tropical eddies had $\text{Ro} > 0.1$. While there is no objective criterion for defining when the Rossby number is “large,” the distributions in Fig. 14 indicate that the observed eddies are not highly nonlinear or ageostrophic by this measure, except at low latitudes where f approaches zero.

The smallness of Ro implies that the momentum equation is dominated by the geostrophic balance between the pressure gradient force and the Coriolis acceleration. This quasi-geostrophic approximation of the dynamics in turn implies that altimetry is adequate for investigating the dynamics of the observed mesoscale features that are resolved by the SSH fields of the AVISO Reference Series since surface velocity can be computed by geostrophy from SSH.

The Rossby number can alternatively be interpreted as the ratio of relative vorticity (which can be characterized by U/L_s) to the local planetary vorticity, which is equal to the Coriolis parameter f . The smallness of Ro thus implies that the relative vorticities of the rotating eddies are small compared with the planetary vorticity.

5. Eddy shapes

The shapes of the mesoscale eddies were investigated from the combined cyclones and anticyclones by normalizing the SSH within each eddy by its (positive) amplitude A , and then normalizing its spatial coordinates by the speed-based scale L_s of the

eddy. Specifically, if the SSH within an eddy at time step t_i is $h(x, y, t_i)$, we formed the doubly normalized SSH defined by

$$h'(x', y', t_i) = A^{-1} h(x/L_s, y/L_s, t_i). \quad (5.1)$$

Each observation of an eddy is thus transformed to have unit amplitude and scale, allowing them to be composited to investigate the shapes of the eddies. The $\sim 36,000$ tracked eddies with lifetimes ≥ 16 weeks comprise ~ 1.15 million individual eddy observations. For each of these observations, $h(x', y', t_i)$ was binned at each normalized coordinate (x', y') , yielding a distribution of the doubly normalized SSH, $h'(x', y')$, from which inferences about eddy shape may be drawn.

The distributions of doubly normalized SSH along east–west and north–south profiles, that is, along the x' and y' axes, respectively, are shown in Fig. 15. The east–west and north–south profiles of the average of doubly normalized SSH are shown by the blue lines, and the modes of the distributions in each bin are shown by the red lines. The interquartile range for the east–west profile is shown as the gray shaded area (the interquartile range for the north–south profile is essentially the same). While the interquartile range increases away from the center of the eddies, indicating less coherent structure with increasing radius, the general shape of the composited eddies is unambiguously “bell-shaped,” as expected. Consideration of cyclones and anticyclones separately yields composites that do not differ significantly from those shown in Fig. 15 for the combined cyclonic and anticyclonic eddies.

The two blue lines in Fig. 15 are nearly the same, indicating that, on average, there is no evidence for anisotropy of the eddy shape in the orthogonal east–west and north–south cross sections of the average of the doubly normalized SSH. The profiles of the averages are well approximated across the central 2/3 of the eddy interiors by the axisymmetric Gaussian profile with an e-folding normalized radius of $L_e = 0.64$ that is overlaid as the thick short dashed line. The associated radius of maximum speed $L = 2^{-1/2}L_e$ is shown as

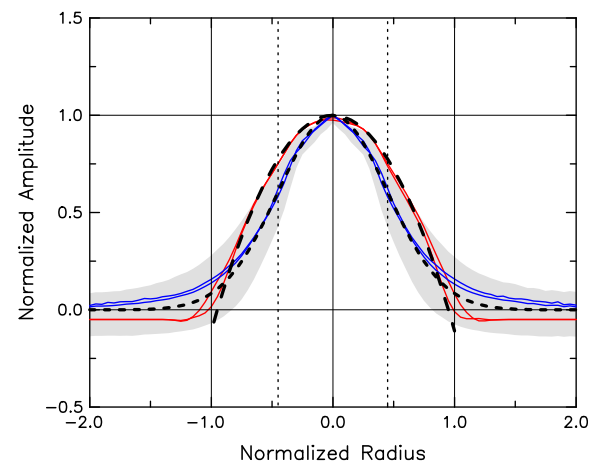


Fig. 15. Composite profiles of the distribution of SSH as functions of radius along east–west and north–south sections computed from all of the eddies with lifetimes ≥ 16 weeks (a total of ~ 1.15 million eddy observations). The SSH profiles along these sections were doubly normalized by the amplitude A and the speed-based scale L_s for each eddy (see text). The gray shading represents the interquartile range of the distribution of values in each normalized radius bin for the east–west section; the interquartile range for the north–south section is essentially the same. The pairs of blue and red lines are the east–west and north–south transects of the average and the mode, respectively, of the doubly normalized SSH. The mode profiles have been smoothed slightly. The thick short dashed line corresponds to a Gaussian profile with a normalized e-folding scale of $L_e = 0.64$ and the vertical dotted lines are the normalized radius $L = 2^{-1/2}L_e$ of maximum rotational speed for this Gaussian. The thick long dashed line corresponds to a quadratic profile with zero crossings at normalized radii of 0.95.

the vertical dotted lines. The flanges of the east–west and north–south profiles of the averages are seen to be flatter than the Gaussian approximation for normalized radii greater than approximately the e-folding scale of the Gaussian, i.e., for unnormalized radii greater than about $0.64L_s$.

The distribution of doubly normalized SSH at radii within most of the interior of the composite eddy is consistently skewed toward small values, resulting in a mode that is larger than the average across approximately 85% of the normalized eddy interior. This skewness is nearly identical in both the east–west and the north–south cross sections, as evidenced by the fact that the modes as a function of normalized radius that are shown by the red lines in Fig. 15 are essentially the same for both cross sections. This is further evidence that, on average, there is no apparent anisotropy of the eddy shape. The mode profiles are well approximated by the quadratic function that is overlaid as the thick long dashed line, which has zero crossings at a normalized radius of 0.95, i.e., very near the radius corresponding to the speed-based eddy scale L_s .

The average value is a good characterization of any variable that has an approximately symmetric distribution. For a variable with a skewed distribution, however, the mode is arguably a better characterization since it corresponds to the most frequently occurring value of the variable. The choice of the mode as the preferred representation of the binned profiles of eddy shape in Fig. 15 is further motivated by the large discrepancy between the speed-based eddy scale L_s and the radius of maximum rotational speed, which occurs at $L = 2^{-1/2}L_e$ for a Gaussian eddy (shown in normalized coordinates by the vertical dotted lines in Fig. 15). From the comparison between estimates of L_s and L in Appendix B.3, $L_s \approx 1.64 L$ (see Fig. B2c). The observed radius L_s of maximum rotational speed in the observed eddies is thus typically 64% larger than it would be if the eddies had Gaussian shape. This is consistent with the differences between the quadratic and Gaussian approximations of the eddy shapes in the composite eddy cross sections in Fig. 15.

It is noteworthy that the average and mode profiles of doubly normalized eddies in the Parallel Ocean Program global ocean circulation model run with a nominal grid spacing of $1/10^\circ$ at Los Alamos National Laboratory (Maltrud and McClean, 2005) are very similar to those shown in Fig. 15. The details of this analysis will be reported elsewhere. For present purposes, this should alleviate concerns that the shapes of the eddies in the SSH fields of the AVISO Reference Series are imposed by the covariance function in the objective analysis procedure used to construct these SSH fields (see Appendix A.2).

While the gray shaded region in Fig. 15 shows that there is considerable variability in the shapes of the large eddies analyzed here, it is clear that Gaussian approximations are not valid over the full interiors of the eddies. It is likewise clear that a substantial number of the eddies have the quadratic structure of the mode profiles. For axially symmetric rotation, a radial profile that is quadratic implies that the relative vorticity is constant within the eddy interior, i.e., out to radii close to the speed-based scale L_s , beyond which the flanges of the eddy become flat. To the extent that the typical eddy can be characterized as having a quadratic profile, this has important dynamical implications; the associated fluid motion consists of solid-body rotation.

6. Nonlinearity

The nonlinearity of the eddies identified in the SSH fields of the AVISO Reference Series is assessed in this section from the statistics of three different nondimensional parameters.

6.1. Advection nonlinearity parameter

A common measure of nonlinearity for the rotating vortices that are of interest here is the nondimensional ratio U/c , where U is the

maximum rotational speed summarized in Section 4.3 and c is the translation speed of the eddy estimated at each point along the eddy trajectory from centered differences of the (x, y) coordinates of successive centroid locations. For Gaussian eddies, a value of U/c that exceeds 1 implies that there is trapped fluid within the eddy interior that is advected with the eddy as the eddy translates. This can be most easily seen from a transformation to a coordinate frame moving with the eddy (e.g., Samelson, 1992). More generally, values of $U/c \geq 1$ that occur when typical rotational fluid speeds are as large as or larger than the eddy translation speed imply that the eddy cannot be regarded as a linear wave disturbance propagating through a nearly stationary medium, but instead is capable of modifying the medium by advecting a trapped fluid parcel as it translates. Eddy advection of trapped fluid implies that the eddies can transport water properties such as heat salt and potential vorticity, as well as biogeochemical characteristics such as nutrients and phytoplankton. While we feel that this advective measure of nonlinearity is the most germane of all nonlinearity parameters for the present study since the trapping of fluid is a fundamental distinction between linear waves and nonlinear eddies, we also investigate two other commonly used measures of nonlinearity in Sections 6.2 and 6.3.

The distributions of U/c defined in the above manner are shown in the first column of Fig. 16 for the same three latitude bands as the Rossby number considered in Fig. 14: the northern hemisphere extratropics (20°N – 60°N), the tropics (20°S – 20°N), and the southern hemisphere extratropics (60°S – 20°S). The estimates of U/c obtained here are nearly a factor-of-2 larger than our previous estimates (Chelton et al., 2007). It is shown in Appendix B.5 that this is because the estimate of U used in our earlier study was overly conservative.

It is apparent from Fig. 16 that virtually all of the observed mesoscale eddies outside of the tropics had $U/c > 1$ and hence were nonlinear by this measure. Some of the mesoscale eddies were highly nonlinear. For example, 48% of the U/c values for the extratropical eddies in both hemispheres exceeded 5 and 21% exceeded 10. Even within the tropics where the translation speeds c are very fast and hence U/c tends to be smaller, about 90% of the combined cyclonic and anticyclonic mesoscale features had $U/c > 1$. Fewer of the tropical eddies are highly nonlinear; only 14% of the U/c values exceeded 5 and 4% exceeded 10.

Close inspection of the top and bottom left panels of Fig. 16 reveals that the distributions of U/c for extratropical eddies are more skewed toward high values for cyclones than for anticyclones in the southern hemisphere but the opposite is found in the northern hemisphere. This puzzling result is consistent with the hemispheric asymmetries of the dependencies of amplitudes and rotational speeds on eddy polarity discussed in Sections 4.1 and 4.3.

A map of the geographical distribution of the average advective nonlinearity parameter U/c in each 1° square region is shown in the top panel of Fig. 17. Not surprisingly, the largest average U/c values are found in all of the major unstable, meandering currents: the Gulf Stream and its extension across most of the high-latitude North Atlantic, the Kuroshio and Oyashio Currents and their eastward extension half way across the North Pacific, the Agulhas Return Current, the Brazil–Malvinas Confluence and the Antarctic Circumpolar Current. Large average values of U/c are also evident in the East Australia Current and in some of the eastern boundary current systems (e.g., the California Current, the Alaska Current, and the Leeuwin Current off the west coast of Australia). A narrow band of high nonlinearity is found along the Azores Front centered near 34°N in the central North Atlantic (Pingree and Sinha, 2001; Mourão et al., 2003) and in the region south and east of Madagascar (Schouten et al., 2003; Quartly et al., 2006). In contrast, the average U/c values are less than 2 everywhere equatorward of about 15° latitude except very near the Central American wind jets,

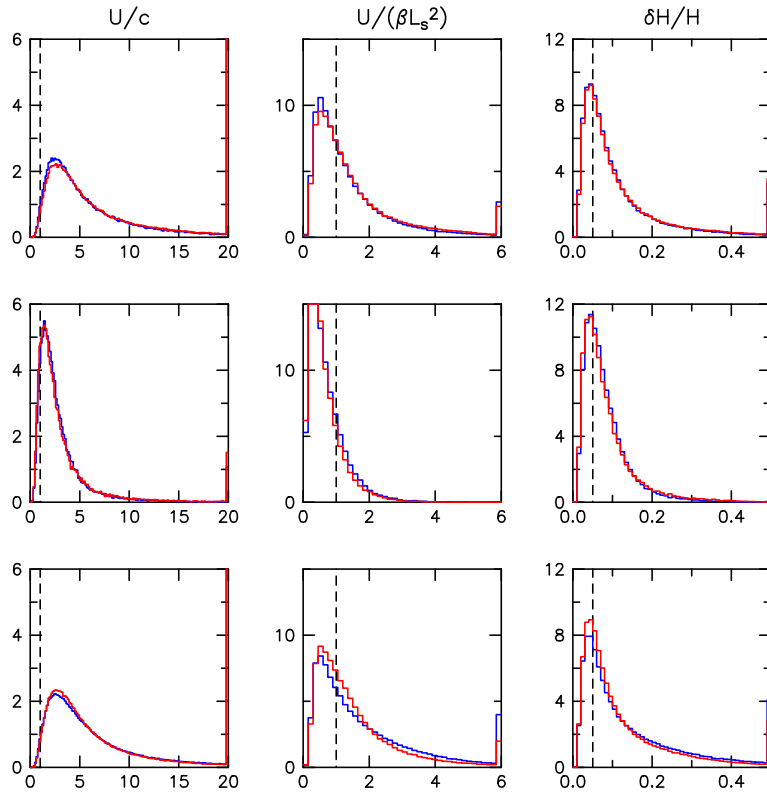


Fig. 16a. Histograms of three measures of the degree of nonlinearity of the observed mesoscale features with lifetimes ≥ 16 weeks for three different latitude bands. Top to bottom: 20°N – 60°N , 20°S – 20°N , and 60°S – 20°S . The three measures of nonlinearity are (left to right): the advective nonlinearity parameter U/c ; the quasi-geostrophic nonlinearity parameter $U/(\beta L_s^2)$; and the upper-layer thickness nonlinearity parameter $\delta H/H$. The blue and red lines in each panel correspond to cyclonic and anticyclonic eddies, respectively. See text for details.

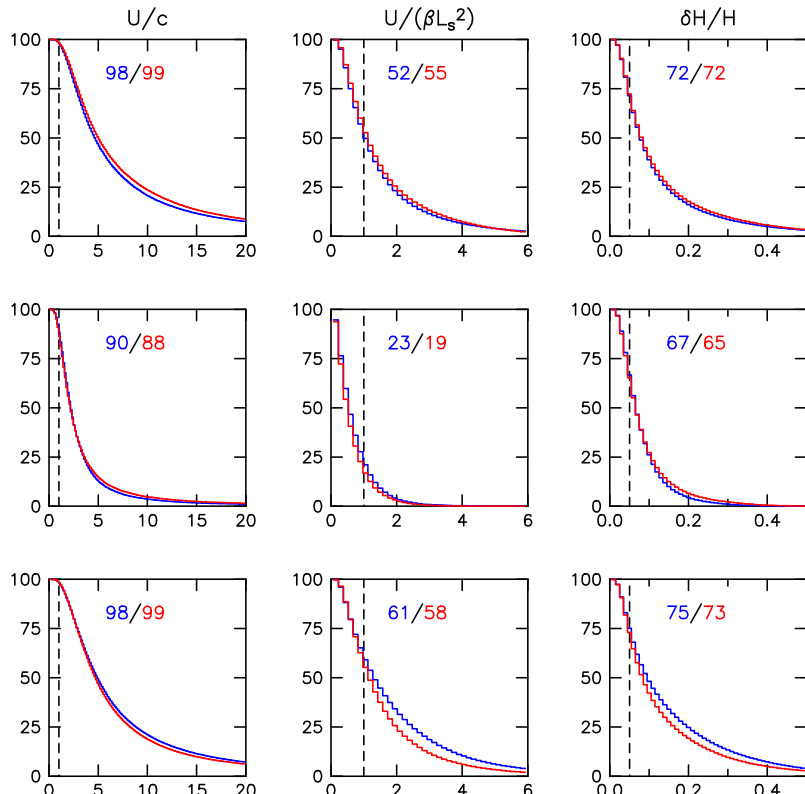


Fig. 16b. The same as Fig. 16a, except the associated upper-tail cumulative histograms for the three nonlinearity parameters in the three different latitude bands. The labels, color coded to their associated line color, indicate the percentages of eddies of each polarity for which the nonlinearity parameter exceeds the value indicated by the vertical dashed line in the respective panel.

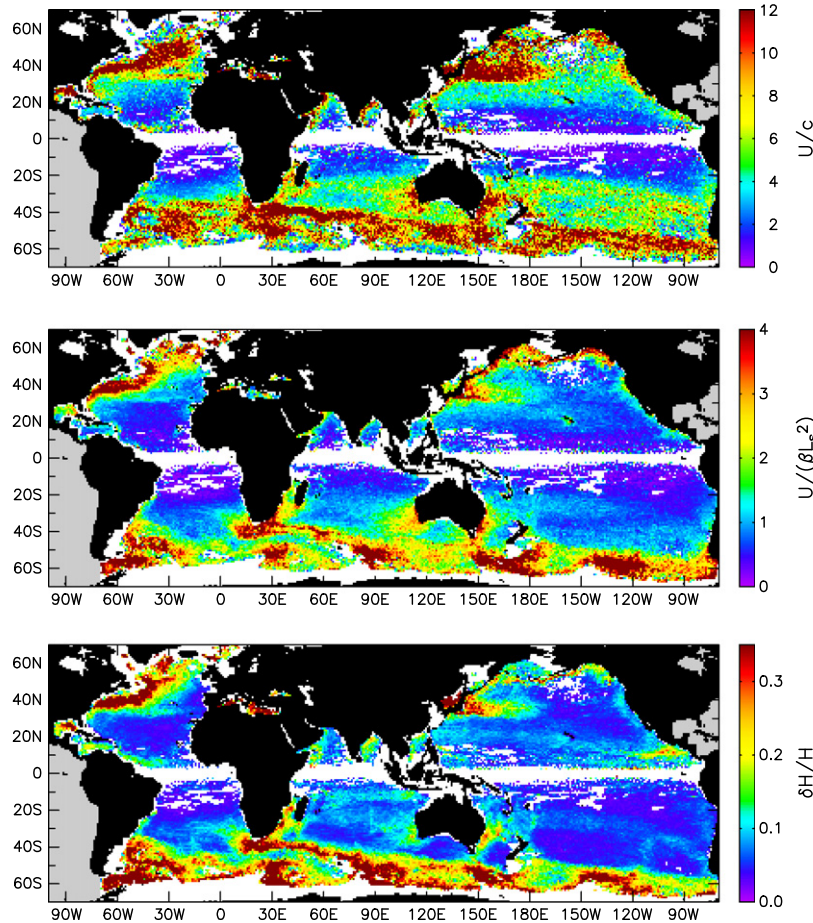


Fig. 17. Maps of the average values of the three nonlinearity parameters in Fig. 16 for each $1^\circ \times 1^\circ$ region. Top to bottom: the advective nonlinearity parameter U/c ; the quasi-geostrophic nonlinearity parameter $U/(\beta L_s^2)$; and the upper-layer thickness nonlinearity parameter $\delta H/H$.

in the region off the northeast coast of South America, and in the western boundary currents of the Arabian Sea and the Bay of Bengal.

6.2. Quasi-geostrophic nonlinearity parameter

Another measure of nonlinearity that is often used is the quasi-geostrophic (QG) nonlinearity parameter, defined to be the ratio of the relative vorticity advection to the planetary vorticity advection. Using the speed-based eddy scale L_s and maximum rotational speed U defined in Sections 4.2 and 4.3, the QG nonlinearity parameter can be characterized as $U/(\beta L_s^2)$, where $\beta = df/dy$ is the planetary vorticity gradient.

The distributions of the QG nonlinearity parameter defined in this manner are shown for the three latitude bands in the second column of Fig. 16. In the northern hemisphere extratropics, the values of $U/(\beta L_s^2)$ exceed 1 for 54% of the combined cyclonic and anticyclonic eddies. By this measure, the extratropical eddies are somewhat less nonlinear in the northern hemisphere than in the southern hemisphere where $U/(\beta L_s^2) > 1$ for 60% of the observed eddies. The mesoscale features in the tropics are less nonlinear than those in the extratropics of either hemisphere, with $U/(\beta L_s^2) > 1$ for only about 22% of the features. In all three latitude bands, these percentages agree to within a few percent for both eddy polarities.

As was the case for the advective nonlinearity parameter U/c considered in Section 6.1, the distribution of the quasi-geostrophic nonlinearity parameter $U/(\beta L_s^2)$ is more skewed toward larger values for cyclones than for anticyclones in the southern hemisphere

extratropics but the opposite is found in the northern hemisphere extratropics.

The map of the average value of the QG nonlinearity parameter in the middle panel of Fig. 17 has a geographical pattern that is generally similar to that of the advective nonlinearity parameter U/c in the top panel. Average values of $U/(\beta L_s^2) > 1$ are restricted to the same major unstable, meandering current systems as the large values of U/c discussed in Section 6.1.

6.3. Upper-layer thickness nonlinearity parameter

A third measure of nonlinearity is the upper-layer thickness nonlinearity parameter that is defined to be the ratio of thermocline displacement to its mean depth, $\delta H/H$, where H is the mean upper-layer thickness in a 2-layer approximation of the stratified ocean and $\delta H = -h/\varepsilon$ is a characteristic perturbation of the interface between the two layers associated with SSH anomaly h and nondimensional density parameter $\varepsilon = (\rho_2 - \rho_1)/\rho_2$ for upper and lower layer densities ρ_1 and ρ_2 . Perturbations of the upper-layer thickness by eddies obviously cannot be estimated rigorously from altimeter measurements of SSH. Values of the parameters H and ε of a 2-layer approximation of the climatological average density structure were estimated as summarized by Flierl (1978) from the eigenvector of the first baroclinic mode computed as described by Chelton et al. (1998) from the 2005 World Ocean Atlas climatological average hydrographic data on a 1° grid (Locarnini et al., 2006; Antonov et al., 2006) and the magnitude of δH was characterized for each eddy as A/ε , where A is the eddy amplitude.

The distributions of the upper-layer thickness nonlinearity parameter defined in this manner are shown for the three latitude bands in the last column of Fig. 16. A value of $\delta H/H = 0.1$ is a reasonable threshold above which this measure of nonlinearity can be considered significant. It is evident from Fig. 16 that $\delta H/H$ exceeds 0.1 for more than 72% of the observed eddies in the extratropics of both hemispheres (slightly higher for the southern hemisphere than the northern hemisphere). About 2/3 of the eddies in the tropical band are nonlinear by this measure.

The hemispheric asymmetries of the dependencies of the advective nonlinearity parameter U/c and the quasi-geostrophic nonlinearity parameter $U/(\beta L_s^2)$ discussed in Sections 6.1 and 6.2 is also found for the upper-layer thickness nonlinearity parameter $\delta H/H$; the distribution of $\delta H/H$ is more skewed toward large values for cyclones than for anticyclones in the southern hemisphere extratropics but the opposite is found in the northern hemisphere extratropics.

It is noteworthy that our estimates of the ratio $\delta H/H$ in the last column of Fig. 16 based on H and ε defined in terms of the climatological average hydrography as summarized above are typically four times larger than our estimates of the Rossby number $Ro = U/(fL_s)$ in Fig. 14. This suggests that many of the observed eddies may formally violate the limits of the quasi-geostrophic approximation, for which the ratio $\delta H/H$ is assumed to be of the order of Ro or less (e.g., Pedlosky, 1987).

The geographical distribution of the average value of $\delta H/H$ (bottom panel of Fig. 17) is qualitatively similar to those of the advective and QG nonlinearity parameters U/c and $U/(\beta L_s^2)$ over most of the World Ocean. Notable exceptions are the zonal bands of high values of $\delta H/H$ along the propagation paths of the previously noted eddies in the eastern tropical Pacific that are generated off the west coast of Central America, at low tropical latitudes in the South Indian Ocean from the eddies that are generated in the region between Australia and Indonesia, and along the Azores front at about 34°N across most of the North Atlantic. Other than these three areas, average values of $\delta H/H$ larger than 0.1 are restricted to the same major unstable, meandering current systems as the

large values of the other two nonlinearity parameters shown in Fig. 17.

6.4. Summary of nonlinearity

The three nonlinearity parameters considered above paint a generally consistent picture of the degree of nonlinearity of the eddies. The most highly nonlinear eddies are found in the major unstable, meandering current systems and the mesoscale features are somewhat less nonlinear in the tropics than at higher latitudes. All three measures of nonlinearity indicate that there is a preference for highly nonlinear extratropical eddies to be cyclonic in the southern hemisphere but anticyclonic in the northern hemisphere.

Of the three nonlinearity parameters considered, we feel that the advective nonlinearity parameter U/c is the most pertinent as noted previously since it determines whether an eddy can advect a parcel of trapped fluid and its associated water properties and biogeochemical characteristics.

7. Propagation characteristics

7.1. Eddy propagation directions

A striking feature of the trajectories in Figs. 4a and 4c–f is the visual tendency for nearly due-west propagation. This can be quantified from the average azimuth of each eddy trajectory, defined here as the angle with respect to due west formed by the great circle connecting the starting and ending points of the trajectory. The eddy centroid locations are somewhat noisy, either because of noise in the SSH fields of the AVISO Reference Series or because of distortions of the eddy boundaries from eddy-eddy interactions and eddy-mean flow interactions. In order to reduce the effects of this noise on the azimuth estimates, we have restricted attention to the eddies with lifetimes ≥ 16 weeks that traversed at least 10° of longitude (approximately 1000 km). The trajectories of all 4508 such eddies are shown in Fig. 18. Except in the Alaska Stream

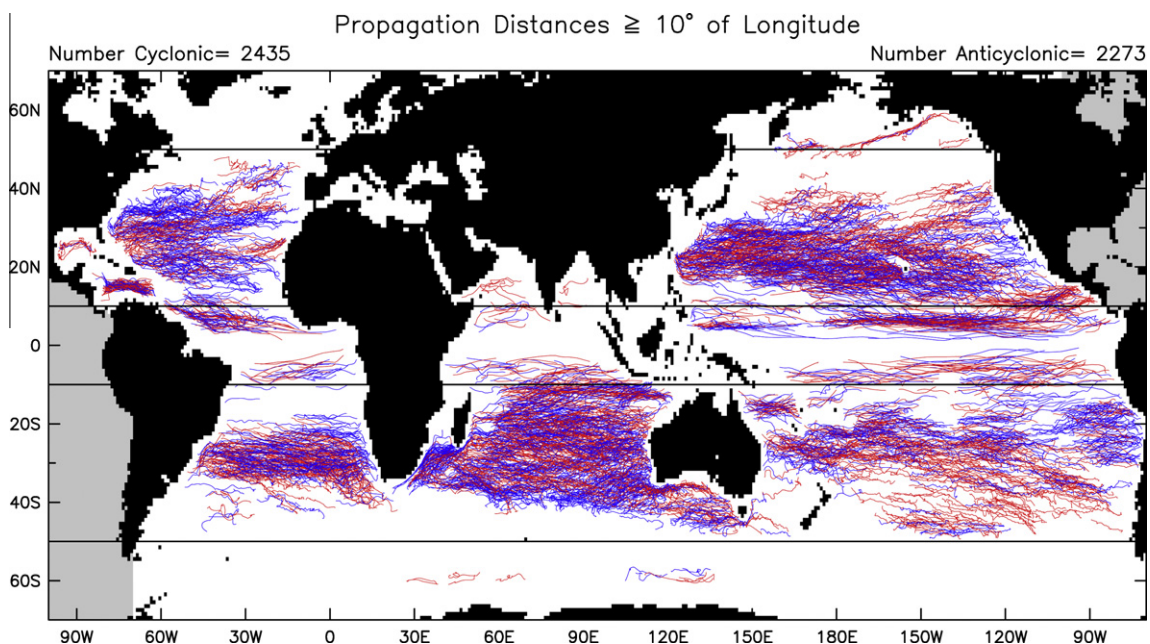


Fig. 18. The trajectories of all of the 2435 cyclonic (blue lines) and 2273 anticyclonic (red lines) eddies over the 16-year period October 1992–December 2008 that had lifetimes ≥ 16 weeks and propagated westward a minimum of 10° of longitude. The horizontal lines show the latitude ranges of 10–50° that were considered for the analyses in Figs. 19 and 20.

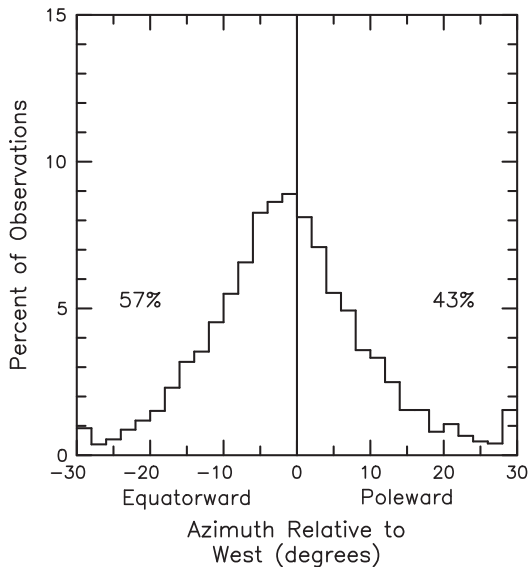


Fig. 19. The distribution of the average azimuths of the trajectories of the combined cyclonic and anticyclonic eddies with lifetimes ≥ 16 weeks and starting points at latitudes between 10° and 50° of both hemispheres that propagated westward a minimum of 10° of longitude (see Fig. 18). To combine the eddies from both hemispheres, the azimuth is defined as positive poleward and negative equatorward, rather than north and south, of due west. The labels indicate the percentages of negative (left) and positive (right) eddy azimuths. The average azimuth is defined as the angle with respect to due west formed by the great circle connecting the starting and ending points of the trajectory.

along the Aleutian Island Chain (Crawford et al., 2000), very few of the eddies north of about 50° N or south of about 50° S propagated more than 10° of longitude. We therefore excluded from this analysis any eddies that had starting points at latitudes poleward of 50° in both hemispheres. We further excluded eddies with starting points equatorward of 10° of latitude; the most energetic mesoscale features at these low latitudes are the tropical instability waves that are constrained by equatorial wave dynamics to propagate with no meridional deflection.

There were 2198 cyclonic and 2015 anticyclonic eddies that satisfied the above criteria. The distribution of the average azimuths of these 4213 eddies of combined polarities is shown in Fig. 19. Only 16% had azimuths that deviated by more than 15° from due west, thus verifying the visual impression of weak meridional propagation from Figs. 4a and 4c–f. The weak meridional drifts of mesoscale features have been noted previously by Challenger et al. (2001), Fu and Chelton (2001), Morrow et al. (2004), and Chelton et al. (2007). A noteworthy feature of Fig. 19 is the small equatorward rotation of the distribution of azimuths; the mean and median angles were, respectively, 1.1° and 1.5° equatorward of due west. A case is made below that these rotations, although small, differ significantly from zero. It is also shown that the azimuths of the combined cyclones and anticyclones are essentially symmetrically distributed about this small equatorward shift.

Previous observational studies have shown that cyclones and anticyclones have distinct preferences for poleward and equatorward deflection, respectively (Morrow et al., 2004; Chelton et al., 2007). This is confirmed here from the histograms of the average azimuths of the eddies separated by polarity in the right panels

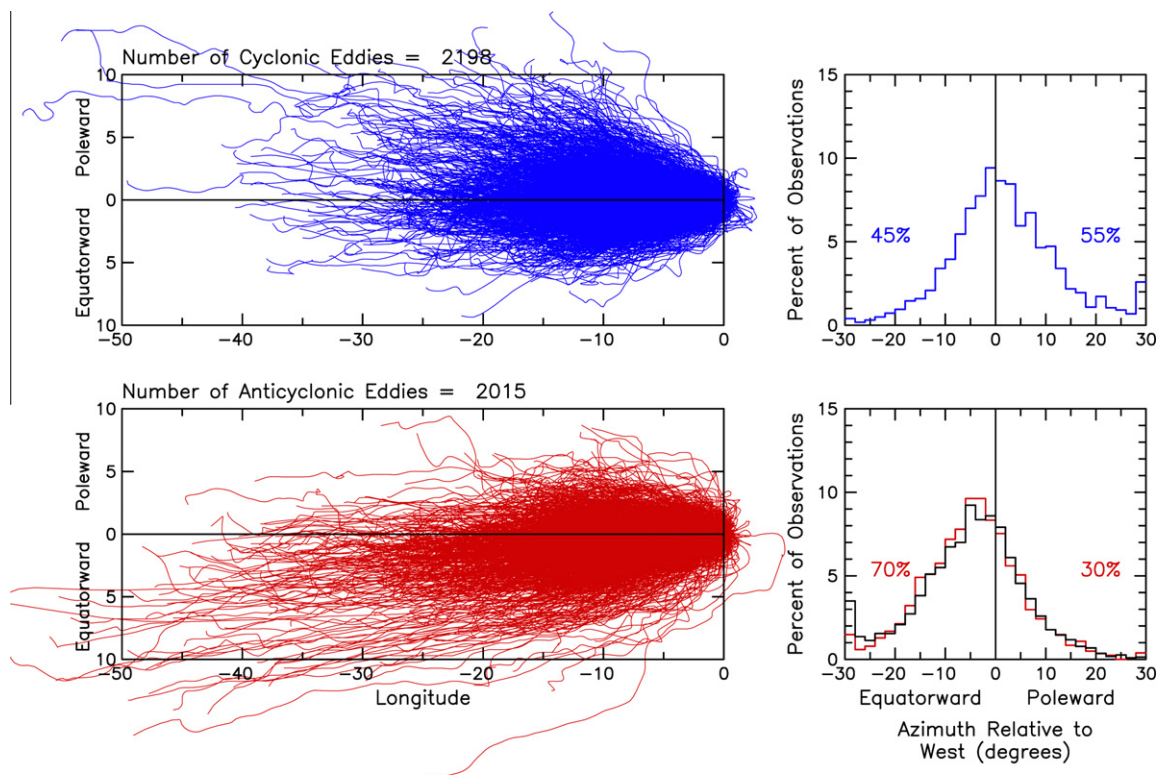


Fig. 20. The meridional deflections of the cyclonic (upper panels) and anticyclonic (lower panels) eddies with lifetimes ≥ 16 weeks and starting points at latitudes between 10° and 50° of both hemispheres that propagated westward a minimum of 10° of longitude (see Fig. 18). The left panels show the changes in longitude (negative westward) and latitude (positive for poleward and negative for equatorward of due west) relative to the initial location of each eddy. The right panels show histograms of the average azimuth of each eddy trajectory, defined as in Fig. 19. The labels in the right panels indicate the percentages of negative (left) and positive (right) eddy azimuths. The black line overlaid in the lower right panel corresponds to the histogram computed from the azimuths of the cyclonic eddies in the upper left panel that have been reflected about 0° and then shifted to have a median equal to the 4.3° equatorward median of the anticyclonic eddies.

of Fig. 20. A small opposing meridional drift of cyclones and anticyclones is expected theoretically for large, nonlinear vortices from the combined effects of the planetary vorticity gradient (the β effect) and self-advection (McWilliams and Flierl, 1979; Cushman-Roisin, 1994). Idealized quasi-geostrophic simulations (Early, 2009; Early et al., in press) suggest that the finite spreads of the distributions of azimuths in the right panels of Fig. 19 likely arise primarily from eddy-eddy interactions. Eddy-mean flow interactions may be another factor affecting the spreads of the distributions of azimuths.

The histograms in the right panels of Fig. 20 are skewed poleward for cyclones and equatorward for anticyclones with median azimuths of 1.3° poleward and 4.3° equatorward, respectively. Aside from the different medians and the sense of skewness, however, the histograms for the two eddy polarities are nearly identical mirror images of one another. This is evidenced by the black line in the bottom right panel, which is the histogram recomputed from the azimuths of the cyclonic eddies that have been reflected about 0° and then shifted 5.6° equatorward to have a median equal to the 4.3° equatorward median of the anticyclonic eddies.

Because the numbers of cyclones and anticyclones analyzed here are nearly equal, the overall median of the distribution of the azimuths of the combined cyclones and anticyclones (Fig. 19) would be equal to the mean of the individual medians for the two polarities if their distributions are identical but reflected and shifted as described above. This in turn would require that the percentage of cyclones with azimuths less (greater) than the overall median be equal to the percentage of anticyclones with azimuths greater (less) than it. These relations are indeed confirmed from the right panels of Fig. 20. The mean of the two medians is 1.5° equatorward, identical to the overall median value of 1.5° for the combined cyclones and anticyclones obtained empirically from Fig. 19. Moreover, the percentages of eddies with azimuths poleward and equatorward relative to this mean are, respectively, 62% and 38% for the cyclones and 37% and 63% for the anticyclones. These nearly identical but reversed numbers support the view that the distribution of eddy azimuths is the combination of essentially identical skewed distributions for cyclones and anticyclones, mirrored about an equatorward median of -1.5° and shifted approximately 2.8° to either side (poleward for cyclones and equatorward for anticyclones). Moreover, the mirroring of the separate distributions for the cyclones and anticyclones about the central azimuth of -1.5° implies that the distribution of the azimuths of the combined cyclones and anticyclones in Fig. 19 is symmetrically distributed.

While the median angle of the combined eddies is small, a case can be made that it is statistically significant. Consider for the sake of argument the mean azimuth of -1.1° in Fig. 19, to which Gaussian statistics apply. Because the azimuths may not be independent, a rigorous test of the hypothesis that this mean differs significantly from zero requires determination of the effective number of independent samples N^* in the set of $N = 4213$ eddies analyzed here. We determined that N^* would have to be smaller than 282, i.e., the ratio N^*/N would have to be smaller than 1/15, in order for the mean azimuth of -1.1° not to differ significantly from zero. Since it seems unlikely that N^* is this small, we conclude that the mean of -1.1° differs significantly from zero, and by inference that the median of -1.5° does as well.

As further evidence in support of our conclusion that the equatorward rotations of the mean and median azimuth angles are significant, we note that a small equatorward rotation of the median angle of the azimuths of the combined cyclones and anticyclones is a feature common to regional subsets of the data in every ocean basin, exclusive of the cyclonic eddies that form in the Leeuwin Current along the west coast of Australia that, perhaps because of their higher degrees of nonlinearity (see the top two panels of

Fig. 17), have azimuths that are much more strongly poleward than those of cyclones elsewhere in the World Ocean (see, for example, Morrow et al., 2004). We also note that the mean and median angles of the distribution of the azimuths of the trajectories of the combined cyclones and anticyclones in the Parallel Ocean Program global ocean circulation model (Maltrud and McClean, 2005) are rotated equatorward by a very similar small amount (not shown here).

For all of the above reasons, the median of 1.5° equatorward rotation of the eddy azimuths relative to due west appears to be a real feature of combined cyclonic and anticyclonic eddies. Over a zonal propagation distance of 2000 km, this corresponds to a meridional displacement of approximately 50 km. The $+2.8^\circ$ and -2.8° rotations of the separate medians of the cyclones and anticyclones, respectively, from their opposing meridional deflections relative to this overall median azimuth of -1.5° imply that the median total meridional displacements over a zonal propagation distance of 2000 km would be approximately 50 km poleward for cyclones and 150 km equatorward for anticyclones.

When the eddies are grouped into thirds according to their scales L_s , the larger eddies appear to be less prone and the smaller eddies appear to be more prone to the equatorward bias noted above; compared with the 1.5° equatorward median angle of the complete set of eddies, the median angle of the $1/3$ largest eddies decreased to 0° , whereas the median angle of the smallest $1/3$ eddies increased to 2.8° equatorward (see further discussion below). The significances of these changes are more difficult to judge because of the reduced number of samples. A similar analysis of the azimuths of the eddies with the smallest and largest $1/3$ amplitudes A found no clear dependence of the median angle on eddy amplitude.

The small but apparently significant 1.5° equatorward rotation from due west of the median angle of the azimuths of the combined cyclones and anticyclones, and the symmetry of the distributions of the cyclonic vs. anticyclonic eddy azimuths about this angle, are likely evidence of the effects of ambient conditions on the propagation directions of the eddies. The simplest such mechanism is advection by the meridional component of a mean barotropic flow. Advection by the generally equatorward flow across most of the subtropical gyres where the majority of eddies are found (see Fig. 5) would be qualitatively consistent with the observed equatorward rotation of the mean and median angles of the distribution of eddy azimuths.

Another possible mechanism for equatorward rotation of the azimuths of the combined cyclonic and anticyclonic eddies is modification of the potential vorticity gradient by vertically sheared mean flow. It is known that this shear has a significant effect on Rossby wave propagation speeds (Killworth et al., 1997; Dewar, 1998; de Szoeke and Chelton, 1999; Liu, 1999; Yang, 2000; Colin de Verdière and Tailleux, 2005) and direction (Samelson, 2010). In the absence of background mean currents, the potential vorticity gradient reduces to the planetary contribution, β , which would result in a median azimuth angle that is due west. The negligible equatorward bias of the median azimuth angle for the eddies with largest scales L_s and the increased equatorward bias for the eddies with smallest L_s noted above may be an indication that the β effect of the spherical geometry of the Earth has a greater influence, compared with the background mean currents, on the larger eddies because of their larger latitudinal spans. Alternatively, this may be from reduced eddy nonlinearity because of the smaller rotational speeds of large eddies for a given amplitude.

7.2. Eddy propagation speeds

The locations of the eddy centroids at the 7-day intervals along their trajectories also provide estimates of the eddy propagation

speeds. The variations in the centroid coordinates from one time step to the next often result in substantial deviations from westward propagation, sometimes even in “backward” propagation of a generally westward-propagating eddy. These point-to-point deviations from systematic propagation (usually westward, except in regions of strong eastward flow, see Fig. 4b) appear to be attributable primarily to distortions of the eddy structure from interactions with nearby eddies. Errors in the SSH fields may also contribute to the noisiness of the centroid locations. To mitigate the effects of this geophysical noise and mapping errors, zonal propagation speeds were estimated from local least-squares fits of the longitudes of the eddy centroids as a function of time in non-overlapping 8-week segments of each eddy trajectory. For the eddies with lifetimes ≥ 16 weeks analyzed here, this resulted in at least two independent speed estimates for each eddy.

To compare with our previous estimates of westward propagation speeds (Chelton and Schlax, 1996; Fu and Chelton, 2001) that were computed from time-longitude plots of SSH by the Radon transform (Deans, 1983), the eddy speeds were computed along the 45 zonal sections shown in Fig. 21. This is a subset of the sections that were analyzed previously, excluding the earlier sections that were equatorward of 10° of latitude where our eddy identification procedure performs less well as discussed in Section 3.3. These sections were originally selected for the early analysis of T/P data by Chelton and Schlax (1996) because they showed the clearest evidence of westward propagation over long distances from visual inspection of time-longitude sections throughout the World Ocean during the first 3 years of the T/P data record. Eddy propagation speeds are analyzed globally below. The Radon transform estimates of propagation speeds along the 45 sections in Fig. 21 are shown as function of latitude by the black dots in Fig. 22. With few exceptions, these speeds are faster than the long baroclinic linear Rossby wave phase speed (the black line in the top panel of Fig. 22), a result that agrees with the previous studies by Chelton and Schlax (1996) and Fu and Chelton (2001).

We note that our earlier analyses of westward propagation by the Radon transform were based on SSH fields that were constructed by simple smoothing of the T/P data alone, rather than by the objective analysis procedure described in Appendix A.2 that was used to construct the SSH fields of the AVISO Reference Series. We also note that the westward propagation speeds obtained from

Radon transform analysis of the SSH fields from the Parallel Ocean Program global ocean circulation model are similarly fast (see, for example, Fig. 14 of Fu and Chelton, 2001). These two results should alleviate concerns that the westward propagation speeds deduced in Fig. 22 from Radon transform analysis of the SSH fields of the AVISO Reference Series are imposed by the inclusion of propagation in the covariance function in the objective analysis procedure used by AVISO to construct these SSH fields (see Appendix A.2).

The averages of eddy propagation speed estimates within $\pm 1.5^\circ$ of latitude along the same 45 sections in Fig. 21 are shown by the red dots in Fig. 22. Each of these 45 sections included at least 75 eddy speed estimates over the 16-year data record, and most contained many more than that. These average eddy speeds are approximately 25% slower than the Radon transform estimates (Fig. 23a). The slower propagation speeds of eddies compared with the speeds inferred from the Radon transform agrees with our previous study (Chelton et al., 2007), and is also found to be the case for eddies in idealized quasi-geostrophic simulations (Early, 2009; Early et al., in press). It is evidently a robust feature of westward propagating mesoscale eddies.

The systematic differences between the eddy speeds and the propagation speeds obtained from Radon transforms reveals what we believe to be important insight into the dynamics of westward propagating mesoscale variability. Zonally low-pass filtering the $20^\circ \times 10^\circ$ high-pass filtered SSH fields with a half-power filter cut-off of 3° to attenuate the contributions of compact eddies to the variability has no significant effect on the Radon transform; the propagation speeds estimated from Radon transforms of the 3° low-pass filtered SSH along the 45 sections in Fig. 21 are virtually identical to the speeds in Fig. 22 obtained from Radon transforms without the 3° low-pass filtering (Fig. 23b). Moreover, the differences between the eddy speeds and the speeds obtained from Radon transforms of the 3° low-pass filtered SSH fields (Fig. 23c) are virtually identical to their differences from the Radon transforms without the 3° low-pass filtering (Fig. 23a). On the other hand, the eddy speeds are very similar to the propagation speeds estimated from Radon transforms of 3° high-pass filtered SSH fields (Fig. 23d).

The various relationships in Fig. 23 show that the Radon transform is effectively a low-pass filter that is insensitive to mesoscale features with wavelength scales shorter than about 3° . The faster

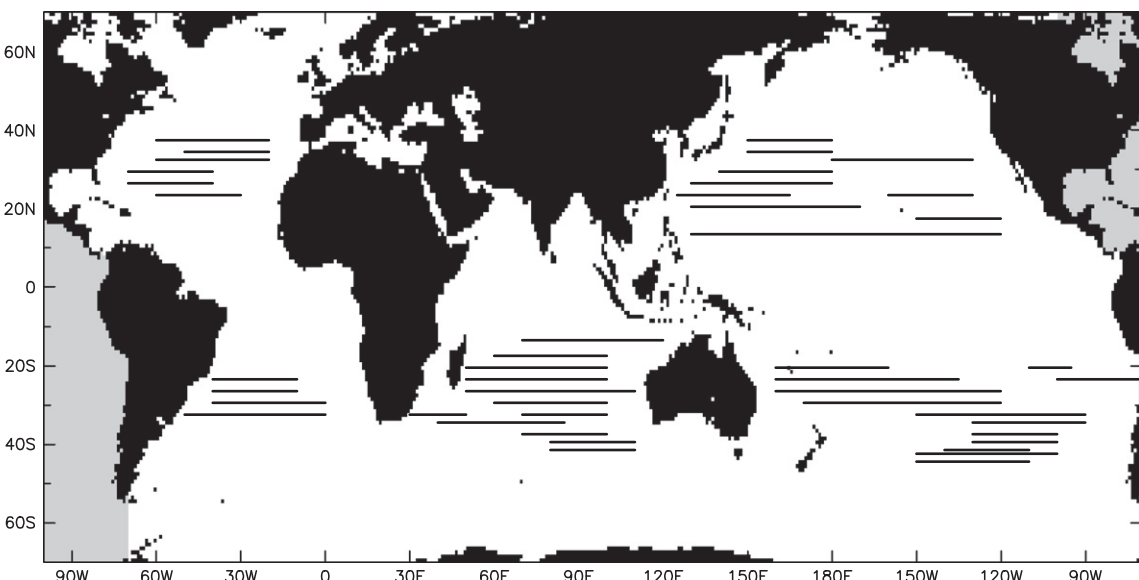


Fig. 21. The 45 zonal sections along which the Radon transform estimates of westward propagation speed and the average of the eddy speeds were computed for the black and red dots in Fig. 22. These are the same sections along which westward propagation was analyzed previously by Chelton and Schlax (1996) and Fu and Chelton (2001), except that the sections at latitudes lower than 10° have been excluded here.

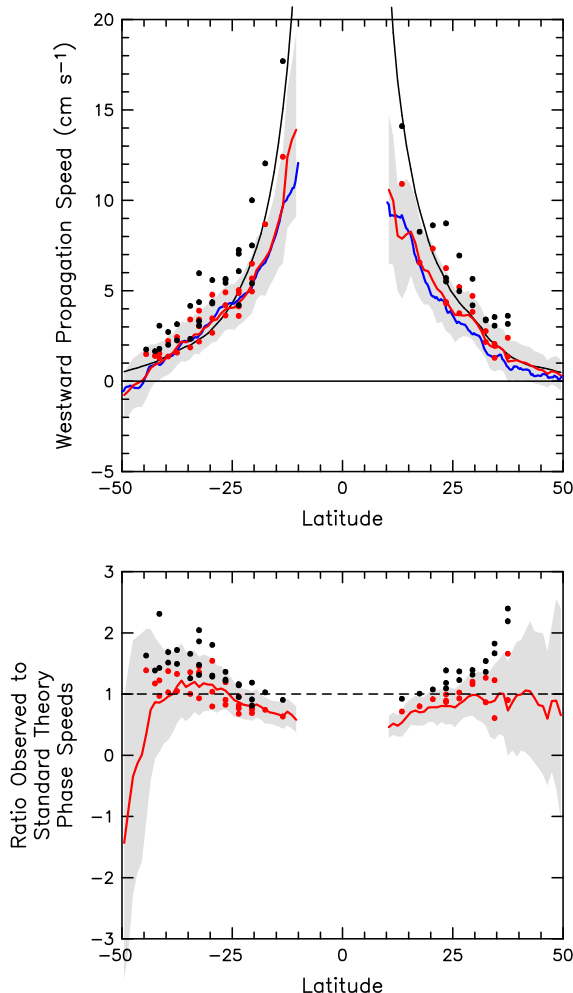


Fig. 22. The latitudinal variation of westward zonal propagation speeds estimated by a variety of different methods. The black dots are the Radon transforms of the $20^\circ \times 10^\circ$ high-pass filtered SSH fields along the 45 zonal sections shown in Fig. 21 and the red dots are the average along the propagation speeds of eddies with lifetimes ≥ 16 weeks within $\pm 1.5^\circ$ of latitude of the center latitudes of the same 45 zonal sections. The latitudinal profile of the global zonal average of the propagation speeds of all of the eddies with lifetimes ≥ 16 weeks is shown by the red line, with gray shading to indicate the interquartile range of the distribution of the eddy speeds in each latitude band. The black line is the latitudinal profile of the zonally averaged westward phase speeds of long baroclinic Rossby waves. The ratios of the various speed estimates to the local long baroclinic Rossby wave phase speed are shown in the bottom panel. The blue lines in the upper panel (barely distinguishable from the red line over much of the southern hemisphere) is the latitudinal profile of the global zonal average of the eddy propagation speeds estimated by space-time lagged cross correlation analysis by Fu (2009).

speeds obtained from the Radon transform can therefore be interpreted as an indication that features in the SSH field with scales larger than the compact mesoscale eddies that are the subject of this investigation propagate about 25% faster than the mesoscale eddies. A possible interpretation of this apparent scale dependence of propagation speed is that SSH variability consists of a superposition of nonlinear mesoscale eddies and larger-scale, linear Rossby waves that recent theories have shown should propagate faster than predicted by the classical theory because of the effects of background mean currents and bottom topography (see the discussion in Section 1). At least some, if not most, of this linear Rossby wave variability likely consists of the non-compact contributions to mesoscale variability (e.g., the interconnecting ridges and valleys between eddies arising from an up-scale energy cascade) that generally have larger scales and smaller amplitudes than the compact eddies and can therefore behave more linearly.

This speculation appears to be confirmed from the quasi-geostrophic model studies by Early (2009) and Early et al. (in press).

Aside from the speed differences reported here, we have not been able to identify an unambiguous SSH-based diagnostic to the top panel of separate nonlinear eddies from linear Rossby waves. If Rossby wave-like features are in fact detectable in the SSH fields analyzed here, they evidently have amplitudes that are small compared with the amplitudes of the nonlinear eddies.

A global summary of the propagation speeds of all of the $\sim 36,000$ eddies with lifetimes ≥ 16 weeks was obtained analogous to the 45 estimates shown by the red dots in Fig. 22 by zonally averaging all of the eddy speed estimates at 1° intervals of latitude. The latitudinal variation of these zonal averages is shown by the red lines in the two panels of Fig. 22. The gray shaded regions are the interquartile ranges of variability of the individual eddy speeds within each latitude band. From separate analyses of the propagation speeds of cyclones and anticyclones, we determined that these speed estimates do not depend significantly on eddy polarity (see, for example, Fig. 24b and c below).

The latitudinal variation of the mean eddy speed computed here from the eddy trajectories can be compared with the estimates obtained independently by Fu (2009) based on space-time lagged cross correlation analysis of SSH variability. The global zonal average of his correlation-based eddy speed estimates (the blue lines in the upper panel of Fig. 22) is almost indistinguishable from our global zonal average in the southern hemisphere. His estimates are mostly slightly slower than ours in the northern hemisphere, although well within the interquartile range of variability of our speed estimates.

The differences between the eddy speed estimates along the 45 sections in Fig. 21 that were discussed above (the red dots in Fig. 22) and the zonally averaged eddy speeds shown by the red lines suggest that this subset of speed estimates is not entirely representative of the global eddy dataset. Although slower than the speeds estimated by the Radon transform as discussed above, many of these 45 estimates are somewhat fast compared with most of the other eddies at the same latitude (the red lines in Fig. 22). This conclusion should be interpreted with some degree of caution, however, since the geographical distribution of the 45 sections in Fig. 21 is limited. Moreover, very few of these 45 eddy speed estimates exceed the interquartile range of variability shown by the gray shading in Fig. 22, and hence they are not out of the range of expected variability of the speed estimates.

An important feature of the red lines in both panels of Fig. 22 is that the zonally averaged eddy speeds are closer to the long baroclinic Rossby wave phase speed than are the faster propagation speeds estimated by Radon transforms. Except at the high southern latitudes poleward of 45°S where the ratios of the eddy speeds to the local long Rossby wave phase speeds become negative from eastward advection of the eddies by the Agulhas Return Current and the Antarctic Circumpolar Current, and in the tropical band $20^\circ\text{S}-20^\circ\text{N}$ where the speed ratios decrease to less than 1 in both hemispheres, the eddy speeds generally differ from the long baroclinic Rossby wave phase speeds by less than 20%.

The similarity of the eddy speeds to the long baroclinic Rossby wave phase speeds is consistent with theories for large, nonlinear vortices. These theories conclude that eddies with radii as large as the mesoscale eddies analyzed here and in regions where background mean currents are negligible should propagate westward with speeds approximately equal to the phase speeds from the classical theory for long baroclinic Rossby waves (McWilliams and Flierl, 1979; Killworth, 1986; Cushman-Roisin et al., 1990).

Although within the interquartile range of variability, the small but systematic trends from slightly low eddy speeds compared with long Rossby wave phase speeds at low latitudes to slightly higher eddy speeds at high latitudes that are evident in both

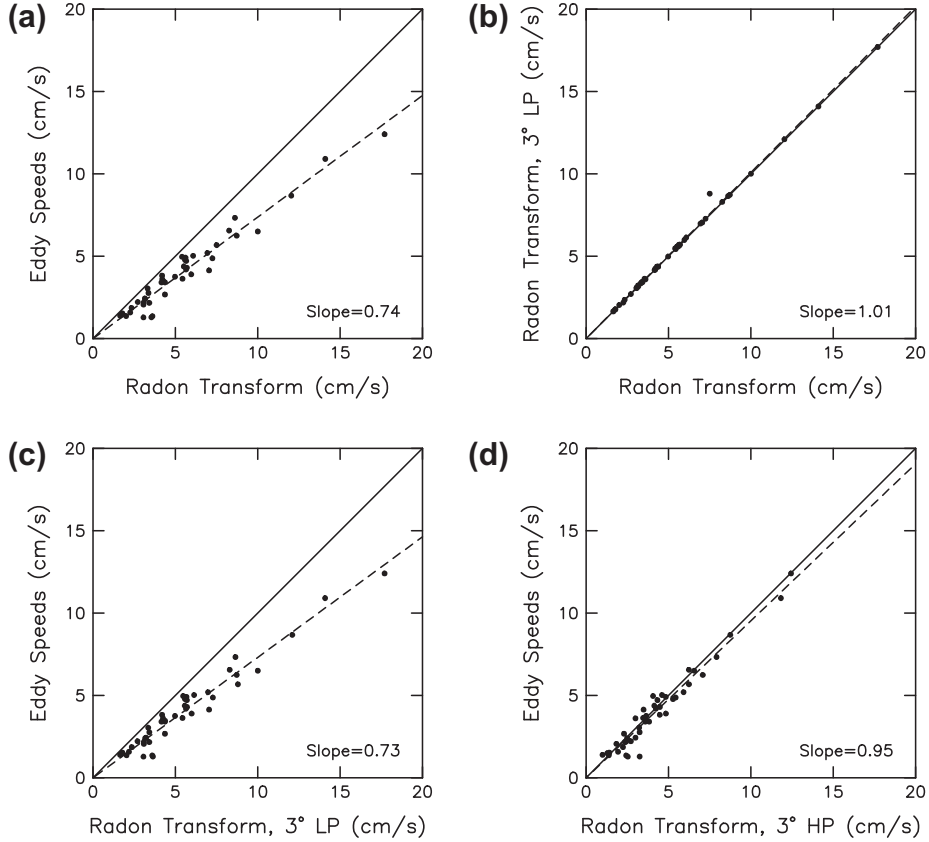


Fig. 23. Scatter plot comparisons between various estimates of westward propagation speed along the 45 zonal sections shown in Fig. 21: (a) The mean eddy speeds versus the Radon transforms of the $20^\circ \times 10^\circ$ high-pass filtered SSH fields; (b) The Radon transforms of the $20^\circ \times 10^\circ$ high-pass filtered SSH fields with 3° zonal low-pass filtering versus without 3° zonal low-pass filtering; (c) The mean eddy speeds versus the Radon transforms of the $20^\circ \times 10^\circ$ high-pass filtered SSH fields with 3° zonal low-pass filtering; and (d) The mean eddy speeds versus the Radon transforms of the $20^\circ \times 10^\circ$ high-pass filtered SSH fields with 3° zonal high-pass filtering.

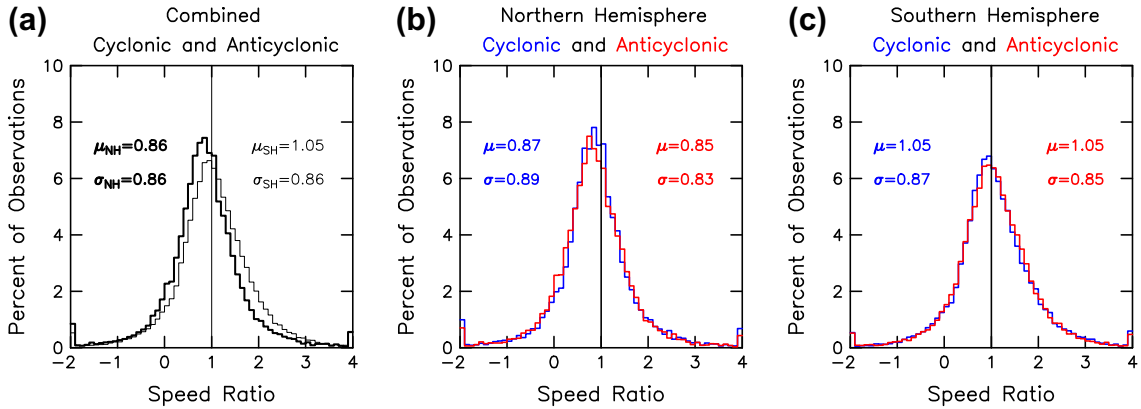


Fig. 24. Distributions of eddy speeds normalized by the local long baroclinic Rossby wave phase speed for the latitude range $15\text{--}40^\circ$. The distributions for cyclonic and anticyclonic eddies combined are shown in panel (a) for the northern and southern hemispheres as thick and thin lines, respectively. The distributions for cyclonic and anticyclonic eddies (blue and red lines, respectively) are shown separately for the northern and southern hemisphere in panels (b) and (c). The mean value μ and standard deviation σ of each distribution is labeled in each panel with lettering coded to the associated line thickness in panel (a) and the colors in panels (b) and (c).

hemispheres from the red lines in the bottom panel of Fig. 22 may be worthy of further theoretical investigation.

Another noteworthy feature of the latitudinal variation of the eddy speeds shown by the red lines in the top panel of Fig. 22 compared with the local long Rossby wave phase speeds shown by the black lines is that the eddy speeds at middle and high latitudes are consistently slower relative to the long Rossby wave phase speeds in the northern hemisphere than in the southern hemisphere. This is also evident from the space-time lagged cross correlation esti-

mates of eddy speeds by Fu (2009) (the blue lines in Fig. 22). The hemispheric differences between the eddy speeds relative to the local long Rossby wave phase speeds are shown in another way in Fig. 24a from histograms of the speed ratios for the two hemispheres separately within the latitude range $15\text{--}40^\circ$. Both distributions are approximately symmetric with the same spread (characterized here by the standard deviation) and with a mean value of 1.05 for the southern hemisphere and 0.86 for the northern hemisphere. It can be seen from Fig. 24b and c that this hemi-

spheric asymmetry is indifferent to eddy polarity. Although within the interquartile range of variability, the systematic nature of the differences between the mean eddy propagation speed ratios in the northern and southern hemispheres at all latitudes (as evident from the hemispheric differences between the red lines in Fig. 22) suggests that the ~20% hemispheric difference is likely significant. We are not able to explain this difference.

Analyses of the dependencies of eddy propagation speeds on the amplitudes and scales of the eddies reveal other interesting results. Histograms of the speed ratios for the eddies partitioned by the smallest 1/3 and largest 1/3 amplitudes A are shown in Fig. 25a and b, respectively. No significant dependence of these distributions on eddy polarity is apparent from separate histograms for cyclones and anticyclones (not shown here). It is clear, however, that the distributions of speed ratios for eddies with small amplitudes are narrower (especially in the northern hemisphere) with about 10% slower mean speeds compared with the histograms of all of the observed eddies in Fig. 24a. In contrast, the distributions of speed ratios for eddies with large amplitudes are considerably wider with about 10% larger mean speeds. These histograms thus indicate that eddies with large amplitude propagate approximately 20% faster on average, but with less consistency (larger variance), than eddies with small amplitude. A similar faster propagation speed for larger-amplitude eddies has been found in idealized quasi-geostrophic simulations (Early, 2009; Early et al., in press). Early et al. (in press) speculate that this may be attributable to “wave drag” caused by the of Rossby waves that slows the eddy propagation speed.

Histograms of the speed ratios for the eddies with the smallest 1/3 and largest 1/3 scales L_s are shown in Fig. 25c and d, respectively. There was again no apparent dependence of these distributions on eddy polarity (not shown here). The distributions of speed ratios are narrower for the eddies with large scales and wider for the eddies with small scales, indicating that eddies with large scales propagate with more consistent speed than eddies with small scales. The changes of the mean values of the distributions are less clear than for the amplitude dependence in Fig. 25a and b. In the northern hemisphere, the mean propagation speed is about 10% faster for large eddies compared with small eddies, while in the southern hemisphere the mean propagation speed is about 10% slower for the large eddies.

The dependencies of propagation speeds on amplitude and scale in Fig. 25 are perhaps surprising. Since eddies with large amplitude might be expected to have large scale as well, it might be anticipated that eddies with large amplitude would have propagation speed characteristics similar to those of eddies with large scale, and vice versa. The results of Fig. 25 show that this is not the case. In particular, while a consistent relation between the propagation speeds of eddies with large versus small amplitudes exists in both hemispheres (about 20% faster for larger eddies), the relative speeds of eddies with large versus small scales are opposite in the two hemispheres (larger-scale eddies are faster in the northern hemisphere and slower in the southern hemisphere). Likewise, the dependence of the variance of the propagation speeds on eddy amplitude is opposite the dependence of the variance of the propagation speeds on eddy scale (eddies with large amplitude have

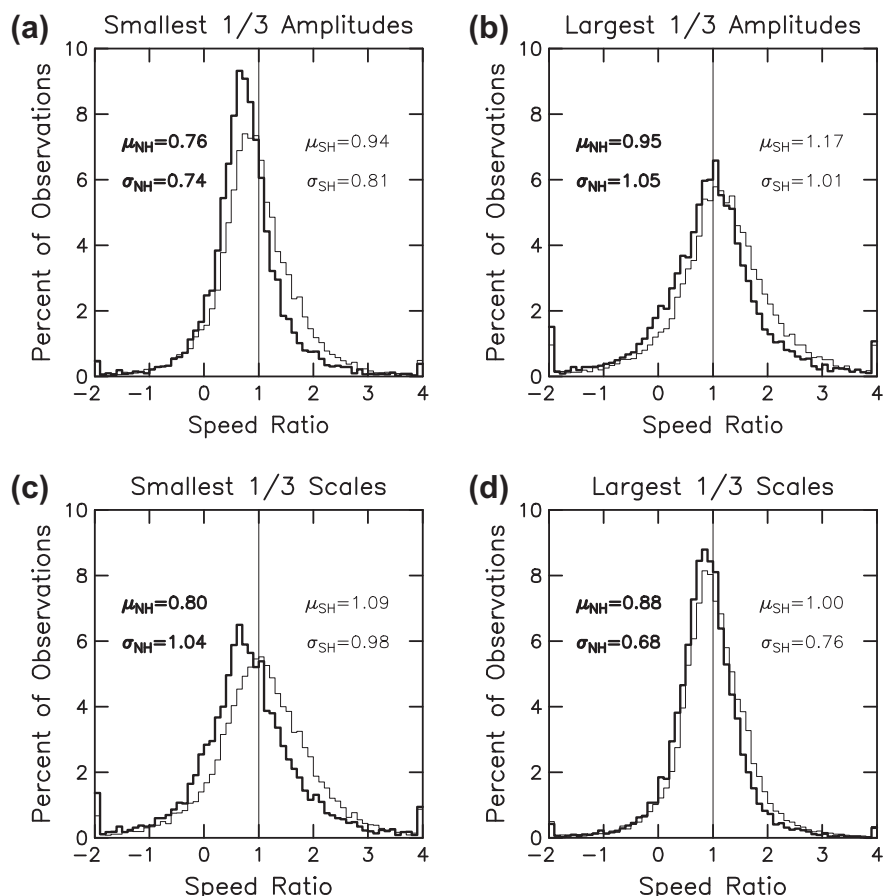


Fig. 25. The same as Fig. 24a, except separately for the eddies with (a) smallest 1/3 amplitudes A ; (b) largest 1/3 amplitudes A ; (c) smallest 1/3 scales L_s ; and (d) largest 1/3 scales L_s . In each panel, the distributions for cyclonic and anticyclonic eddies combined are shown for the northern and southern hemispheres as thick and thin lines, respectively, and the mean value μ and standard deviation σ of each distribution is labeled in each panel with lettering thickness coded to the associated line thickness.

larger speed variance while eddies with large scales have smaller speed variance). As noted previously in Section 4.2, however, the correlation between eddy amplitudes and scales is less than 0.16 at all latitudes. The different behaviors of eddies with large amplitudes and large scales are therefore not contradictory. This is likewise the case for the different behaviors of eddies with small amplitudes and small scales.

8. Summary and conclusions

The SSH fields constructed by merging the measurements from two simultaneously operating altimeters (one in a 10-day repeat orbit and the other in a 35-day repeat orbit) reveal mesoscale features with spatial scales much smaller than could be resolved from SSH fields constructed from TOPEX/Poseidon (T/P) data alone. The existence of these mesoscale features raises questions about the conclusions of numerous past studies that the strong tendency for westward propagation of SSH variability is evidence of linear baroclinic Rossby waves. Visually, these features have more compact form than is expected for linear Rossby waves. They remain coherent for long distances with little evidence of change of shape from dispersion and they exhibit a strong tendency for propagation nearly due west with little meridional deflection. The characteristics of these mesoscale features have been investigated in detail in this study to assess whether they are nonlinear. The overall conclusion is that nearly all of the observed mesoscale features outside of the tropics and most of the mesoscale features even within the tropics have rotational speeds U that are larger than their translation speeds c , and are therefore characterized by an advective nonlinearity parameter $U/c > 1$. For the purpose of discussion, these features are referred to here as eddies, thus distinguishing them from features that obey linear Rossby wave dynamics.

The dataset analyzed here is the first 16 years (October 1992–December 2008) of the $1/4^\circ \times 1/4^\circ$ global gridded version of the SSH fields of the AVISO Reference Series. An important prerequisite to the analysis presented here was the need to quantify the scales of the features that can be adequately resolved in these SSH fields. The details of the objective analysis procedure used by AVISO to produce these SSH fields are summarized in Appendix A.2. It is shown empirically in Appendix A.3 from zonal and meridional wavenumber spectra that the filtering in the objective analysis procedure used to construct the SSH fields of the AVISO Reference Series has half-power filter cutoffs of about 2° in both longitude and latitude. For Gaussian features, this corresponds to e-folding scales of about 0.4° , or roughly 40 km.

The degree to which the ~ 40 km feature resolution limitation influences the statistics of the kinematic properties of nonlinear eddies summarized in this study cannot presently be quantified from observations. The SSH fields analyzed here clearly do not resolve the submesoscale variability that has radius scales smaller than about 10 km. Nor do these SSH fields adequately resolve the lower range of the 10–500 km radius scales of mesoscale variability. Observational studies of features with scales smaller than ~ 40 km must await the launch of the next-generation altimeter, the Surface Water and Ocean Topography (SWOT) mission, which has a planned launch in 2019. SWOT will use radar interferometry to measure SSH across a swath width of 140 km with a 20 km nadir gap and is expected to have a wavelength resolution of about 10 km (Fu and Ferrari, 2008). This corresponds to an e-folding radius scale of about 2 km for Gaussian eddies.

While submesoscale features and mesoscale features with radii too small to be unambiguously detected in the dataset analyzed here are known to exist in many regions of the World Ocean, a consequence of the steep rolloff of spectral energy at high wavenumbers (small wavelengths) is that their SSH signatures are much smaller

than those of the mesoscale features that are the focus of this study. The spectral dependence of eddy kinetic energy on wavenumber k expected for geostrophic turbulence is $\sim k^{-3}$ at the highest wavenumbers (e.g., Kraichnan, 1967; Batchelor, 1969; Charney, 1971; Rhines, 1975, 1979; Stammer, 1997; Scott and Wang, 2005). This corresponds to an SSH spectral dependence of $\sim k^{-5}$, which implies that the SSH signatures are 2.5 orders of magnitude smaller for submesoscale features with wavelength scales of $O(10\text{ km})$ than for mesoscale features with wavelength scales of $O(100\text{ km})$. Even if the rolloff of the SSH spectrum is only $\sim k^{-3}$, the SSH signatures are 1.5 orders of magnitude smaller at submesoscales. We therefore believe that the dominant scales of the SSH signatures have likely been captured in the SSH fields analyzed here. Until this can be shown, however, the conclusions of this study should be treated as specific to the large eddies with scales larger than ~ 40 km that are resolvable in the SSH fields of the AVISO Reference Series.

The second prerequisite to the analysis presented here was the development of a new automated procedure for identifying and tracking mesoscale features in the SSH fields of the AVISO Reference Series. The details of the procedure and its improvements over past eddy identification procedures, including that used for our previous investigation (Chelton et al., 2007), are presented in Appendix B. Application of this procedure typically detects more than 3000 eddies globally at any given time, of which about 2400 are trackable for 4 weeks or longer (see, for example, the bottom panel of Fig. 1). In the 16-year dataset analyzed here, a total of approximately 177,000 mesoscale features were identified and tracked for 4 weeks or longer.

Limitations of the automated eddy identification procedure are discussed in Appendix C. Complications arise when eddies merge or split or become distorted from interactions with other eddies or the mean flow and from noisiness in the SSH fields arising from mapping errors. Imperfectly identified eddies are most common in regions where the mesoscale variability is most energetic, which generally corresponds to regions where the flow consists of unstable meanders that have an eddy-like character in the anomaly SSH fields analyzed here, except that their structures often deviate from, and are more transient than, the compact forms that are characteristic of isolated eddies.

To alleviate concerns that any imperfections that may exist in our eddy identification and tracking procedure could affect the general conclusions of this study, we considered only the $\sim 36,000$ eddies that had lifetimes ≥ 16 weeks. This dataset constitutes more than 1.15 million individual observations of mesoscale eddies over the 16-year data record analyzed here.

It is difficult to quantify the percentage of SSH variance that is explained by mesoscale eddies because the definition of an eddy boundary by any automated procedure that adopts a conceptual notion that eddies have compact form unavoidably excludes much of the observed mesoscale variability (see Appendix C). This is because of the practical difficulty of objectively defining the boundary of an eddy, especially when it is interacting with nearby eddies and other aspects of the flow field. The analysis in Appendix C concludes that the bias of our estimates of the amplitudes of the compact features of mesoscale variability is quite small; increasing our amplitude estimates even by just 1 cm results in eddy interiors over most of the World Ocean that have elongated structures that are very different from the compact forms that are the usual notion of what constitutes a coherent eddy. These expanded interiors often encompass multiple individual eddies and portions of the interconnecting ridges and valleys between eddies that is the spectral continuum of an up-scale energy cascade (e.g., Scott and Wang, 2005). In regions of energetic mesoscale variability, increasing our amplitude estimates by 1 cm, and sometimes by 2 cm, results in improved eddy boundaries. However, increasing our amplitude estimates by more than 2 cm is usually detrimental everywhere.

Our conclusion that SSH variability is dominated by mesoscale eddies must be qualified by noting that the SSH fields analyzed in this study were spatially high-pass filtered with half-power filter cutoffs of 20° of longitude by 10° of latitude. This filtering greatly facilitates the identification of eddy-like mesoscale features. Without spatial high-pass filtering, propagating eddies with small amplitudes can become more difficult to detect during times when they become “lost” in modulations of the background SSH variability from the steric effects of seasonal heating and cooling and other processes that affect SSH on a wide range of space and time scales. This spatial high-pass filtering likely attenuates SSH variability associated with any large-scale Rossby waves, thus biasing the conclusions of this study in favor of compact mesoscale eddies.

An important point to emphasize, however, is that all past studies that have interpreted westward-propagating SSH variability as linear Rossby waves have also relied on spatial high-pass filtering of the SSH fields; the problems of steric heating and cooling and other large-scale effects that limit the detection of compact mesoscale eddies also limit the detection of linear Rossby waves. Isolating any linear Rossby wave contributions to SSH variability in the presence of the much more energetic mesoscale eddy variability is a challenge.

The ~36,000 mesoscale features analyzed in detail in this study provide a wealth of information about mesoscale variability, some of which is in need of theoretical explanation. From considerations of numerous modifications of our automated eddy identification and tracking procedures over the past 5 years, we have concluded that the characteristics of the mesoscale eddy field presented here are quite robust and not highly sensitive to the details of the procedures.

The salient conclusions from the descriptive analysis presented in Sections 3–7 can be summarized as follows:

- (1) Approximately 3/4 of the ~36,000 eddies with lifetimes ≥ 16 weeks (Fig. 4a) propagated westward. Eastward-propagating eddies are mostly restricted to regions of strong eastward currents where advection of the eddies by these background currents is expected (Fig. 4b).
- (2) The Rossby numbers for the observed eddies are generally small (Fig. 14), justifying the use of the geostrophic approximation to estimate the fluid velocity in the eddy interiors from gridded fields of SSH.
- (3) Eddies are observed nearly everywhere in the World Ocean, with the notable exceptions of the “eddy deserts” in the northeast and southeast Pacific Ocean and a few other localized regions (Figs. 4 and 5). SSH is typically influenced by 4–6 eddies per year within the eddy-rich regions and 2–3 eddies per year in the more quiescent regions. The small numbers of tracked eddies at latitudes lower than about 10° are partly attributable to technical difficulties in identifying and tracking low-latitude eddies because of noise in the SSH fields and the combination of the fast propagation speeds, large spatial scales, and rapidly evolving structures of low-latitude eddies. The eddy identification and tracking procedure described in Appendix B.2 could be modified to improve the performance at these low latitudes, but regional tuning of the automated procedures has not been implemented for the analysis presented here.
- (4) Eddies form nearly everywhere in the World Ocean, again with the notable exceptions of the eddy deserts in the northeast and southeast Pacific and a few other localized regions (top panel of Fig. 6). Likewise, eddies terminate nearly everywhere in the World Ocean (bottom panel of Fig. 6). Formation rates are higher in the eastern boundary current regions. While the maps in Fig. 6 must be interpreted with some degree of caution because some of the apparent terminations and originations are undoubtedly from eddies that become temporarily untrackable, we believe that the geographical distributions of formation and termination locations are at least qualitatively correct in these figures. The essentially global distribution of origination locations supports the conclusions of Gill et al. (1974), Robinson and McWilliams (1974), Stammer (1998), and Smith (2007b) and others that virtually all of the World Ocean is baroclinically unstable.
- (5) The eddy amplitudes are broadly distributed (Fig. 9), with 40% of the eddies having amplitudes less than 5 cm and 25% having amplitudes greater than 10 cm. The geographical distribution of average eddy amplitudes is very similar in pattern and magnitude to the standard deviation of the $20^\circ \times 10^\circ$ spatially high-pass filtered SSH fields from which the eddies were identified (Fig. 10). The largest eddies are found in the regions of strong and unstable currents (the western boundary currents and their eastward extensions into the ocean interior, the Antarctic Circumpolar Current, and the Loop Current in the Gulf of Mexico) where the mean amplitudes can exceed 30 cm. These eddy amplitude estimates are generally found to be biased by less than 1 cm outside of regions of energetic mesoscale variability and may be biased low by 1 or 2 cm, but only occasionally by more than that, in energetic regions (Figs. C2 and C3).
- (6) The radius scales of the eddies are characterized in Section 4.2 by the scale L_s that is defined in Appendix B.3 to be the radius of a circle with area equal to that within the closed contour of SSH around which the average geostrophic speed is maximum within the eddy interior. This corresponds approximately to a contour of zero relative vorticity. Globally, more than 90% of the tracked eddies have scales L_s between 50 and 150 km (Fig. 9). The geographical distribution of the average value of L_s consists of an essentially monotonic decrease from about 200 km in the near-equatorial regions to about 75 km at 60° latitude (Fig. 12). Except in the tropics, these scales are large compared with the Rossby radius of deformation, which decreases from about 250 km to 10 km over the same latitude range (Fig. 12). The large scales of the extratropical mesoscale eddies compared with the local Rossby radius of deformation are consistent with the up-scale transfer of kinetic energy that is expected from geostrophic turbulence theory (e.g., Kraichnan, 1967; Batchelor, 1969; Charney, 1971; Rhines, 1975, 1979; Stammer, 1997; Scott and Wang, 2005).
- (7) The correlations between the amplitudes and scales of eddies are less than 0.16 at all latitudes. Eddies evidently do not have a universal self-similar structure.
- (8) Composites of doubly normalized SSH over the ~1.15 million observations show no evidence of anisotropy. Cross sections of binned averages are well approximated by a Gaussian profile over the central 2/3 of the radius L_s of the eddy (Fig. 15). However, the implied radius of maximum rotational speed for this Gaussian approximation is about 64% smaller than the observed radius L_s of maximum speed. The Gaussian approximation is therefore only qualitatively valid. The mode of the distribution of SSH values within each radius bin is well approximated by a quadratic function across essentially all of the radius L_s of the eddy (Fig. 15). The radius of maximum rotational speed for the quadratic approximation is close to the observed radius L_s of maximum speed. The quadratic approximation is thus arguably a better representation of the composite shape of the observed eddies. The mode corresponds to the most frequently occurring value at each radius and therefore

- characterizes the shapes of a substantial number of the observed eddies. A quadratic shape implies that the relative vorticity is approximately constant within the interior of an eddy. The associated fluid motion consists of approximately solid-body rotation.
- (9) Not surprisingly, eddies with small amplitude or small scale generally have short lifetimes, while eddies with large amplitude or large scale generally have longer lifetimes (Figs. 11 and 13).
- (10) Overall, there is a slight preference for cyclonic eddies (Figs. 2 and 3). For the eddies with lifetimes ≥ 16 weeks considered here, there are 6% more cyclones than anticyclones. However, there is a preference for the eddies with long lifetimes and large propagation distances to be anticyclonic (Figs. 2, 3 and 4e and f).
- (11) While there is no dependence of scale L_s on eddy polarity in either hemisphere (Section 4.2) there is a preference for eddies with amplitudes $A > 10$ cm (Section 4.1) and rotational speeds of $U > 20$ cm s $^{-1}$ (Section 4.3) to be cyclonic in the southern hemisphere (bottom left and right panels of Fig. 9b). Such asymmetries between cyclones and anticyclones are expected from the gradient wind effect of centrifugal force that pushes fluid outward and thus intensifies the low pressure at the centers of cyclones and weakens the high pressure at the centers of anticyclones. However, this cannot explain the slight preference for anticyclonic eddies for nearly all amplitudes and rotational speeds in the northern hemisphere (bottom left and right panels of Fig. 9a).
- (12) Perhaps the most significant conclusion from this study is that essentially all of the observed mesoscale features outside of the tropical band 20°S–20°N are nonlinear by the metric U/c , where U is the maximum circum-average geostrophic speed within the eddy interior and c is the translation speed of the eddy (Section 6.1). When this advective nonlinear parameter exceeds 1, an eddy can advect a parcel of trapped fluid. Many of these extratropical eddies are highly nonlinear, with 48% having $U/c > 5$ and 21% having $U/c > 10$ (Fig. 16). The highest nonlinearity is found in the regions of the major unstable, meandering currents (Fig. 17). The advective nonlinearity parameter U/c becomes smaller in the tropics where the translation speeds c become high. But even in the tropics, $U/c > 1$ for about 90% of the observed mesoscale features. The advective nonlinearity parameter U/c is especially useful for characterizing mesoscale eddies since a value of $U/c > 1$ implies that an eddy can transport heat, salt and potential vorticity, as well as biogeochemical properties such as nutrients and phytoplankton. The observed nonlinear eddies can thus have important influences on heat flux and marine ecosystem dynamics, in addition to their well-established importance in momentum and energy fluxes.
- (13) Consideration of the quasi-geostrophic nonlinearity parameter $U/(\beta L_s^2)$ and the upper-layer thickness nonlinearity parameter $\delta H/H$ estimated as described in Sections 6.2 and 6.3, respectively, leads to the conclusion that most of the observed eddies are nonlinear by these metrics as well (Figs. 16 and 17).
- (14) By all three measures of nonlinearity considered here, there is a preference for highly nonlinear extratropical eddies to be cyclonic in the southern hemisphere but anticyclonic in the northern hemisphere. This is consistent with the hemispheric asymmetries of the dependencies of amplitudes and rotational speeds on eddy polarity noted in item 11 above.
- (15) The propagation directions of the observed eddies are nearly due west (Figs. 19 and 20). Of the eddies that propagated zonally by more than 10° of longitude, only 16% had azimuths that deviated by more than 15° from due west. Idealized quasi-geostrophic simulations (Early, 2009; Early et al., in press) suggest that the finite spreads of the distributions of azimuths likely arise primarily from eddy-eddy interactions. There are systematic preferences for small poleward and equatorward deflections of cyclones and anticyclones, respectively. The distributions of the azimuths of cyclones and anticyclones are essentially identical, except that they are mirror images of each other. These mirrored distributions are significantly skewed and are shifted 2.8° to either side of a median azimuth that is rotated 1.5° equatorward of due west. Although small, it is argued in Section 7.1 that this rotation of the central azimuth of the combined cyclonic and anticyclonic eddy trajectories differs significantly from zero and is likely attributable to the effects of ambient currents on the propagation directions of eddies, either by meridional advection by a mean barotropic flow or by the effects of vertical shear on the potential vorticity gradient vector. Eddies with large horizontal scales are less prone to this equatorward rotation of the central azimuth of the eddy trajectories.
- (16) The propagation speeds of the observed eddies are close to the local phase speed of long baroclinic Rossby waves. There is no apparent dependence of the propagation speeds on eddy polarity (Fig. 24b and c). However, compared with the local long Rossby wave phase speed, the eddy speeds in the southern hemisphere are about 20% faster than in the northern hemisphere (Figs. 22, 24 and 25), which we believe to be a statistically significant difference.
- (17) There are subtle but probably significant dependencies of the characteristics of the propagation speeds on eddy amplitude and scale (Fig. 25). Perhaps the most important of these is that eddies with large amplitudes propagate about 20% faster than those with small amplitudes. A similar dependence of propagation speed on eddy amplitude has been found in idealized quasi-geostrophic simulations (Early, 2009; Early et al., in press). This may be evidence of the effects of “wave drag” caused by the shedding of Rossby waves that slows the eddy propagation speed (Early et al., in press).
- (18) The nearly due-west propagation with small opposing meridional deflections of cyclones and anticyclones and with propagation speeds nearly equal to the long baroclinic Rossby wave phase speed in items 14–16 above are all consistent with theoretical expectations for large, nonlinear vortices on a β plane (McWilliams and Flierl, 1979; Killworth, 1986; Cushman-Roisin et al., 1990; Cushman-Roisin, 1994).
- (19) The eddy propagation speeds are about 25% slower than the propagation speeds estimated from Radon transforms of time-longitude plots of SSH (Figs. 22 and 23). It is shown in Section 7.2 that the Radon transform is effectively a low-pass filter that responds preferentially to the large-scale features in the SSH field. The faster speeds deduced from Radon transforms thus imply that features in the SSH field with scales larger than the mesoscale eddies analyzed in this study propagate faster than the eddies. A similar discrepancy between the propagation speeds of eddies and the larger-scale features tracked by the Radon transform is found in idealized quasi-geostrophic simulations (Early, 2009; Early et al., in press). This scale dependence of propagation speed is suggestive of dispersion and may be evidence for the existence of linear baroclinic Rossby waves (or more precisely, features that obey linear Rossby wave dynamics) that have propagation characteristics distinct from the mesoscale eddy field. Investigating such linear Rossby wave-like features in the presence of the much more energetic fields of

nonlinear mesoscale eddies is a challenge. Aside from the speed differences reported here, we have not been able to identify an unambiguous SSH-based diagnostic to isolate Rossby wave-like signals. Most of these linear or quasi-linear features in the spatially high-pass filtered SSH fields analyzed here appear to be the non-compact contributions to mesoscale variability from the interconnecting ridges and valleys between eddies arising from the up-scale energy cascade. The difficulty in distinguishing the contributions of linear features to SSH variability from the much more energetic nonlinear eddy field may be in part attributable to the tendency for large-scale Rossby waves to become unstable and break down into small-scale eddies at middle and high latitudes (Gill, 1974; LaCasce and Pedlosky, 2004; Isachsen et al., 2007).

The wealth of information about mesoscale eddies summarized above based on the unprecedented coverage of the SSH characteristics of mesoscale eddies provided by the 16-year merged dataset produced by AVISO is enabling studies of the kinematics and dynamics of mesoscale variability that have not previously been possible. The results presented in this study provide a framework for dynamical interpretations of mesoscale eddy variability. As noted in items 15, 17 and 19 above, recent idealized numerical modeling of eddy dynamics motivated by the observations reported here supports the interpretation of the tracked eddies as nonlinear, coherent structures (Early, 2009; Early et al., in press). These modeling results include quasi-geostrophic simulations that, despite the significant upper-layer thickness perturbations suggested from our estimates in Figs. 16 and 17, provide compelling representations of many aspects of the observed eddy properties.

Our ongoing efforts are applying this eddy dataset to investigate a variety of scientific questions, including the dispersion characteristics of the observed mesoscale features based on wavenumber-frequency spectral analysis; seasonal and interannual variations of the characteristics of the tracked eddies and their dynamical implications; the geographical distributions of sea-surface temperature and chlorophyll within our SSH-based definition of the eddy interiors; and the influence of the surface geostrophic velocity field within the eddy interiors on the air-sea momentum flux (i.e., the surface wind stress, which is determined from the relative motion between surface winds and surface ocean currents). The numerous differences between northern and southern hemisphere eddies noted from the analyses presented here are also of interest (e.g., the hemispheric differences between the dependencies of amplitude, rotational speed and nonlinearity on eddy polarity, the opposing dependencies of propagation speed on eddy scale in the two hemispheres, and the overall ~20% faster propagation speeds of eddies in the southern hemisphere compared with the local long Rossby wave phase speed). This is a small sampling of the wide range of possible applications of this rich eddy dataset.

We close by noting that many of the important questions about the significance of mesoscale eddies in ocean dynamics and thermodynamics, as well as their role in marine ecosystem dynamics, require subsurface information as well as the surface information provided by satellite altimetry. These questions are being addressed in ongoing research from analysis of the altimeter data in combination with subsurface float observations and from the Parallel Ocean Program global ocean circulation model (Maltrud and McClean, 2005). As noted in Sections 5 and 7, the shapes, propagation directions and propagation speeds deduced here from analysis of the SSH fields from the AVISO Reference Series are all well represented in this model. The results of these analyses of model eddies will be reported elsewhere along with an analysis of the vertical structures of the eddies in the model.

Acknowledgments

We thank Lee-Leung Fu, Jim McWilliams and an anonymous third reviewer for their thorough and constructive formal reviews of this paper. We are grateful to Gerald Dibarboure for clarifying the details of the AVISO objective analysis procedure that are summarized in Appendix A.2. We also thank Tom Farrar, Brian Arbic, Curt Collins and Thierry Penduff for their detailed and helpful comments on the manuscript. This research was funded as part of the NASA Ocean Surface Topography Mission through NASA Grant NNX08AR37G. The merged altimeter data analyzed here were produced by the DUACS (Developing Use of Altimetry for Climate Studies) multi-mission altimeter data processing system, which is part of the multi-mission ground support system SSALTO (Segment Sol multimissions d'ALTImétrie, d'Orbitographie et de localisation précise) that is operated by the French space agency CNES (Centre National d'Etudes Spatiales) in partnership with CLS (Collecte Localis Satellites) in Toulouse, France. The SSALTO/DUACS merged altimeter data are distributed by CLS/AVISO (Archivage, Validation, Interprétation des données des Satellite Océanographiques), and are referred to by AVISO as the Reference Series. Except for the left panels of Fig. A3 for reasons explained in the figure caption, the analysis presented here was based on the 1/4° latitude by 1/4° longitude gridded fields that were produced by AVISO by bilinear interpolation from the original Mercator grid with a nominal spacing of 1/3°.

Appendix A. The resolution capability of the merged dataset

A.1. Resolution capability of the TOPEX/Poseidon sampling pattern

For interpretation of variability in SSH fields constructed from altimeter observations, it is important to know the scales of the features that can be resolved. We have addressed the question of resolution capability for the sampling patterns of various combinations of single and double altimeter missions in a series of studies culminating with Chelton and Schlax (2003), hereafter referred to as CS03, wherein the smoothing and gridding of altimeter observations of SSH onto an arbitrary latitude-longitude grid is considered for single and double altimeter missions. Resolution as defined by CS03 is based on a subjective judgment of the level of tolerance for the overall magnitude and the spatial and temporal inhomogeneity of mapping errors in the gridded SSH fields. The eddy identification and tracking procedure used in this study to investigate mesoscale variability is a demanding application of smoothed SSH fields. Excessive smoothing attenuates the mesoscale features of interest. Insufficient smoothing leaves residual artifacts in the SSH fields that can be mistakenly interpreted as mesoscale eddies and can also cause modulation of eddy amplitudes as they propagate across regions of alternately sparse and dense sampling, which imply low and high spatial resolution, respectively.

CS03 conclude that the wavelength resolution capability of SSH fields constructed from T/P data alone is approximately 6° in longitude by 6° in latitude by 20 days. Less smoothing than this results in spatial inhomogeneity of the mapping errors. The highest resolution and smallest errors are found at the crossovers of the ascending and descending ground tracks of the T/P satellite. The lowest resolution and largest errors are found at the centers of the diamond-shaped regions between the ground tracks. A simulated one-dimensional analog that makes the effects of such inhomogeneity of resolution and errors clear is shown in Fig. 6 of Chelton and Schlax (1994).

The perhaps surprisingly coarse wavelength resolution of $6^\circ \times 6^\circ \times 20$ days is readily confirmed empirically from the maps and zonal sections of SSH standard deviation in the top three rows

of Fig. A1. The $5^\circ \times 5^\circ \times 20$ -day smoothing used in the upper panels is clearly insufficient, as evidenced by the spatial inhomogeneity of the standard deviation. The checkerboard patterns of SSH standard deviation in the map and the oscillating structures in the two zonal sections along crossover latitudes coincide with

the longitudinal spacing of the ground tracks of the T/P satellite. The standard deviation is relatively low inside the unsampled diamonds where only the large-scale features in SSH can be resolved by the T/P ground track pattern. Westward propagating features in these insufficiently smoothed SSH fields therefore modulate from

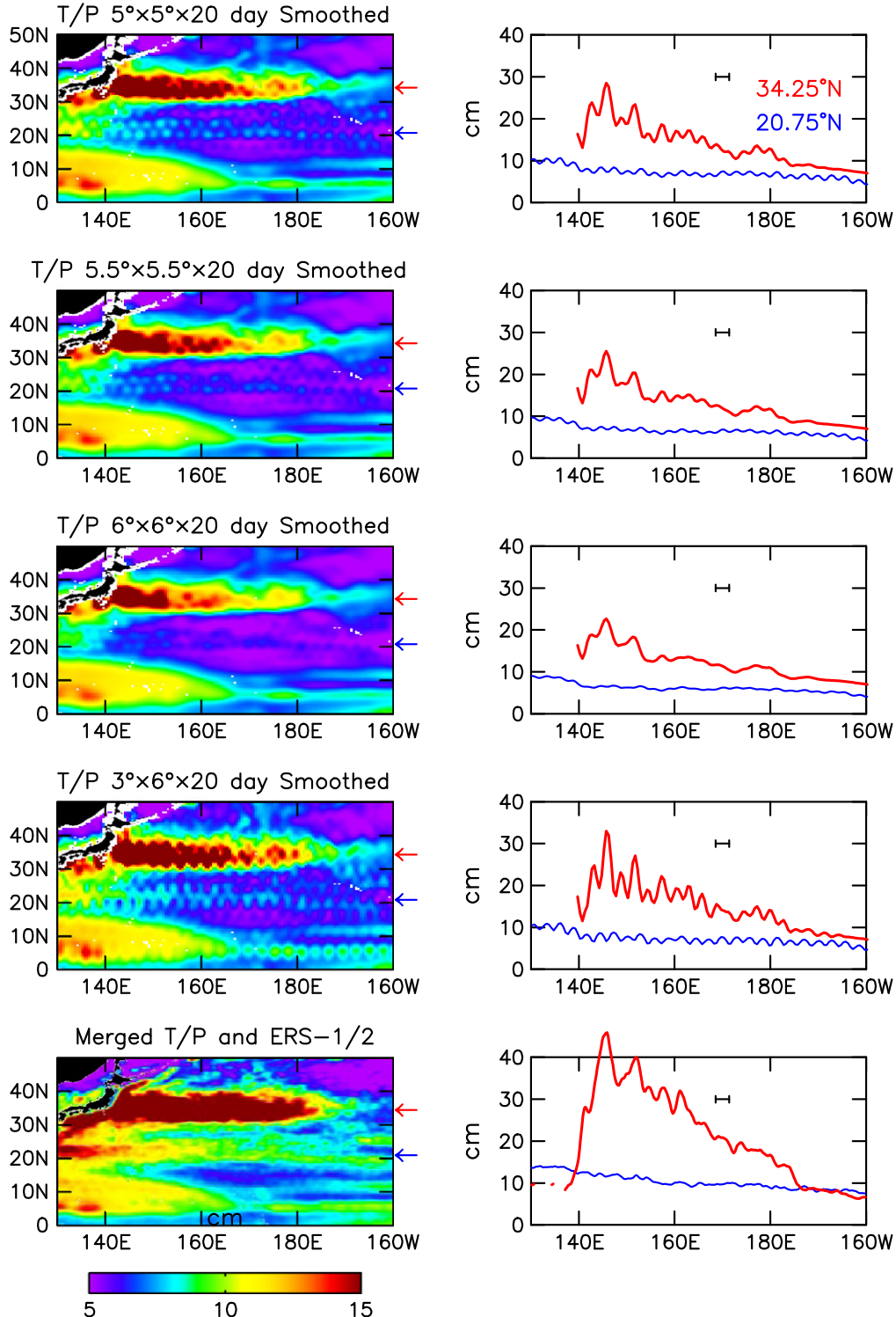


Fig. A1. Maps (left panels) and zonal cross sections along the latitudes 34.25°N and 20.75°N of T/P ground track crossovers (right panels) of the standard deviation of gridded SSH fields constructed from altimeter data with various amounts of smoothing with a three-dimensional loess smoother (cf., Chelton and Schlax, 2003). Top to bottom: T/P data with $5^\circ \times 5^\circ \times 20$ -day smoothing; T/P data with $5.5^\circ \times 5.5^\circ \times 20$ -day smoothing; T/P data with $6^\circ \times 6^\circ \times 20$ -day smoothing; T/P data with $3^\circ \times 6^\circ \times 20$ -day smoothing; and the SSH fields of the AVISO Reference Series with no additional smoothing applied. The horizontal bar in each of the right panels is the zonal spacing of the crossovers of ascending and descending T/P ground tracks. The red and blue arrows along the right border of each map indicate the latitudes of the zonal sections in the right panels. The T/P data in the top four rows are smoothed onto a $0.5^\circ \times 0.5^\circ$ grid and the standard deviations are calculated from 9.5 years of gridded data. The merged dataset in the bottom row is on a $1/4^\circ \times 1/4^\circ$ grid and spans the 16-year period October 1992–December 2008.

larger amplitudes near crossovers where higher resolution is possible to smaller amplitudes near diamond centers where the resolution is poor. Features with small amplitude and/or small horizontal scale can become untrackable in the diamond centers. Their later reappearance near a crossover would be erroneously interpreted as a newly formed eddy. Such behavior is clearly problematic for automated eddy tracking.

With $5.5^\circ \times 5.5^\circ$ smoothing (second row of panels in Fig. A1), the checkerboard patterns of SSH standard deviation in the map and the oscillating structures in the zonal sections are reduced but are still readily apparent. The transition from inadequate to adequate smoothing occurs quite abruptly for smoothing larger than $5.5^\circ \times 5.5^\circ$. With the $6^\circ \times 6^\circ$ smoothing advocated by CS03 (third row of panels in Fig. A1), the checkerboard patterns in the standard deviation are essentially eliminated. The reason for this abrupt transition is that the span of the spatial smoother becomes large enough with $6^\circ \times 6^\circ$ smoothing to include measurements in all directions for smoothed estimates of SSH at every location globally.

Using a different approach, Tai (2004, 2006) concludes that SSH fields with wavelength resolution higher than $6^\circ \times 6^\circ$ can be constructed from the T/P sampling pattern by a least-squares estimation procedure that smooths the along-track observations onto a grid consisting of the midpoints along the ground tracks half way between crossover points. In practice, essentially the same result can be achieved more simply by averaging the individual measurements along the track segments between crossovers (Tai, 2009). The resulting smoothed SSH fields on the grid of midpoints are capable of midlatitude wavelength resolutions of about 3° in longitude by 6° in latitude. However, this resolution is not valid for SSH fields constructed by smoothing the observations directly onto an arbitrary grid. This is evident in the fourth row of panels of Fig. A1 from the pronounced checkerboard patterns in the map and the oscillating structures in the zonal cross sections of standard deviation with $3^\circ \times 6^\circ \times 20$ -day smoothing onto a $0.5^\circ \times 0.5^\circ$ grid.

The grid consisting only of midpoints advocated by Tai (2004, 2009) is too coarse for the eddy identification and tracking procedure summarized in Appendices B.2–B.4 that was applied for this investigation of mesoscale variability. It may be possible to interpolate the smoothed SSH estimates at the midpoints onto a higher resolution grid, but such fields have not yet been produced.

A.2. Summary of the AVISO processing details

The analysis of CS03 summarized in Appendix A.1 was based on the filtering properties of the loess smoother (Cleveland and Devlin, 1988; Schlax and Chelton, 1992; Chelton and Schlax, 2003). In order to estimate the resolution of the merged altimeter dataset analyzed in this study that were produced by SSALTO/DUACS from two simultaneously operating altimeters and are distributed and referred to by AVISO as the Reference Series,¹ it is necessary to determine the filtering properties of the objective analysis procedure that was used by AVISO to produce the SSH fields. The de-

tails of this procedure have evolved somewhat over the years and an up-to-date and comprehensive documentation of the procedure is not available. Many of the details are described in a sequence of published papers: Le Traon et al. (1995, 1998, 2003), Le Traon and Ogor (1998), and Ducet et al. (2000). Since the processing details could conceivably impact the interpretation of the mesoscale variability deduced in this study from the SSH fields of the AVISO Reference Series, we summarize here our understanding of the procedure as it has most recently been implemented. In addition to the above publications, this summary is based on personal communication in December 2010 with G. Dibarbour at CLS in Toulouse, France who presently oversees the AVISO processing.

To make the SSH measurements from the two altimeters that contribute to the SSH fields more compatible, the larger orbit errors of the satellite in the 35-day repeat orbit (ERS-1, followed by ERS-2 and presently by Envisat) were mitigated through a cross-over adjustment of the altimeter range measurements with those from the concurrent satellite in the 10-day repeat orbit that had smaller orbit errors (T/P, followed by Jason-1 and presently by Jason-2). Along-track mean profiles of SSH were then computed over the full life span of each satellite sensor and were then adjusted to the 7-year period 1993–1999 based on cross calibrations of the various altimeter datasets during the overlaps of successive altimeter data records. For each contributing satellite, the associated mean profile was then subtracted from the SSH profile in each exact repeat period to obtain along-track profiles of anomaly SSH.

To reduce measurement noise and computational load, the along-track anomaly SSH values were spatially low-pass filtered along track and subsampled using a Lanczos filter with a latitudinally dependent half-power filter cutoff wavelength that varied from about 250 km near the equator to 60 km at latitudes higher than 40° . The subsampling rate varied with latitude in a manner commensurate with the filtering scales. These smoothed and subsampled anomaly SSH values were then mapped onto a $1/3^\circ$ Mercator grid using a covariance-based objective analysis procedure that is referred to as suboptimal interpolation because only data within a region of influence slightly smaller than the spatial and temporal scales of the covariance function (see below) contribute to the estimate.

The covariance function used to represent SSH in the objective analysis procedure is the product of a cubic polynomial and an exponential in latitude and longitude, further multiplied by a Gaussian in time. Temporal scales, zonal and meridional spatial scales, and zonal and meridional propagation speeds are incorporated in this covariance function (cf., the un-numbered equation in section 2d of Le Traon et al., 2003). Zonal scales (defined to be the zero crossing of the covariance) vary latitudinally from about 300 km near the equator to less than 100 km at high latitudes; meridional scales (the zero crossing as well) also vary latitudinally and are slightly smaller than the zonal scales. The zonal propagation speeds vary geographically and are comparable to the theoretical value for long baroclinic Rossby waves, generally decreasing from about 30 cm s^{-1} westward in the near-equatorial regions to about 1 cm s^{-1} westward at high latitudes, but are eastward by as much as a few cm s^{-1} in some of the midlatitude eastward jets (e.g., the Antarctic Circumpolar Current and the Gulf Stream). The meridional propagation speeds are small over most of the World Ocean.

The e-folding time scale of the covariance function in the objective analysis procedure varies at each $1/3^\circ$ Mercator grid point and is approximately 35 days over the regions between about 15° and 50° latitude where most of the mesoscale eddies are observed (Fig. 5), decreasing to about 10 days in the tropics where the propagation speeds are fast and eddies evolve quickly, and in the high-latitude regions where the eddies tend to be transient. The choice of the 4-week minimum lifetime for the eddies retained from the

¹ The analysis presented in this study is based on the version of the AVISO Reference Series that was available in October 2009 and included SSH fields for the time period 14 October 1992 through 31 December 2008. A reprocessed version of these SSH fields was released in September 2010, which incorporated numerous improvements (see the documentation on the AVISO website) and extended the time series through March 2010. A preliminary analysis of the results of applying the automated eddy identification and tracking procedure described in Appendices B.2–B.4 to this new dataset found that none of the conclusions of this study are changed. It is noteworthy, however, that the new dataset yields a few percent more eddies for all lifetimes, presumably because of reduced noise in the improved SSH fields. For the lifetimes ≥ 16 weeks that are the focus of this study, for example, there are 763 more eddies (36,654, compared with 35,891 in the older dataset analyzed in this study).

automated identification and tracking procedure summarized in Appendices B.2–B.4 is commensurate with the ~35-day e-folding time scale of the objective analysis procedure in the eddy-rich regions.

In addition to the above features, the covariance matrix used in the objective analysis procedure incorporates the following elements:

1. White measurement noise appropriate for each contributing altimeter (larger for ERS-1, ERS-2 and Envisat than for T/P, Jason-1 and Jason-2).
2. Long-wavelength measurement noise from residual orbit errors appropriate for each contributing altimeter (again larger for ERS-1, ERS-2 and Envisat than for T/P, Jason-1 and Jason-2).
3. White noise in the covariance function in the form of a noise-to-signal variance ratio of 10%, which is included to account for the small-scale variability that cannot be resolved by the sampling pattern of the two simultaneously contributing altimeters.

The spatial resolution of the SSH fields is controlled primarily by three factors: (1) the along-track smoothing; (2) the spatial smoothing imposed by the zonal and meridional length scales of the covariance function; and (3) the noise-to-signal variance ratio of 10% used in the objective analysis procedure.

Since the algorithm is linear in the input data, the spatial filtering properties of the covariance-based objective analysis procedure could in principle be quantified by determining the equivalent transfer function of the procedure as summarized by Schlax and Chelton (1992). As the precise parameters of the procedure vary geographically in complicated ways at each 1/3° Mercator grid point, synthesis of the results would be difficult. Rather

than attempt a grid point by grid point description, the zonal and meridional spatial filtering properties of the objective analysis procedure used to construct the SSH fields of the AVISO Reference Series are determined empirically in Appendix A.3 from zonal and meridional wavenumber spectral analysis of the gridded SSH fields. The conclusion of this spectral analysis is perhaps surprising and not at all obvious from the complicated details of the objective analysis procedure summarized above: When characterized in degrees of longitude and latitude, the spatial resolution appears to be essentially isotropic and geographically homogeneous.

A.3. The spatial resolution capability of the SSH fields of the AVISO reference series

The spatial filtering properties of the objective analysis procedure used by AVISO to produce the SSH fields of the Reference Series (see Appendix A.2) are empirically quantified in this section using a wavenumber spectral analysis of these SSH fields. One-dimensional wavenumber spectra were computed for broad expanses of the midlatitude North and South Pacific oceans. Zonal wavenumber spectra were computed along the 15 sections spanning 60° of longitude shown by the heavy lines in Fig. 27. Meridional wavenumber spectra were computed along the 16 sections spanning 35° of latitude shown by the thin lines in Fig. A2. Spectra were computed along each of these 31 sections at weekly intervals over the 16-year duration of the AVISO Reference Series and ensemble averaged to obtain a smoothed spectrum for each section.

The resulting 15 zonal and 16 meridional smoothed wavenumber spectra are superimposed in the upper left and right panels of Fig. A3, respectively, for wavenumber in units of cycles per km. For

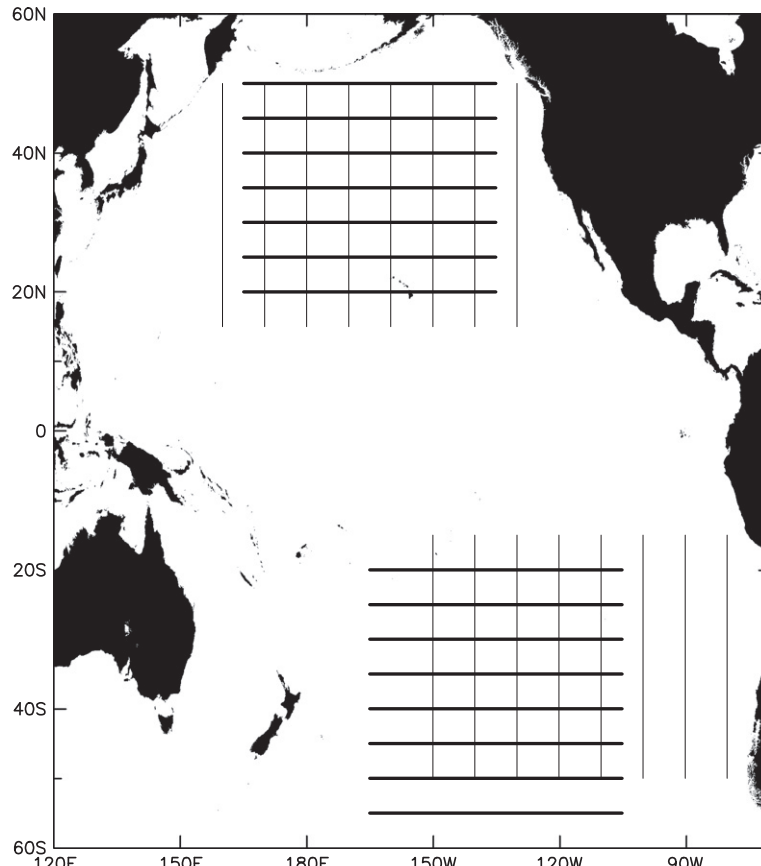


Fig. A2. The 15 zonal (thick lines) and 16 meridional (thin lines) sections along which the wavenumber spectra in Fig. 28 were computed.

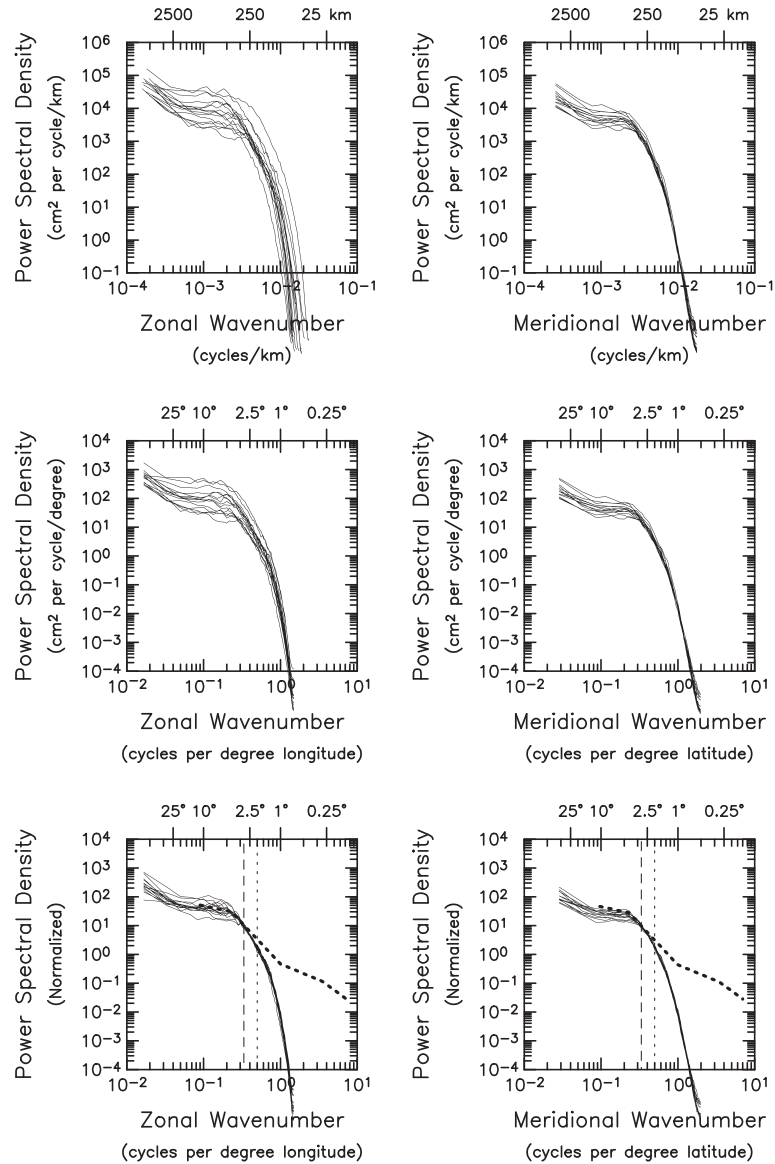


Fig. A3. Zonal (left panels) and meridional (right panels) wavenumber spectra computed from the SSH fields of the AVISO Reference Series analyzed in this study. To avoid interpretation complications from the small sidelobes of the filter transfer function for the interpolation onto a globally uniform $1/4^\circ$ latitude by $1/4^\circ$ longitude grid, the zonal wavenumber spectra were computed from the version of these SSH fields on the original $1/3^\circ$ Mercator grid. Because of the irregular latitudinal spacing in the Mercator grid, the meridional wavenumber spectra were computed from the AVISO $1/4^\circ \times 1/4^\circ$ gridded fields. The top panels show the spectra for wavenumber in cycles per km. The middle and bottom panels show the same spectra for wavenumber in cycles per degree of longitude (left) and latitude (right). The spectra in the bottom panels have been normalized so that each spectrum has the same variance integrated over wavelengths shorter than 3° (wavenumbers higher than 0.333 cycles per degree of longitude or latitude). The vertical dashed and dotted lines correspond to wavelengths of 3° and 2° , respectively, and the thick dotted lines in the bottom panels are the high-resolution wavenumber spectra computed by Stammer (1997) from the along-track T/P data, normalized here to match the centers of the clusters of spectra at 3° wavelengths. The flattening of the along-track spectrum at wavelengths shorter than 1° is the red-noise floor from T/P measurement noise (see Stammer, 1997).

wavelengths longer than roughly 300 km (wavenumbers smaller than 3.33×10^{-3} cycles per km), the zonal and meridional spectra have different variances, reflecting the wide range of dynamical regimes represented in the individual spectra. At shorter wavelengths (higher wavenumbers), the variances in all of the spectra drop steeply. The 16 meridional wavenumber spectra are tightly clustered at these higher wavenumbers. Although the zonal wavenumber spectra are less tightly clustered at wavelengths shorter than 300 km, the similarity of the shapes of the 15 individual spectra is striking and highly suggestive of the effects of filtering.

To see the effects of filtering more clearly, the wavenumber spectra are superimposed in the middle panels of Fig. A3 for wavenumber in units of degrees of longitude and latitude. There is no

change in the character of the meridional wavenumber spectra since the scaling between kilometers and degrees of latitude is the same everywhere. Because the scaling between kilometers and degrees of longitude varies as the cosine of latitude, the zonal wavenumber spectra for the wide range of latitudes in Fig. A2 change significantly when wavenumber is changed from cycles per km in the upper left panel to cycles per degree of longitude in the middle left panel. In particular, the individual zonal wavenumber spectra become tightly clustered at the higher wavenumbers corresponding to wavelengths shorter than about 3° .

The zonal and meridional wavenumber spectra thus decrease with increasing wavenumber in a consistent manner when wavenumber is displayed in units of cycles per degree of longitude or

latitude. For wavelengths shorter than about 1.5° , the slopes are steeper than -10 in the log-log plots in Fig. A3. This consistency is symptomatic of the “band-edge rolloff” of the filtering inherent in the AVISO objective analysis procedure. The spectra do not coincide exactly in the high-wavenumber regime because of the different total variances of SSH in the different dynamical regimes from which the spectra were computed. These different variances result in offsets between the spectral variances over the low wavenumbers (long wavelengths) that are adequately resolved in the AVISO Reference Series, thus resulting in different “starting points” for the band-edge rolloff at shorter wavelengths (higher wavenumbers).

When the spectra are adjusted to account for the geographical variability of the resolvable variance by normalizing each of the individual spectra to have the same variance over wavelengths shorter than 3° (bottom panels of Fig. A3), the 15 zonal wavenumber spectra and 16 meridional wavenumber spectra become nearly indistinguishable for wavelengths shorter than 3° (wavenumbers higher than 0.333 cycle per degree of longitude and latitude). This universality of the spectral characteristics of the SSH fields at high wavenumbers when adjusted for the different variance levels of SSH at the resolvable wavelengths lends very strong support to our interpretation of the observed spectral roll off at high wavenumbers as being caused by the filtering inherent in the objective analysis procedure.

The thick dotted line in the bottom panels of Fig. A3 is the global composite average normalized wavenumber spectrum derived from high-resolution along-track measurements of SSH by Stammer (1997), here adjusted to match our normalized spectra at a wavelength of 3° . The normalized wavenumber spectra computed here roll off more steeply than the along-track wavenumber spectrum at wavelengths shorter than 3° , which further demonstrates the filtering effects of the objective analysis procedure. [Note that the flattening of the along-track spectrum at wavelengths shorter than 1° is the red-noise floor from T/P measurement noise (see Stammer, 1997).]

It is thus apparent that features with wavelength scales shorter than about 3° are attenuated in the SSH fields of the AVISO Reference Series. The attenuation is essentially zero at 3° (the vertical dashed lines in Fig. A3) and increases monotonically to about a factor of 50 at a wavelength scale of 1° , compared with the Stammer (1997) spectrum. A reasonable definition of the implicit filter cutoff of the objective analysis procedure used to create the SSH fields of the AVISO Reference Series can be inferred from the half-power point (cf., CS03) of the steep rolloff at high wavenumbers in the spectra in Fig. A3, i.e., the wavelength at which the attenuation relative to the Stammer (1997) spectrum is about a factor of 2. This occurs at a wavelength of about 2° , indicated by the vertical dotted lines in Fig. A3.

We conclude that the filtering of the objective analysis procedure used to create the SSH fields of the AVISO Reference Series is approximately isotropic and geographically homogeneous over the regions shown in Fig. A2, when characterized in terms of degrees of longitude and latitude. Since these broad expanses of the North and South Pacific are representative of the range of conditions found throughout most of the global ocean, the filtering properties determined above for these regions are likely applicable globally in the SSH fields of the AVISO Reference Series. The wavelengths of the half-power filter cutoffs are about 2° in longitude by 2° in latitude.

An interpretation of the $2^\circ \times 2^\circ$ filter cutoff wavelengths in terms of the corresponding mesoscale eddy scale is desirable. It is evident from the composite average eddy profiles in Fig. 15 that, on average, the eddies in this dataset can be reasonably approximated for present purposes as axially symmetric Gaussian structures of the form

$$h(r) = A \exp\left(-r^2/L_e^2\right), \quad (\text{A.1})$$

where h is SSH, r is the radial distance from the center of the eddy, A is the eddy amplitude, and L_e is the e-folding scale for the eddy. The scale L_e that corresponds to a wavelength of 2° can be determined by least-squares fitting of the idealized form in Eq. (A.1) to the positive half of a cosine with 2° wavelength, yielding $L_e \approx 0.4^\circ$, i.e., approximately 1/5 of the 2° wavelength. Eddies with L_e shorter than about 0.4° (zonal scales of about 45 km at the equator, 40 km at 30° latitude, and 30 km at 50° latitude) have thus been filtered out in the SSH fields of the AVISO Reference Series.

An alternative argument in support of the above correspondence between the 2° wavelength filter cutoff and Gaussian features with e-folding scales of about 0.4° can be made as follows. The Fourier transform of the Gaussian spatial feature given by Eq. (A.1) is

$$H(k) = A\pi^{1/2}L_e \exp\left(-\pi^2L_e^2k^2\right), \quad (\text{A.2})$$

where k is the wavenumber. The Fourier transform of the Gaussian feature is thus itself a Gaussian in the wavenumber domain. The spectrum is proportional to the square of the Fourier transform. For the case of interest, the square of Eq. (A.2) that has a half-power point (the conventional characterization of a filter) at a wavelength of 2° corresponds to a Gaussian feature in space given by Eq. (A.1) with an e-folding scale of $L_e = 0.37^\circ$.

It is important to bear in mind that the amplitudes of eddies with e-folding scales between 0.4° and 0.6° (the latter corresponding to the value of L_e that approximates the positive half of a cosine with 3° wavelength) are attenuated by the AVISO objective analysis procedure, but by an amount that decreases with increasing scale. Only the eddies with e-folding scales larger than about 0.6° are unattenuated by the objective analysis procedure.

The standard deviation of SSH computed from the 16 years of SSH fields of the AVISO Reference Series is shown in the bottom panels of Fig. A1. The much more energetic variability compared with the SSH standard deviations in the other panels of Fig. A1 constructed from T/P data alone reveals the degree to which the SSH signals are attenuated by the large amount of spatial smoothing required to construct meaningful maps of SSH from the coarse ground track spacing of the T/P sampling pattern.

The $2^\circ \times 2^\circ$ smoothing of the SSH fields of the AVISO Reference Series is somewhat less than the $3^\circ \times 3^\circ$ resolution capability deduced by CS03 for SSH fields constructed from two altimeters, one in a 10-day repeat orbit and the other in a 35-day repeat orbit. The approach advocated by CS03 strives to minimize spatial and temporal inhomogeneity of interpolation errors. By these criteria, it is apparent in the bottom panels of Fig. A1 that spatial inhomogeneity of the standard deviation of SSH still exists in the AVISO Reference Series, suggesting that the $2^\circ \times 2^\circ$ smoothing is inadequate. The geographical pattern of this inhomogeneity coincides with the ground track pattern of the 10-day repeat altimeter, with locally high values centered on the crossovers and low values in the diamond centers. The limitations imposed by the coarse track spacing of the 10-day repeat altimeter on SSH fields constructed from the merged dataset are most clearly seen from the oscillatory structure of the zonal sections in the bottom right panel of Fig. A1.

The approximate $2^\circ \times 2^\circ$ smoothing of the SSH fields of the AVISO Reference Series thus appears to be not quite sufficient by the spatial homogeneity criteria of CS03. The oscillatory structure in the SSH standard deviation, with locally larger variability near the crossovers of the 10-day repeat ground tracks than near the diamond centers formed by the 10-day repeat ground tracks, is an indication of amplitude modulation as eddies propagate across regions of inhomogeneous resolution and mapping errors. The amplitude will be larger when the eddy is in well-sampled regions near the crossovers of the ground tracks of the 10-day T/P sampling pattern and smaller when the eddy is in the poorly sampled dia-

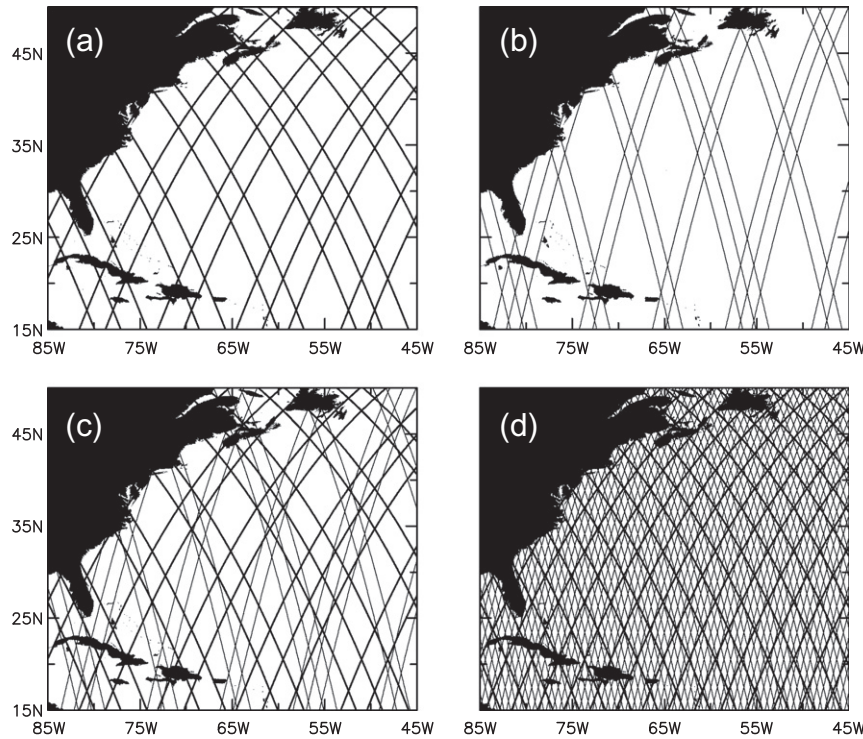


Fig. A4. The ground track patterns for the 10-day repeat orbit of T/P and its successors Jason-1 and Jason-2 (thick lines) and the 35-day repeat orbit of ERS-1 and its successors ERS-2 and Envisat (thin lines). (a) The ground tracks of the 10-day orbit during a representative 7-day period; (b) The ground tracks of the 35-day orbit during the same representative 7-day period; (c) The combined ground tracks of the 10-day orbit and the 35-day orbit during the 7-day period; and (d) The combined ground tracks of the 10-day orbit and the 35-day orbit during the full 35 days of the 35-day orbit.

mond-shaped regions between the crossovers. Such behavior can result in mislocation of eddy centroids and underestimation of eddy amplitudes in the SSH fields of the AVISO Reference Series. An example of such errors has been documented by Pascual et al. (2006) for an eddy in the North Atlantic. In extreme cases, such noise in the SSH fields can result in discontinuity of eddy trajectories obtained from the automated eddy identification and tracking procedure described in Appendices B.2–B.4.

The strong constraint imposed by the sampling pattern of the 10-day repeat altimeter on the resolution capability of the SSH fields of the AVISO Reference Series that combine measurements from a 10-day repeat altimeter and a 35-day repeat altimeter is perhaps surprising. The combined ground track patterns from the complete 10-day and 35-day repeat orbits of the two simultaneously operating satellites form the dense network of observations shown in the lower right panel of Fig. A4. The reason that the sampling pattern of the 10-day repeat altimeter limits the resolution of the merged dataset is evident from the other three panels of Fig. A4, which show the ground track patterns for a representative 7-day period from the 10-day repeat altimeter, the 35-day repeat altimeter and their combination. Over any particular 7-day period (the sample interval for the AVISO Reference Series), most of the complete ground track pattern is measured by the 10-day repeat altimeter. However, only 20% of the ground track pattern is mapped out over 7 days by the 35-day repeat altimeter. This inhomogeneous sampling is mitigated to some extent by temporal smoothing in the objective analysis procedure used by SSALTO/DUACS to construct SSH fields from the merged data. The observations within the 7-day window centered on the time of each SSH field are weighted more heavily than the observations outside of the 7-day window. The distribution of the combined observations from which any particular 7-day estimate of SSH is constructed is thus controlled largely by the sampling pattern of the 10-day repeat altimeter.

Appendix B. SSH-based eddy identification and tracking procedure

B.1. Overview of previous automated eddy identification procedures

The large number of eddies in the SSH fields of the AVISO Reference Series mandates the use of automated procedures for identification and tracking of individual eddies. The procedures that have been applied to altimeter data have built upon techniques developed previously for turbulence studies from numerical simulations. The various techniques strive to identify eddies in SSH, geostrophic velocity or variables related to the relative vorticity field that aim to isolate rotating structures with compact forms.

In the first application of automated eddy detection to altimeter data, Isern-Fontanet et al. (2003) implemented a procedure that is based on the Okubo–Weiss parameter originally used in turbulence studies as a measure of the relative importance of rotation and deformation in fluid flow (Okubo, 1970; Weiss, 1991). The Okubo–Weiss parameter is defined as

$$W = (\nu_x + u_y)^2 + (u_x - \nu_y)^2 - (\nu_x - u_y)^2 \quad (B.1a)$$

$$= 4(\nu_x u_y - u_x \nu_y) + (u_x + \nu_y)^2, \quad (B.1b)$$

where u and ν are the eastward and northward velocity components and subscripts denote partial differentiation. The terms in the first and second sets of parentheses in Eq. (B.1a) are the shear strain and normal strain, respectively, and the terms in the last set of parentheses are the relative vorticity. For the case of the horizontally nondivergent flow in the ocean, $u_x + \nu_y = 0$ and the Okubo–Weiss parameter Eq. (B.1b) reduces to

$$W = 4(\nu_x u_y - u_x \nu_y) = 4(\nu_x u_y + u_x^2). \quad (B.2)$$

Mathematically, the right side of Eq. (B.2) is equivalent to the determinant of the velocity gradient matrix multiplied by -4 . Eddies, for

which vorticity dominates strain, have $W < 0$ for both eddy polarities (cyclonic and anticyclonic). In the W -based methods, eddies are defined as connected regions where W lies below a specified negative threshold value.

Variants of the W -based method have been applied regionally to identify eddies in the Mediterranean Sea (Isern-Fontanet et al., 2003, 2004, 2006a,b), in the major eastern boundary currents (Morrow et al., 2004), and from model simulations of the circulation off the west coast of South America (Penven et al., 2005). A W -based method was applied globally to the SSH fields of the AVISO Reference Series by Chelton et al. (2007).

There are three significant problems with these W -based methods of eddy identification. The first is the need to specify a threshold value of W by which eddies are defined. No single value is optimal for the entire World Ocean. Setting the threshold too high can result in failure to identify small eddies, while a threshold that is too low can lead to a definition of eddies with unrealistically large areas that may encompass multiple vortices, sometimes with opposite polarities.

A second problem with the W -based method is that numerical estimates of W are highly susceptible to noise in the SSH fields. The velocity components must be estimated from SSH, h , by the geostrophic relations

$$u = -gf^{-1}h_y, \quad (\text{B.3a})$$

$$v = gf^{-1}h_x, \quad (\text{B.3b})$$

where g is the gravitational acceleration and f is the Coriolis parameter. The Okubo–Weiss parameter Eq. (B.2) then becomes

$$W = 4g^2f^{-2}(h_{xy}^2 - h_{xx}h_{yy}). \quad (\text{B.4})$$

The computation of W by Eq. (B.4) requires products of numerical second derivatives of the SSH field. Each differentiation and multiplication amplifies noise in the SSH field, which is non-negligible with the $2^\circ \times 2^\circ$ smoothing of the SSH fields of the AVISO Reference Series (Chelton and Schlax, 2003; Pascual et al., 2006; see also the discussion in Appendices A.1 and A.3 of Fig. A1). The problem is compounded at low latitudes by the factor f^{-2} that arises from the geostrophic relations (B.3a) and (B.3b).

To reduce the noise in W , Chelton et al. (2007) smoothed the SSH fields spatially with half-power filter cutoff wavelengths of 3° in longitude by 3° in latitude by 20 days prior to computing W , and then smoothed W with a $1.5^\circ \times 1.5^\circ$ spatial filter before thresholding W to define eddies. This two-stage smoothing was in addition to the approximate $2^\circ \times 2^\circ$ smoothing that is inherent in the SSH fields of the AVISO Reference Series (see Appendix A.3). The smoothing introduces a positive bias in the horizontal scales of the eddies and a negative bias in their amplitudes. Application of the method was further restricted to latitudes higher than 10° to limit the f^{-2} amplification of noise.

The third problem with the W -based method is that the interiors of eddies defined by closed contours of W do not generally coincide with closed contours of SSH. The misregistration of the two fields is often quite substantial. Indeed, eddies with opposing polarities sometimes occur within a single closed contour of W . While arguments can be made in favor of either W or SSH as a basis for defining an eddy, it is clear that estimation of eddy amplitude can be problematic for the W -based method.

After extensive experimentation, we have concluded that W is not well suited to eddy identification from noisy SSH. It is preferable to define eddies directly in terms of SSH, which eliminates the need for differentiation and thus avoids the noise problems described above.

The problem of defining eddies using thresholding remains. For example, Fang and Morrow (2003) implemented an SSH-based def-

inition of eddies using a threshold of ± 10 cm to identify the large eddies in the South Indian Ocean. Chaigneau and Pizzaro (2005) adopted a threshold of ± 6 cm to identify the smaller eddies in the region west of South America. Choosing an optimal threshold for global studies is difficult.

A threshold-free method of eddy identification has recently been applied by Chaigneau et al. (2008) to study eddies off the west coast of South America. An eddy was defined by closed streamline contours obtained using the “winding angle method” by tracing particle trajectories (streamlines) based on the geostrophic velocities computed from anomaly SSH. Streamlines that curve through an angle of $>2\pi$ radians are deemed closed, even if they do not intersect. The center points of all such “closed” streamlines are collected and clusters of center points are identified which correspond to single eddies. For each such cluster, the boundary of the eddy is defined by the outermost “closed” streamline.

A disadvantage of the Chaigneau et al. (2008) procedure is that it is based on the geostrophic velocity field obtained from derivatives of the SSH field. While less problematic than W -based methods that rely on products of doubly differentiated SSH, geostrophic estimates of velocity from SSH still amplify noise in the SSH fields, and the problem is compounded at low latitudes by an f^{-1} amplification factor.

B.2. A new SSH-based automated eddy identification procedure

The eddy identification procedure developed for this study strives to achieve threshold-free identification of eddies without the need for differentiation of the SSH field and with no smoothing beyond that inherent in the SSH fields of the AVISO Reference Series (see Appendices A.2 and A.3). For geostrophic flow around localized features such as eddies, streamlines correspond approximately to closed contours of SSH anomalies. This allows a simpler algorithm for eddy identification that is based on finding an outermost closed contour of SSH. The method is thus similar to the SSH method implemented by Fang and Morrow (2003) and Chaigneau and Pizzaro (2005), except that it obviates the need to specify a threshold contour of SSH as described below.

The eddy identification procedure described here was applied to the 16-year record (14 October 1992 through 31 December 2008) of the $1/4^\circ \times 1/4^\circ$ version of the SSH fields of the AVISO Reference Series described in Appendix A.2. We spatially high-pass filtered these SSH fields at each 7-day time step to remove coherent signals with wavelength scales larger than 20° of longitude by 10° of latitude. A map of anomaly SSH comprised of $1/4^\circ \times 1/4^\circ$ pixels is thus obtained at each 7-day time step. An example is shown in the bottom panel of Fig. 1.

For eddy identification, we make the following definitions. Each pixel has four nearest neighbors (to the north, south, east and west). Given a region defined by a set of connected pixels, a pixel is interior to the region if its four neighbors lie within the region. A point within the region is a local maximum (minimum) if it is interior and has SSH greater (less) than all of its nearest neighbors. We proceed to define an eddy as a simply connected set of pixels that satisfy the following criteria:

- (1) The SSH values of all of the pixels are above (below) a given SSH threshold for anticyclonic (cyclonic) eddies.
- (2) There are at least 8 pixels and fewer than 1000 pixels comprising the connected region.
- (3) There is at least one local maximum (minimum) of SSH for anticyclonic (cyclonic) eddies.
- (4) The amplitude of the eddy is at least 1 cm (see below).
- (5) The distance between any pair of points within the connected region must be less than a specified maximum.

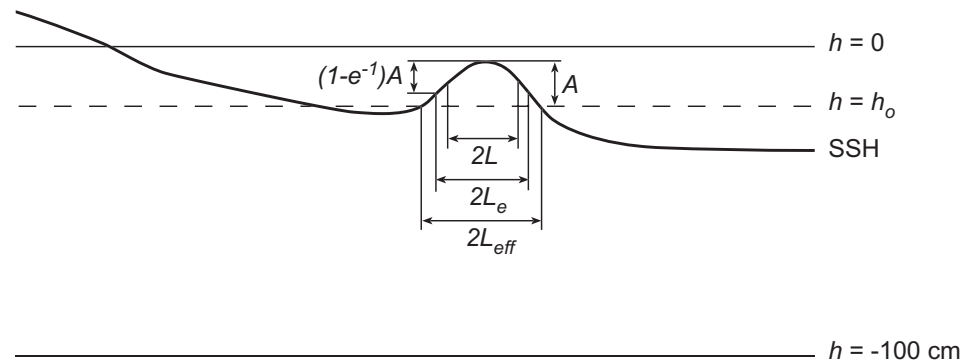


Fig. B1. A schematic summary of the automated eddy identification procedure for the case of an anticyclonic eddy (concave downward SSH) on a large-scale background negative SSH with larger magnitude than the amplitude of the eddy. The dashed line represents the basal value h_0 of SSH around the outermost closed contour of SSH defining the boundary of the eddy. The amplitude A and the radius scale variables L_{eff} , L_e and L as defined in Appendix B.3 are shown schematically for the eddy.

These five criteria can be used to define eddies once a threshold level of SSH is fixed. In order to make the eddy identification “threshold-free,” the SSH field is partitioned using a range of SSH thresholds from -100 cm to $+100 \text{ cm}$. Anticyclonic and cyclonic eddies are defined separately. For anticyclonic eddies, which are concave-down, the partitioning begins with an SSH threshold of -100 cm and proceeds upwards in increments of 1 cm until a closed contour of SSH that satisfies the above criteria is found (Fig. B1). At each thresholding step, the interior pixels of any eddies that are identified are removed from the set of pixels available for defining subsequent eddies. Cyclonic eddies (concave-up) are similarly identified, with the thresholding beginning at $+100 \text{ cm}$, and proceeding downwards. This procedure identifies the largest regions that satisfy the above five eddy definition criteria. Since all of the pixels that comprise each eddy satisfy criterion 1, the perimeter pixels (i.e., the non-interior pixels of the eddy) will approximate the outermost closed contour, which is approximately the streamline surrounding the eddy. Because the identification procedure considers SSH thresholds of both signs for both anticyclonic and cyclonic eddies, eddies can be identified even when superimposed on larger-scale background SSH features of either sign (Fig. B1).

The choice of 8 pixels in criterion 2 as the minimum area for defining an eddy was motivated by the conclusions of Appendix A.3 that the smoothing in the objective analysis procedure used by SSALTO/DUACS to construct the SSH fields of the AVISO Reference Series has a half-power filter cutoff of about 2° and thus attenuates features with radius scales L_e smaller than about 0.4° , where L_e is the e-folding scale of a Gaussian approximation for the eddy structure, see Eq. (A.1). The area of a circle with 0.4° radius is equivalent to that of 8 pixels with dimensions of $1/4^\circ \times 1/4^\circ$. Hence the choice of an 8-pixel cutoff for the minimum allowable areal extent of an eddy. With the tracking procedure described below in Appendix B.4, this cutoff minimum eliminates approximately $1/3$ of the eddies identified as closed contours of SSH with lifetimes of 4 weeks and longer.

Criterion 5 is imposed because closed contours on the outer flanges of eddies often enclose elongated features or broad ameba-like regions, often with multiple extrema, that do not resemble the usual notion of compact form for rotating vortices. Requiring that the maximum distance between any pairs of points within an eddy interior be less than a specified threshold usually allows identified eddies to be restricted to compact structures (see Figs. C2 and C3 and the related discussion in Appendix C). We have taken the maximum-distance threshold to be 400 km for latitudes above 25° , which is shown in Appendix C to be a good choice. To allow for the detection of low-latitude eddies and eddy-like features (e.g., tropical instability waves) that can have scales larger

than 400 km , the maximum distance criterion was increased linearly to 1200 km at the equator.

Using the above stepwise thresholding procedure with increments of 1 cm , eddies with amplitudes smaller than 1 cm are not retained. In principle, it is easy to reduce the increment to a value smaller than 1 cm , thus allowing the detection of eddies with smaller amplitudes. In practice, however, this often resulted in large, ameba-like eddy perimeters because the outermost “flanges” of eddies tend to be broad and relatively flat (see the composite eddy profiles in Fig. 15). An increment of 1 cm yields a good compromise between minimum resolvable eddy amplitude and well defined and compact eddy interiors.

The algorithm described above can yield eddies with more than one local extremum of SSH. This could occur because of multiple eddies in close proximity that are contained within a single outermost closed contour of SSH, or because of irregularity of the SSH structure within a single eddy from noise in the SSH fields. We attempted to separate, or split, multiple eddies by successive application of the algorithm. This splitting often resulted in undesirable characteristics of the tracked eddies, e.g., abrupt and large changes in the area of an eddy interior and the eddy amplitude from one time step to the next along its trajectory and false identification of short-lived, small-amplitude eddies. After much experimentation, the eddy splitting procedure was abandoned.

B.3. Definitions of eddy amplitude and scale

The amplitude of each anticyclonic eddy is defined as the difference $A = h_{\max} - h_0$ between the maximum SSH within the eddy, h_{\max} , and the average height value h_0 around the outermost closed contour of SSH that defines the eddy perimeter (see Fig. B1). Similarly, the amplitude of each cyclonic eddy is defined as the difference $A = h_0 - h_{\min}$ between h_0 and the minimum SSH within the eddy, h_{\min} . The amplitude of an eddy is thus a positive quantity for either polarity. The “basal value” h_0 of each eddy is estimated as the average SSH over the perimeter pixels of each eddy. Because of the discretization of the SSH field by the $1/4^\circ \times 1/4^\circ$ grid, the perimeter pixels do not generally all have the same value, especially when the SSH topography is steeply sloped around a portion or all of the eddy perimeter.

For tracking purposes (see Appendix B.4) the size of each eddy is characterized by the effective radius, L_{eff} , defined to be the radius of the circle that has the same area as the region within the eddy perimeter (Fig. B1).

We have adopted three definitions for eddy scale. One of these is an indirect estimate based on the axially symmetric Gaussian expressed as Eq. (A.1), which is a good approximation for the central $2/3$ of the average profile of the composite eddy in

Fig. 15. The e-folding scale L_e of the Gaussian approximation was estimated for each eddy by the radius of a circle whose area is equal to the area of the portion of the eddy interior lying above $h_{max} - (1 - e^{-1})A = h_0 + A/e$ for an anticyclonic eddy (Fig. B1) and below $h_{min} + (1 - e^{-1})A = h_0 - A/e$ for a cyclonic eddy. Since L_e is defined relative to the base h_0 that encompasses an area equivalent to that of a circle with radius L_{eff} , the e-folding scale L_e is effectively computed indirectly from L_{eff} .

For dynamical interpretation, the formulation in Eq. (A.1) for an axisymmetric Gaussian is more conveniently expressed as

$$h(r) = A \exp[-r^2/(2L^2)]. \quad (\text{B.5})$$

The second eddy scale $L = 2^{-1/2}L_e$ is a better characterization of the horizontal scale of an eddy than L_e since L is the radius at which the axial speed of an axisymmetric Gaussian eddy is maximum and hence the relative vorticity is zero. The e-folding scale L_e , and therefore L , are very highly correlated with the effective radius L_{eff} (see Fig. B2a), emphasizing the fact that L_e and L are computed indirectly from L_{eff} . On average, $L_e \approx 0.62L_{eff}$, and hence $L = 2^{-1/2}L_e \approx 0.44L_{eff}$.

Our third, and preferred, definition of eddy scale is a direct estimate based on the contour of SSH within the eddy interior around which the average geostrophic speed is maximum. This corresponds approximately to a contour of zero relative vorticity within the eddy, regardless of whether the eddy has a Gaussian shape. We calculated the average geostrophic speed around each of the SSH contours used in the thresholding procedure described in Appendix B.2. The speed-based definition of the eddy scale L_s is the radius of the circle that has the same area as the region within the closed contour of SSH with maximum average speed. An appealing aspect of the scale L_s is that it does not presuppose any particular form for the structure of the eddy. For an axially symmetric eddy with Gaussian shape, L_s would correspond to the scale $L = 2^{-1/2}L_e$ defined in Eq. (B.5) in terms of the e-folding scale L_e in the formulation in Eq. (A.1) for a Gaussian.

The relationship between L_s and L_{eff} is shown in Fig. B2b. On average $L_s \approx 0.70L_{eff}$, but the variability within each binned average is much larger than for the binned averages of L_e (and hence L) as a function of L_{eff} (Fig. B2a). On an eddy-by-eddy basis, the correlation between L_s and L_{eff} is thus not nearly as strong as between L_e and L_{eff} . This is not surprising since L_e is computed indirectly from L_{eff} as summarized above, whereas L_s is estimated directly from the SSH field within the eddy interior, independently of L_{eff} .

The relationships between L_s and L_e , and thus between L_s and $L = 2^{-1/2}L_e$, are shown in Fig. B2c, from which it is apparent that $L_s \approx 1.15L_e \approx 1.64L$ on average, but with large variability within

each binned average and hence only moderate correlation on an eddy-by-eddy basis. The fact that L_s is consistently so much larger than L is a clear indication of inadequacy of a Gaussian approximation for the eddy structures, in which case L_s and L would be equal, as noted above. It is shown in Section 5 that the most frequently occurring structure of the tracked eddies consists approximately of an axisymmetric quadratic profile of SSH within most of the radius L_s , thus resulting in L_s significantly larger than the scale L that would be obtained if the eddies had Gaussian shape.

B.4. Automated eddy tracking

After eddies were identified for each time step in the sequence of SSH maps by the algorithm described in Appendix B.2, an automated tracking procedure was applied to determine the trajectory of each eddy. The various automated tracking procedures that have been implemented differ in detail but are all similar in concept. As summarized briefly below, the tracking method applied here to the eddies identified based on SSH is essentially the same as that which we applied previously to eddies identified based on the Okubo–Weiss parameter W (Chelton et al., 2007).

The center location of each identified eddy is defined to be the centroid of SSH within the outermost closed contour of SSH. For each eddy identified at time step k , the eddies identified at the next time step $k+1$ are searched to find the closest eddy lying within a restricted search region. To reduce the risk of jumping from one track to another, the search area in the later map is restricted to the interior of an ellipse with zonally oriented major axis. The eastern extremum of the ellipse is 150 km from the current eddy center and the north–south semi-minor axis of the ellipse is 150 km. The western extremum of the ellipse is a distance d from the current eddy center, where d is never less than 150 km. In concert with the observed increase of propagation speeds with decreasing latitude, d is set to 1.75 times the distance that a long baroclinic Rossby wave would propagate in one 7-day time step based on the long Rossby wave phase speed computed for the location of the eddy from the Rossby radius of deformation obtained from Chelton et al. (1998). If the resulting value is less than 150 km, then d is set to 150 km.

For any particular reference eddy at time k , only eddies at time $k+1$ with amplitude and area that fall between 0.25 and 2.5 times those of the reference eddy are considered. These wide ranges of allowable amplitude and size variation from one time step to the next accommodate noise in the SSH fields. If such a nearest later-time eddy is found, it is associated with the trajectory of the refer-

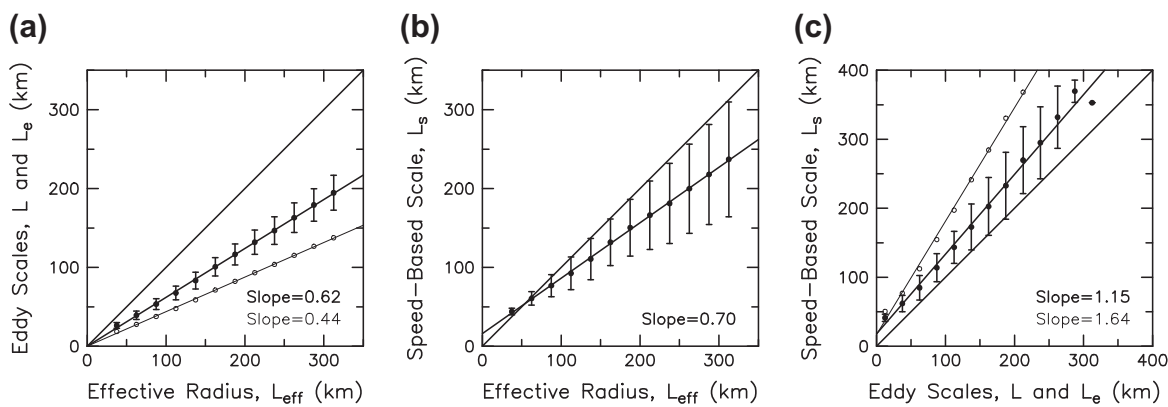


Fig. B2. Binned scatter plots computed from all of the eddies with lifetimes ≥ 16 weeks: (a) the Gaussian-based eddy scales L_e and $L = 2^{-1/2}L_e$, shown by the thick and thin lines, respectively, as a function of the effective radius L_{eff} , as defined in Appendix B.3; (b) the speed-based eddy scale L_s as a function of the effective radius L_{eff} ; and (c) the speed-based eddy scale L_s as a function of the Gaussian-based eddy scales L_e and L (thick and thin lines, respectively). The slopes of the least-squares fit lines through each set of binned averages are labeled in each panel, with lettering thickness coded to the associated line thickness in panels (a) and (c). The standard deviation of the points in each bin is shown by the vertical bars.

ence eddy up to time k . This process is repeated at each subsequent time step to obtain the entire trajectory of each eddy.

The “leftover eddies” at a time step k for which no associated eddy can be identified at time step $k+1$ may be the result of eddies temporarily “disappearing” for a variety of reasons related to sampling errors and measurement noise. An attempt was made to accommodate such problems and allow for the reappearance of a temporarily “lost” eddy. The tracking was repeated for the leftover eddies by looking ahead two and, if necessary, three time steps. If an identifiable later-time eddy was not found within three time steps, the trajectory of the leftover eddy was terminated at time k . When searching ahead more than one time step, the western extremum of the ellipse described above was extended to be n times d , where n is the number of time steps. Regardless of the number of time steps, d was restricted to be no more than 10° of longitude.

In practice, the results of this “look-ahead” procedure for tracking temporarily lost eddies were disappointing. The resulting eddy trajectories often jumped from one eddy to another. While this was clear visually from animations, our attempts to implement automated checks to prevent this from happening were mostly unsuccessful. It was eventually decided that losing track of eddies when they temporarily disappear is preferable to incorrectly patching together the trajectories of different eddies. The unfortunate result is that a “born-again” eddy that reappears after the altimeter sampling in the vicinity of the eddy improves is incorrectly identified by the tracking procedure as a new eddy. We are not able to say how often this occurs. From visual studies of animations, we do not feel that this is a major problem. In any case, we are confident that the eddy characteristics presented in this study (amplitude, scale, nonlinearity, and propagation speed and direction) are not strongly affected by misidentification of the start and end dates of eddy trajectories. It is clear, however, that the lifetimes of the eddy trajectories obtained by this procedure (Fig. 2) are generally a lower bound on the true eddy lifetimes. Conversely, eddy forma-

tion and termination rates estimated from these tracked eddies (Fig. 6) likely exceed the true values.

To reduce the risk of spurious eddies arising from noise in the SSH fields, eddies tracked as summarized above for time periods shorter than 4 weeks were eliminated from the eddy dataset. This 4-week lifetime is commensurate with the 35-day e-folding time scale of the Gaussian covariance function in the objective analysis procedure used to construct the SSH fields of the AVISO Reference Series (Appendix A.2). While we believe that most of the retained eddies with lifetimes of 4 weeks and longer are legitimate, a minimum lifetime threshold of 16 weeks was used for the analyses presented in Sections 3–7 in order to further alleviate concerns about imperfections in the automated eddy identification and tracking procedure. For the analyses presented in this study, the (x, y) locations of the centroids that define the trajectory of each eddy were smoothed using the loess smoother (Cleveland and Devlin, 1988; Schlax and Chelton, 1992; Chelton and Schlax, 2003) with a half-span of 6 weeks.

B.5. Comparisons between Okubo–Weiss-based eddies and SSH-based eddies

Rigorous comparison of the eddies identified by the method of Chelton et al. (2007) based on the Okubo–Weiss parameter W as summarized in Appendix B.1, and by the new SSH-based method summarized in Appendix B.2, is difficult since the two sets of eddies are defined in terms of different variables. In particular, the outer perimeters of eddies defined by the W -based method generally do not coincide with contours of SSH. The results of the two procedures can, however, be compared qualitatively.

The lifetime histograms and upper-tail cumulative histograms of the combined cyclones and anticyclones identified by the two procedures over the 10-year time period October 1992–August 2002 analyzed by Chelton et al. (2007) are shown in Fig. B3.

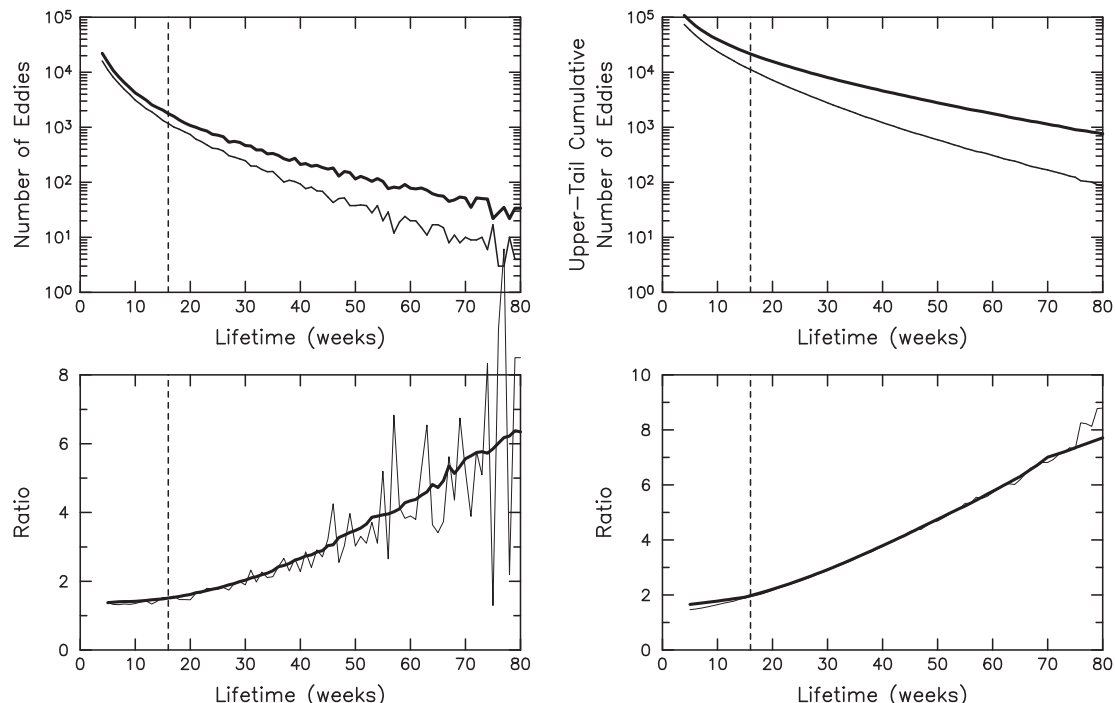


Fig. B3. Histograms (left) and upper-tail cumulative histograms (right) of the lifetimes of the tracked eddies obtained by the Okubo–Weiss-based method as implemented by Chelton et al. (2007) (thin lines in the upper panels) and the SSH-based method summarized in Appendices B.2–B.4 (thick lines in the upper panels) based on eddies tracked over the 10-year time period October 1992–August 2002 that was analyzed by Chelton et al. (2007). The ratios of the histogram values for the two methods are shown by the thin lines in the bottom panels. The thick lines represent 21-week running averages of the ratios at weekly intervals. The vertical dashed lines indicate the 16-week lifetime cutoff used for the analyses in Sections 3–7.

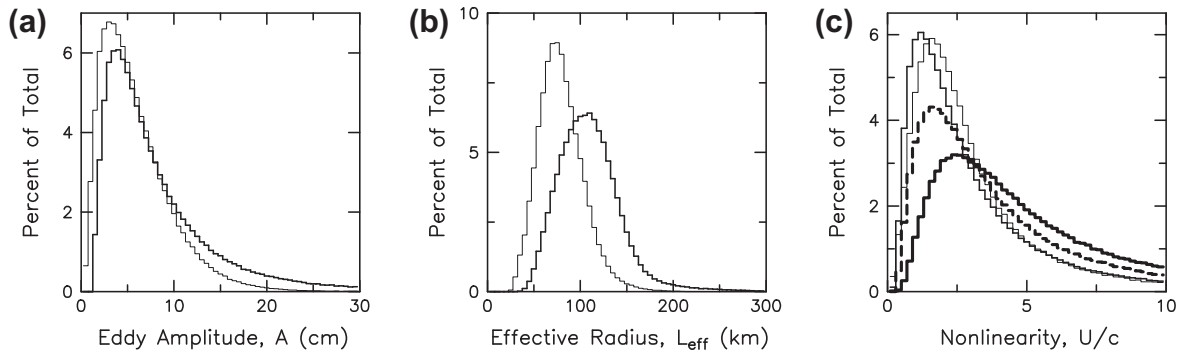


Fig. B4. Histograms of the eddy characteristics as defined in Appendix B.3 computed from all of the eddies with lifetimes ≥ 16 weeks identified by the Okubo–Weiss-based method as implemented by Chelton et al. (2007) (thin lines) and the SSH-based method summarized in Appendices B.2–B.4 (thicker lines): (a) amplitude, A ; (b) effective radius, L_{eff} ; and (c) the advective nonlinearity parameter, U/c . All histograms are based on eddies tracked over the 10-year time period October 1992–August 2002 that was analyzed by Chelton et al. (2007). In panel (c), the translation speed c at time k is computed as centered differences from the locations of the centroid of the eddy at times $k - 1$ and $k + 1$. The thin and medium-thickness lines in (c) are histograms of U/c determined from U defined conservatively as in Chelton et al. (2007) to be the mean geostrophic speed within the interiors of the Okubo–Weiss-based eddies and SSH-based eddies, respectively (see text). The thick dashed line in (c) is the histogram of U/c determined less conservatively but indirectly from the Gaussian-based definition of the characteristic fluid speed U . The thick solid line in (c) is the histogram of U/c determined directly by our preferred method from the speed-based estimate of U . (See text for details.)

Compared with the W -based method, the SSH-based procedure described in Appendix B.2 identifies increasingly more trackable eddies with increasing lifetime. For lifetimes longer than the 4-week minimum lifetime retained by the SSH-based method implemented as described in Appendices B.2–B.4, there is a cumulative total of 46% more eddies (108,541 compared with 74,456) during the 10-year time period analyzed by Chelton et al. (2007) (rather than the 16 years of data analyzed in this study). For the lifetimes of 16 weeks and longer analyzed in this study, the SSH-based method identifies about twice as many eddies in the 10-year data record (21,671 compared with 11,174). The difference increases to about a factor of 5 for eddies with lifetimes of a year and longer. The SSH-based procedure for eddy identification is thus much more effective than the W -based method used by Chelton et al. (2007).

Histograms of the eddy amplitudes and effective radii deduced from the two eddy datasets are shown in Fig. B4. Again bearing in mind that the two sets of eddies are defined in terms of different variables, the histograms are not directly comparable. In particular, the perimeters of the W -based eddies are defined by a threshold choice of W that does not map uniquely to any particular contour of SSH. It is seen from the figure that both the effective radii and the amplitudes of the W -based eddies are skewed toward smaller values than those of the SSH-based eddies. The difference is especially pronounced for the effective radii.

The larger effective radii and larger amplitudes of the SSH-based eddies analyzed in this study have only moderate impact on the estimated degree of nonlinearity of the eddies, as it was characterized by Chelton et al. (2007). In that study, nonlinearity was assessed from the advective nonlinearity parameter U/c , where c is the translation speed of the eddy at each time step and U is the characteristic particle speed within the eddy that was defined conservatively in that study to be the average geostrophic speed within the eddy interior, $U = gf^{-1}A/L_{\text{eff}}$, where g is the gravitational acceleration, f is the Coriolis parameter and A and L_{eff} are the amplitude and effective radius of the eddy, defined as in Appendix B.3 based on the SSH field within the W -based definition of the eddy perimeter. The U/c values using this same conservative definition of U are skewed toward somewhat smaller values for the SSH-based eddies analyzed in this study (see the thin and medium-thickness lines in Fig. B4c). This is mostly attributable to the larger effective radii of the SSH-based eddies (Fig. B4b).

The heavy dashed line in the distribution of U/c in Fig. B4c is for the SSH-based eddies when the characteristic particle speed U is defined to be the maximum geostrophic speed for the Gaussian

approximation of each eddy, i.e., $U = gf^{-1}\exp(-1/2)A/L$, where the scale L for which the axial speed is maximum in a Gaussian eddy is obtained indirectly from the effective radius L_{eff} and amplitude A of each eddy as described in Appendix B.3. This is a more dynamically appropriate definition of U than that used by Chelton et al. (2007) since regions within a Gaussian eddy where U/c exceeds 1 can be shown to delineate the portion of the eddy within which a parcel of fluid is trapped. It is evident from the figure that the eddies are more highly nonlinear by this less conservative measure of U/c .

The heavy solid line in Fig. B4c is the distribution of the advective nonlinearity parameter U/c for SSH-based eddies characterized as in Section 6.1 in terms of our preferred eddy scale L_s that is defined based on the area within the SSH contour with maximum average speed (see Appendix B.3) and defining U to be the corre-

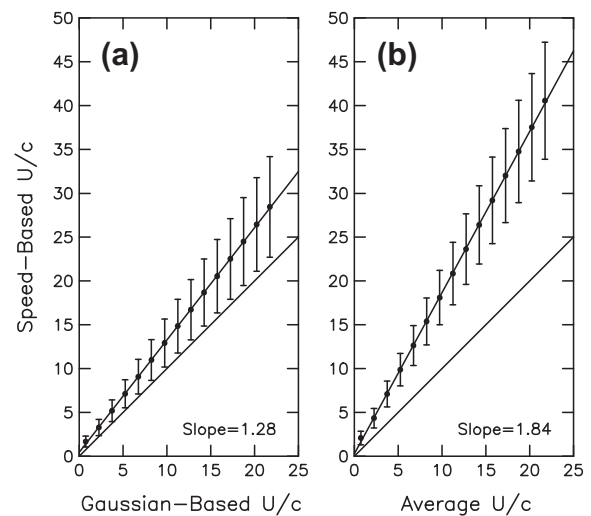


Fig. B5. Binned scatter plots computed from all of the eddies with lifetimes ≥ 16 weeks: (a) the advective nonlinearity parameter U/c determined directly by our preferred method from the speed-based estimate of U as a function of U/c obtained from the Gaussian-based speed U determined indirectly from the eddy amplitude A and scale L , and hence the effective eddy radius L_{eff} , as described in the text and (b) U/c from the speed-based estimate of U as a function of U/c estimated conservatively as in Chelton et al. (2007) based on the mean geostrophic speed within the eddy interiors. The slope of the least-squares fit line through the binned averages is labeled in each panel. The standard deviation of the points in each binned average is shown by the vertical bars.

sponding average speed. This direct measure of particle speed (as opposed to the indirect estimate based on L , and hence U , obtained from L_{eff}) results in even more highly nonlinear estimates of U/c . This accounts for the higher nonlinearity of the eddies in Section 6.1 compared with the nonlinearity reported by Chelton et al. (2007).

The relationships between U/c estimated here based on the value of U associated with the speed-based eddy scale L_s and the other two methods (U defined by the Gaussian-based estimate obtained from A and L as described above, and U defined as the average speed within the eddy interior as in Chelton et al., 2007) are shown by the binned scatter plots in Fig. B5. On average, the speed-based estimate adopted in this study yields an advective nonlinearity parameter U/c that is approximately 1.29 times larger than the Gaussian-based estimate and about 1.84 times larger than the conservative estimate of Chelton et al. (2007) based on the average speed within the eddy interior.

Appendix C. Assessment of the bias of the estimated eddy amplitudes

The adequacy of the estimated amplitudes of the eddies obtained from the automated procedure described in Appendices B.2 and B.3 can be assessed by considering first the hypothetical case of an isolated eddy in the absence of any background SSH associated with other eddies or with physical processes unrelated to the eddy of interest. By whatever detailed criteria are built into the algorithm, an automated eddy identification procedure will define the interior of an eddy based on some chosen perimeter. For our SSH-based procedure, this perimeter has a basal SSH value of h_0 defined as in Appendix B.3 to be the average value of SSH over the perimeter pixels. By our definition (see Appendix B.3), the amplitude A of the eddy is the magnitude of the height difference between h_0 and the extremum value h_{ext} of SSH within the defined interior of the eddy

$$A = |h_{\text{ext}} - h_0|. \quad (\text{C.1})$$

For this idealized case of an isolated eddy, the true amplitude of the eddy is

$$A_{\text{true}} = |h_{\text{ext}}|. \quad (\text{C.2})$$

The amplitude estimated by Eq. (C.1) in the automated procedure thus underestimates the true eddy amplitude given by Eq. (C.2)

for the hypothetical isolated eddy. The magnitude of the underestimate is

$$B = A_{\text{true}} - A \quad (\text{C.3a})$$

$$= |h_{\text{ext}}| - |h_{\text{ext}} - h_0| \quad (\text{C.3b})$$

$$= |h_0|. \quad (\text{C.3c})$$

Expressed as a fraction of the true amplitude of the eddy, the normalized bias of the estimated amplitude of this hypothetical isolated eddy is $B' = B/A_{\text{true}}$. Substituting (C.3a) for B and (C.2) for A_{true} yields an expression for this normalized bias in terms of the amplitude A estimated from the automated procedure,

$$B' = (A_{\text{true}} - A)/A_{\text{true}} = 1 - A/|h_{\text{ext}}|. \quad (\text{C.4})$$

With the unrealistic hypothetical assumption that each eddy exists in isolation, the average normalized bias of the estimated eddy amplitude in any particular region can be obtained by computing the average value of (C.4) over all of the eddies observed in that region. This is shown in Fig. C1 on a $1^\circ \times 1^\circ$ global grid for the eddies with lifetimes ≥ 16 weeks that are analyzed in this study. Globally, this estimate of the normalized bias in percent is $46 \pm 9\%$, indicating that

$$A \approx (0.54 \pm 0.09)A_{\text{true}}. \quad (\text{C.5})$$

While the range of uncertainty of this estimate is relatively narrow when expressed as a fraction or percentage of the true eddy amplitude, its actual magnitude in centimeters can be quite large in regions of energetic mesoscale eddies.

In reality, eddies of course do not exist in isolation. The scenario above for hypothetical isolated eddies therefore has limited applicability in the real ocean. Much of the SSH field outside of an eddy boundary consists of mesoscale variability in the form of distortions of the SSH field from eddy-eddy interactions that constitute the spectral continuum of the up-scale energy cascade. There is also larger-scale variability that is unrelated to the eddy field. Including these SSH structures as part of the eddies would result in features with non-compact form that do not resemble the usual notion of what constitutes a coherent eddy. The average normalized bias shown in Fig. C1 is thus an upper-bound estimate of the bias of the amplitudes A estimated by the automated procedure described in Appendices B.2 and B.3. As shown below, the actual bias of the estimated amplitudes of the compact structures that are of interest in this study is much smaller than is suggested by Fig. C1.

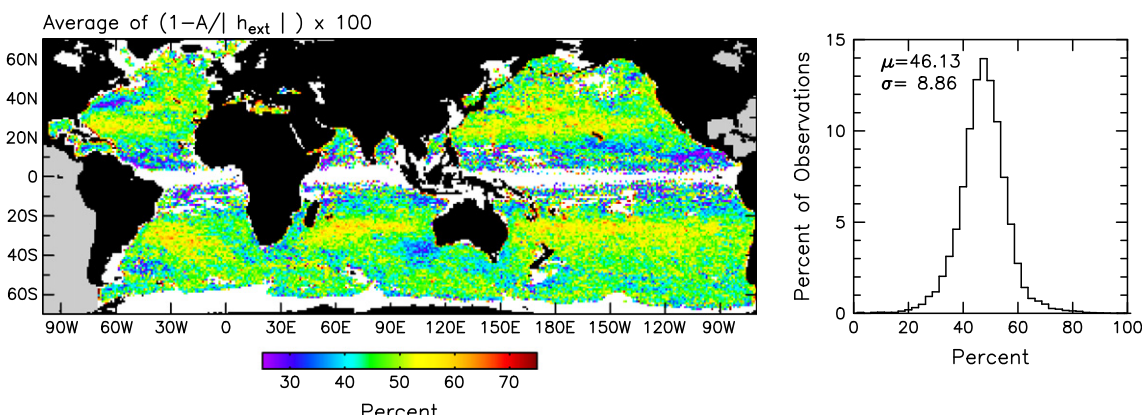


Fig. C1. A map of the upper-bound estimate for each $1^\circ \times 1^\circ$ area of the typical normalized bias B' given by Eq. (C.4) of eddy amplitudes A estimated by the procedure described in Appendix B.3 (see text for details), expressed in percent. A histogram of the gridded values in the map is shown in the right panel. The mean value μ and standard deviation σ of the histogram are labeled on the figure. For reasons discussed in the text, this figure is very misleading since the actual bias of the estimated amplitudes of the compact mesoscale features referred to in this study as "eddies" is generally only 1 or 2 cm and only occasionally more than that (see Figs. C2 and C3 and the associated discussion in the text).

Because of the 1 cm discretization of the step size in the partitioning of SSH to identify the outermost closed contour of SSH (see Appendix B.2), the amplitude A of compact mesoscale features can be biased low by as much as 1 cm from discretization error alone, as shown schematically in Fig. B1. However, even if the 1 cm discretization of the SSH contour defining an eddy were reduced by using a smaller discretization interval, some degree of

underestimation of the true amplitude of a compact feature and its areal extent, and hence its effective scale L_{eff} as defined in Appendix B.3, is unavoidable since the outermost closed contour of SSH may not encompass the entire eddy. Indeed, the outer boundary of an eddy is ill defined. The eddy scale variables L_{eff} , L_e and L (see Appendix B.3) are therefore lower-bound estimates of the horizontal scale of an eddy. The speed-based eddy scale L_s

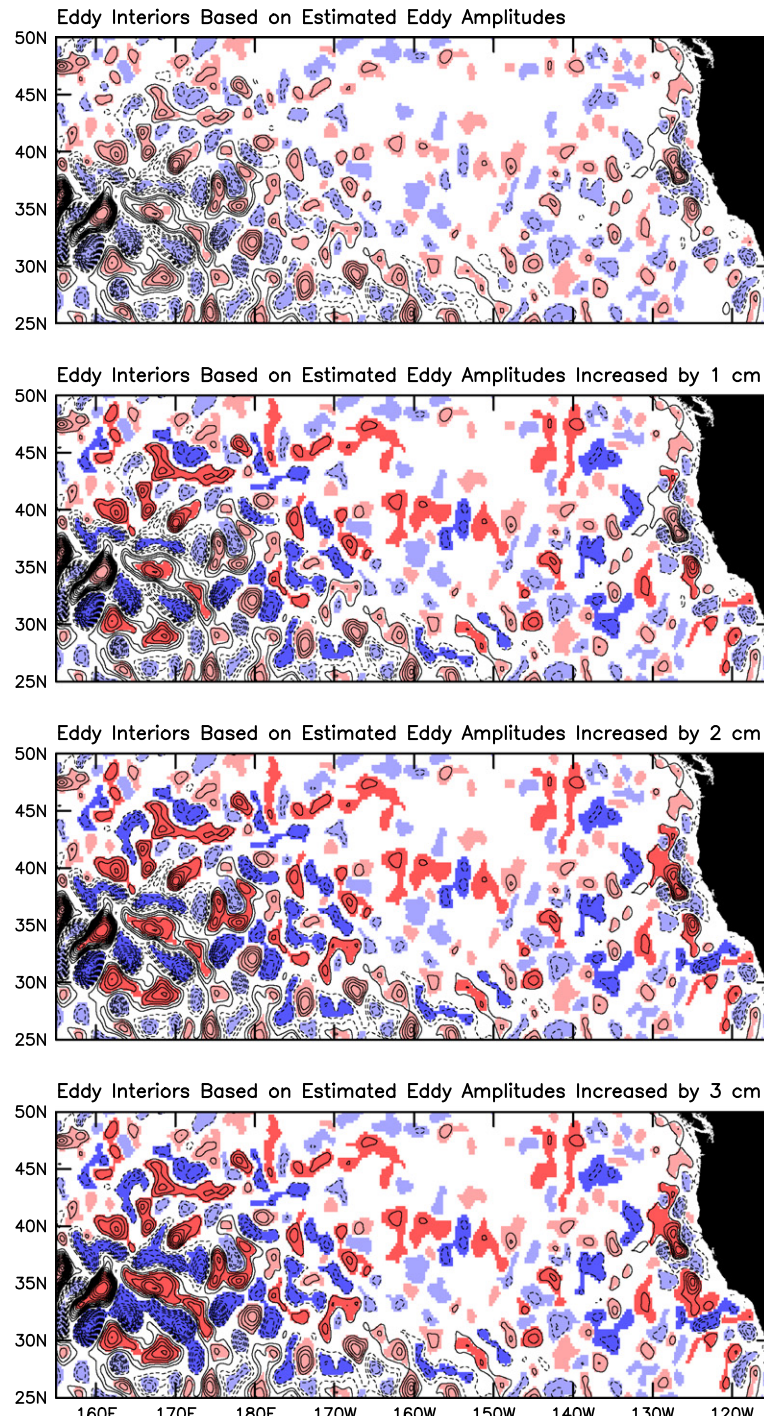


Fig. C2. Enlargements of a portion of the North Pacific from the global $20^\circ \times 10^\circ$ spatially high-pass filtered SSH field on 28 August 1996 shown in the bottom panel of Fig. 1. The top panel shows the anomaly SSH fields with the interiors of cyclonic and anticyclonic eddies as identified by the procedure described in Appendix B.2 shown as light blue and light red areas, respectively. The other panels show the same SSH field with the eddy interiors that are obtained when the perimeter of each eddy is adjusted to increase the amplitude of each eddy by 1, 2 and 3 cm (second, third and fourth panels, respectively). The dark blue and dark red areas represent the resulting expanded eddy interiors for which the threshold of maximum distance is exceeded in the eddy identification procedure described in Appendix B.2 (see text). In all panels, the SSH contour interval is 4 cm and the zero contour has been omitted for clarity.

(again see Appendix B.3) is somewhat less prone to such bias, unless the SSH contour with maximum speed coincides with the outermost closed contour defining the eddy. In such cases, the actual contour of maximum average speed may fall outside of the defined perimeter of the eddy.

The degree to which a compact mesoscale feature (an “eddy”) is encapsulated by the closed contour of SSH defining the eddy boundary depends on the precise definition that is adopted for what constitutes an eddy. Defining the full areal extent of an eddy unambiguously is problematic as discussed above. The difficulty in defining an outer boundary of an eddy can be demonstrated from a detailed analysis of the portion of the North Pacific region of the

spatially high-pass filtered SSH in the bottom panel of Fig. 1. The top panel of Fig. C2 shows the interiors of all of the eddies in this region that are identified from the SSH field on 28 August 1996 as described in Appendix B.2. Cyclones and anticyclones are shown as light blue and light red areas, respectively. It is apparent that nearly all of the compact features in the SSH field were identified as eddies. The eddy perimeter defined by the automated procedure sometimes encapsulates more than one individual eddy. An example is the anticyclonic feature centered near 38°N, 128°W off the coast of northern California that consists of two positive extrema. On the other hand, it is also apparent that there are numerous features for which the defined boundary does not encapsulate all of

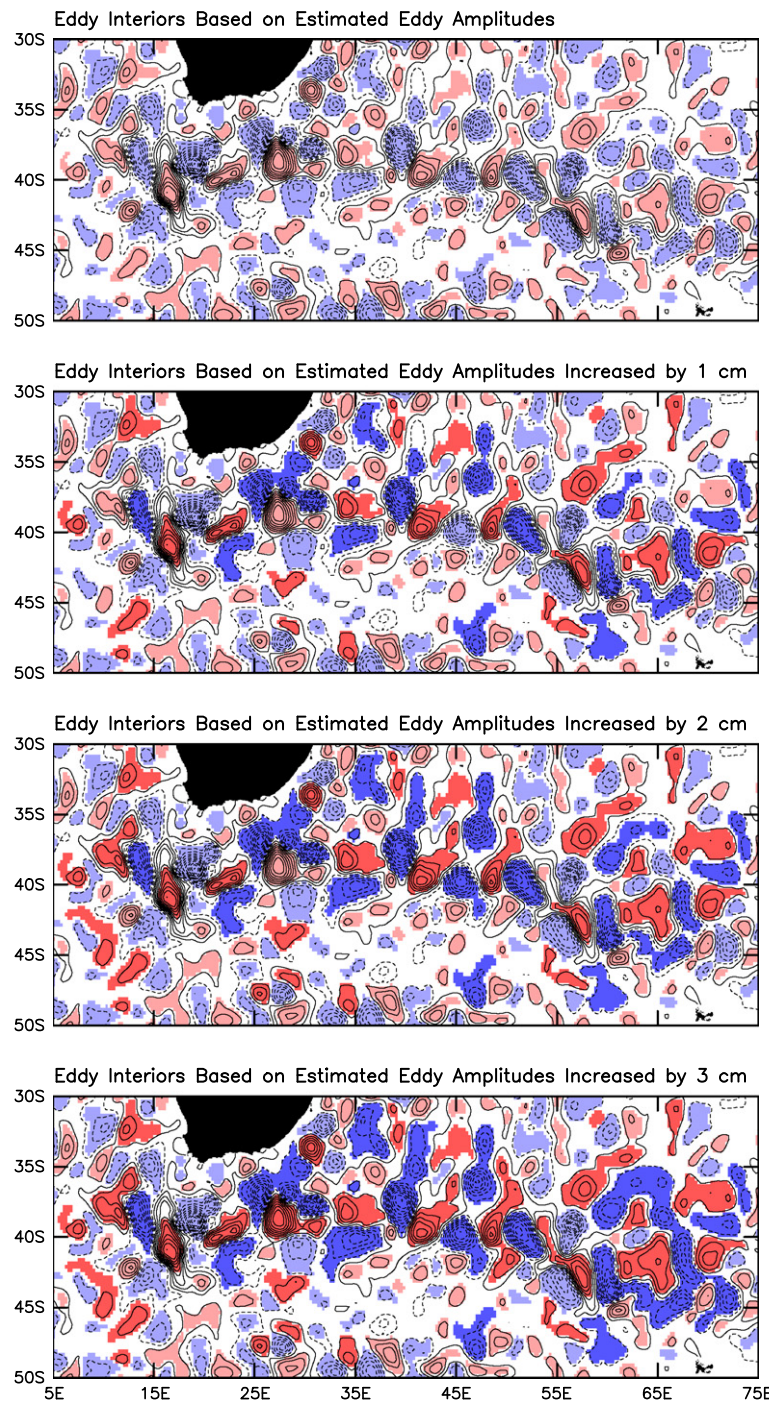


Fig. C3. The same as Fig. C2, except for a portion of the southwest Indian Ocean. The contour interval is 8 cm.

the compact structure of the eddy. This is especially common for the large eddies in the region 27°–40°N, 155°–180°E that is influenced by the Kuroshio Extension.

The results of adjusting the perimeter of each eddy to increase our estimated eddy amplitudes A by 1 cm, which is achieved by lowering the SSH threshold defining each anticyclone by 1 cm and raising it by that amount for each cyclone are shown in the second panel of Fig. C2. The dark blue and dark red areas indicate that the resulting expanded eddy interior failed criterion 5 in Appendix B.2 that bounds the maximum distance between any two points on the eddy boundary. In the Kuroshio Extension region of large-amplitude eddies, most of the expanded eddy boundaries encapsulate more of the SSH topography within the eddy while retaining compact forms but violating the maximum distance criterion. That our algorithm failed to define these eddy boundaries correctly is an indication that the 400 km maximum distance criterion imposed too strict a size constraint on these large-amplitude eddies. Increasing the eddy amplitudes by 1 cm was therefore beneficial in this region. Notable exceptions are the two zonally elongated cyclonic features centered near 37.5° between 157°E and 170°E, each of which consists of the merging of a pair of neighboring cyclones. Three similar cyclonic structures, except elongated meridionally, can be seen just east of the Dateline between 26°N and 38°N.

In the less energetic areas outside of the Kuroshio Extension region, a few of the expanded eddies in the second panel of Fig. C2 retain a compact form but most have very non-compact forms, sometimes encapsulating pairs of neighboring eddies and often encapsulating portions of the elongated interconnecting ridges and valleys between eddies that constitute the spectral continuum of the up-scale energy cascade. Three such features (two anticyclonic and one cyclonic) can be seen to the east and northeast of the above-noted merged pair of neighboring cyclones at the eastern end of the energetic portion of the Kuroshio Extension. Increasing the eddy amplitudes by 1 cm is therefore more often detrimental than beneficial in the less energetic regions.

Many of the eddy boundaries in the second panel of Fig. C2 do not expand when the thresholds are changed by 1 cm, either because the boundary of the eddy does not expand enough for the number of interior pixels to change, or because they already fill the outermost closed contour of SSH and satisfy the five criteria in Appendix B.2 that define the eddy boundary. The former occurs when the SSH topography is steeply sloped around the eddy perimeter. The latter occurs when the expanded contour intersects a continental boundary or the edge of the map and therefore cannot close.

It is apparent from the above discussion that increasing our estimates of the eddy amplitudes by only 1 cm yields mixed results; some of the eddy interiors in the Kuroshio Extension region are improved estimates of the compact forms of these large-amplitude eddies, but most of the expanded eddy boundaries outside of the Kuroshio Extension region have undesirable non-compact forms. Increasing the maximum distance criterion would yield better estimates of some of the eddies in the Kuroshio Extension region, but at the expense of yielding non-compact forms in the less energetic regions.

The results of increasing our estimated eddy amplitudes A by 2 cm are shown in the third panel of Fig. C2. In the Kuroshio Extension region, some of the expanded eddies encapsulate yet more of the SSH topography of the eddies while still maintaining compact forms but violating the maximum distance criterion. However, some of the expanded eddies in the Kuroshio Extension region become very non-compact. An example is the meandering anticyclonic structure centered near 35°N, 177°E that encapsulates several separate eddies and wraps around three sides of the cyclonic eddy to the north. Another example is the zonally elongated

anticyclonic feature centered near 30°N between 160°E and 170°E that encapsulates two large anticyclones. Outside of the Kuroshio Extension region, the above-noted anticyclonic feature off the California coast centered near 38°N, 128°W expanded into a very non-compact form that spans more than 7° of latitude. It is thus apparent that, except for a few of the large-amplitude eddies in the Kuroshio Extension region, increasing the estimated eddy amplitudes by 2 cm was generally more detrimental than beneficial.

The results of increasing the estimated eddy amplitudes A by 3 cm are shown in the bottom panel of Fig. C2. In this case, very few of the expanded eddies retain compact forms, even in the Kuroshio Extension region. Increasing the eddy amplitudes by this amount was therefore detrimental nearly everywhere.

The effects of increasing the eddy amplitudes summarized in detail above for the North Pacific are representative of the entire World Ocean. As another example in which the eddy amplitudes are much larger than in the Kuroshio Extension region, a portion of the Southwest Indian Ocean is shown in Fig. C3. Increasing the eddy amplitudes by 1 cm (second panel of Fig. C3) improved most of the eddy boundaries in the band of energetic eddies associated with the Agulhas Return Current. A notable exception is the large non-compact cyclonic feature immediately southeast of South Africa. In the less energetic areas outside of the Agulhas Return Current region, numerous expanded eddies have non-compact forms. Increasing the eddy amplitudes by 2 cm (third panel of Fig. C3) further improved some of the eddy boundaries in the Agulhas Return Current region but resulted in many eddies with non-compact forms elsewhere. Increasing the eddy amplitudes by 3 cm (bottom panel of Fig. C3) was detrimental nearly everywhere.

We conclude from Figs. C2 and C3 that the amplitudes A of the compact mesoscale features (“eddies”) estimated by the procedure summarized in Appendices B.2 and B.3 may sometimes be biased low by 1 or 2 cm in regions of very energetic mesoscale variability, but rarely by more than that. In the less energetic regions, increasing our amplitude estimates by even 1 cm results in many eddies with non-compact form. The estimated eddy amplitudes in these less energetic regions are thus usually biased by less than 1 cm.

We also conclude that the maximum distance criterion of our procedure successfully restricts the eddy boundaries to compact forms. This size constraint could be relaxed somewhat in regions where the mesoscale eddies are very energetic, thus retaining more of the SSH topography within the compact forms of the large eddies. For this global analysis, we have not attempted regional adjustments of the parameters of our eddy identification algorithm summarized in Appendix B.2. From the discussion above, this would generally change the eddy amplitudes by only 1 or 2 cm compared with the estimates obtained with the maximum distance criterion adopted for this study. Increasing the amplitudes by more than 2 cm would result in features nearly everywhere with non-compact forms that do not fit our assumed notion of what constitutes an eddy.

Residual SSH plateaus and the non-compact mesoscale structures in the SSH field after removing the eddy contributions to SSH are thus seen to be unavoidable consequences of the complex way in which eddies are interconnected to other eddies by the ridges and valleys of the spectral continuum of the up-scale energy cascade. Further complications arise from the fact that the compact eddies and non-compact mesoscale structures are embedded in larger-scale SSH variability that is unrelated to the eddy field.

References

- Antonov, J.I., Locarnini, R.A., Boyer, T.P., Mishonov, A.V., Garcia, H.E., <<http://www.nodc.noaa.gov/OC5/indprod.html>> 2006. World ocean atlas 2005, vol. 2:

- Salinity. In: Levitus, S. (Ed.), NOAA Atlas NESDIS 62, US Government Printing Office, Washington, DC, 182 pp.
- Arbic, B.K., Flierl, G.R., 2004. Effects of mean flow direction on energy, isotropy, and coherence of baroclinically unstable beta-plane geostrophic turbulence. *J. Phys. Oceanogr.* 34, 77–93.
- Batchelor, G.K., 1969. Computation of the energy spectrum in homogeneous two-dimensional turbulence. *Phys. Fluids* 12 (Suppl. II), 233–239.
- Birol, F., Morrow, R., 2001. Source of the baroclinic waves in the southeast Indian Ocean. *J. Geophys. Res.* 106, 9145–9160.
- Byrne, D.A., Gordon, A.L., Haxby, W.F., 1995. Agulhas eddies: a synoptic view using Geosat ERM data. *J. Phys. Oceanogr.* 25, 902–917.
- Calil, P.H.R., Richards, K.J., Jia, Y., Bidigare, R.R., 2008. Eddy activity in the lee of the Hawaiian Islands. *Deep-Sea Res., Part II* 55, 1179–1194.
- Chaigneau, A., Pizzaro, O., 2005. Eddy characteristics in the eastern South Pacific. *J. Geophys. Res.* 110, C06005. doi:[10.1029/2004JC002815](https://doi.org/10.1029/2004JC002815).
- Chaigneau, S., Gizolme, A., Grados, C., 2008. Mesoscale eddies off Peru in altimeter records: identification algorithms and eddy spatio-temporal patterns. *Prog. Oceanogr.* 79, 106–119.
- Challenor, P., Cipollini, G.P., Cromwell, D., 2001. Use of the 3D Radon transform to examine the properties of oceanic Rossby waves. *J. Atmos. Oceanic Technol.* 18, 1558–1566.
- Charney, J.G., 1971. Geostrophic turbulence. *J. Atmos. Sci.* 28, 1087–1095.
- Chelton, D.B., Schlax, M.G., 1994. The resolution capability of an irregularly sampled dataset: with application to GEOSAT altimeter data. *J. Atmos. Oceanic Technol.* 11, 534–550.
- Chelton, D.B., Schlax, M.G., 1996. Global observations of oceanic Rossby waves. *Science* 272, 234–238.
- Chelton, D.B., Schlax, M.G., 2003. The accuracies of smoothed sea surface height fields constructed from tandem altimeter datasets. *J. Atmos. Oceanic Technol.* 20, 1276–1302.
- Chelton, D.B., de Szoeke, R.A., Schlax, M.G., El Naggar, K., Siwertz, N., 1998. Geographical variability of the first-baroclinic Rossby radius of deformation. *J. Phys. Oceanogr.* 28, 433–460.
- Chelton, D.B., Schlax, M.G., Samelson, R.M., de Szoeke, R.A., 2007. Global observations of large oceanic eddies. *Geophys. Res. Lett.* 34, L15606. doi:[10.1029/2007GL030812](https://doi.org/10.1029/2007GL030812).
- Cleveland, W.S., Devlin, S.J., 1988. Locally weighted regression: an approach to regression analysis by local fitting. *J. Am. Stat. Assoc.* 83, 596–610.
- Colin de Verdierre, A., Tailleux, R., 2005. The interaction of a baroclinic mean flow with long Rossby waves. *J. Phys. Oceanogr.* 35, 865–879.
- Crawford, W.R., Cherniawsky, J.Y., Foreman, M.G.G., 2000. Multi-year meanders and eddies in the Alaskan stream as observed by TOPEX/Poseidon altimeter. *Geophys. Res. Lett.* 27, 1025–1028.
- Cushman-Roisin, B., 1994. Introduction to Geophysical Fluid Dynamics. Prentice Hall, New Jersey. 320 pp.
- Cushman-Roisin, B., Chassignet, E.P., Tang, B., 1990. Westward motion of mesoscale eddies. *J. Phys. Oceanogr.* 20, 758–768.
- Deans, S.R., 1983. The Radon Transform and Some of its Applications. John Wiley and Son, New York. 289 pp.
- de Szoeke, R.A., Chelton, D.B., 1999. The modification of long planetary waves by homogeneous potential vorticity layers. *J. Phys. Oceanogr.* 29, 500–511.
- Dewar, W.K., 1998. On “too fast” baroclinic planetary waves in the general circulation. *J. Phys. Oceanogr.* 28, 1739–1758.
- Ducet, N., Le Traon, P.-Y., Reverdin, G., 2000. Global high resolution mapping of ocean circulation from TOPEX/POSEIDON and ERS-1/2. *J. Geophys. Res.* 105, 19477–19498.
- Early, J., 2009. Mathematical Approaches to the Physics of Mesoscale Oceanography. Ph.D. Thesis, Oregon State University, 151 pp.
- Early, J.J., Samelson, R.M., Chelton, D.B., in press. The evolution and propagation of quasigeostrophic ocean eddies. *J. Phys. Oceanogr.*
- Fang, F., Morrow, R., 2003. Evolution, movement and decay of warm-core Leeuwin Current eddies. *Deep-Sea Res., Part II* 50, 2245–2261.
- Farrar, J.T., Weller, R.A., 2006. Intraseasonal variability near 10°N in the eastern tropical Pacific Ocean. *J. Geophys. Res.* 111, C05015. doi:[10.1029/2005JC002989](https://doi.org/10.1029/2005JC002989).
- Feng, M., Wijffels, S., 2002. Intraseasonal variability in the south equatorial current of the East Indian Ocean. *J. Phys. Oceanogr.* 32, 265–277.
- Flierl, G.R., 1978. Models of vertical structure and the calibration of two-layer models. *Dyn. Atmos. Oceans* 2, 341–381.
- Fu, L.-L., 2009. Patterns and velocity of propagation of the global ocean eddy variability. *J. Geophys. Res.* 114, C11017. doi:[10.1029/2009JC005349](https://doi.org/10.1029/2009JC005349).
- Fu, L.-L., Chelton, D.B., 2001. Large-scale ocean circulation. In: Fu, L.-L., Cazenave, A. (Eds.), *Satellite Altimetry and the Earth Sciences: A Handbook of Techniques and Applications*. Academic Press, pp. 133–169.
- Fu, L.-L., Ferrari, R., 2008. Observing oceanic submesoscale processes from space. *Eos, Trans. Am. Geophys. Union* 89, 488.
- Fu, L.-L., Qiu, B., 2002. Low-frequency variability of the North Pacific Ocean: the roles of boundary- and wind-driven baroclinic Rossby waves. *J. Geophys. Res.* 107, 1029/2001JC001131.
- Gill, A.E., 1974. The stability of planetary waves on an infinite beta-plane. *Geophys. Fluid Dyn.* 6, 29–47.
- Gill, A.E., 1982. *Atmosphere–Ocean Dynamics*. Academic Press. 662 pp.
- Gill, A.E., Green, J.S.A., Simmons, A.J., 1974. Energy partition in the large-scale ocean circulation and the production of mid-ocean eddies. *Deep-Sea Res.* 21, 499–528.
- Holland, C.L., Mitchum, G.T., 2001. Propagation of Big Island eddies. *J. Geophys. Res.* 106, 935–944.
- Hughes, C.W., Jones, M.S., Carnochan, S., 1998. Use of transient features to identify eastward currents in the Southern Ocean. *J. Phys. Oceanogr.* 103, 2929–2943.
- Isachsen, P.E., LaCasce, J.H., Pedlosky, J., 2007. Rossby wave instability and apparent phase speeds in large ocean basins. *J. Phys. Oceanogr.* 37, 1177–1191.
- Isern-Fontanet, J., Garcia-Ladona, E., Font, J., 2003. Identification of marine eddies from altimetric maps. *J. Atmos. Oceanic Technol.* 20, 772–778.
- Isern-Fontanet, J.E., Font, J., Garcia-Ladona, E., Emelianov, M., Millot, C., Taupier-Letage, I., 2004. Spatial structure of anticyclonic eddies in the Algerian basin (Mediterranean Sea) analyzed using the Okubo–Weiss parameter. *Deep-Sea Res.* 51, 3009–3028.
- Isern-Fontanet, J., Garcia-Ladona, E., Font, J., 2006a. Vortices of the Mediterranean Sea: an altimetric perspective. *J. Phys. Oceanogr.* 36, 87–103.
- Isern-Fontanet, J., Garcia-Ladona, E., Font, J., Garcia-Olivares, A., 2006b. Non-Gaussian velocity probability density functions: an altimetric perspective of the Mediterranean Sea. *J. Phys. Oceanogr.* 36, 2153–2164.
- Killworth, P.D., 1986. On the propagation of isolated multilayer and continuously stratified eddies. *J. Phys. Oceanogr.* 16, 709–716.
- Killworth, P.D., Blundell, J.R., 2004. The dispersion for planetary waves in the presence of mean flow and topography. Part I: analytical theory and one-dimensional examples. *J. Phys. Oceanogr.* 34, 2692–2711.
- Killworth, P.D., Blundell, J.R., 2005. The dispersion relation for planetary waves in the presence of mean flow and topography. Part II: two-dimensional examples and global results. *J. Phys. Oceanogr.* 35, 2110–2133.
- Killworth, P.D., Blundell, J.R., 2007. Planetary wave response to surface forcing and instability in the presence of mean flow and topography. *J. Phys. Oceanogr.* 37, 1297–1320.
- Killworth, P.D., Chelton, D.B., de Szoeke, R.A., 1997. The speed of observed and theoretical long extra-tropical planetary waves. *J. Phys. Oceanogr.* 27, 1946–1966.
- Kraichnan, R.H., 1967. Inertial ranges in two-dimensional turbulence. *Phys. Fluids* 10, 1417–1423.
- LaCasce, J.H., Pedlosky, J., 2004. The instability of Rossby basin modes and the oceanic eddy field. *J. Phys. Oceanogr.* 34, 2027–2041.
- Le Traon, P.-Y., Ogor, F., 1998. ERS-1/2 orbit improvement using TOPEX/POSEIDON: the 2 cm challenge. *J. Geophys. Res.* 103, 8045–8057.
- Le Traon, P.-Y., Gaspar, P., Bouysse, F., Makhmaraa, H., 1995. Use of TOPEX/POSEIDON data to enhance ERS-1 data. *J. Atmos. Oceanic Technol.* 12, 161–170.
- Le Traon, P.-Y., Nadal, F., Ducet, N., 1998. An improved mapping method of multisatellite altimeter data. *J. Atmos. Oceanic Technol.* 15, 522–534.
- Le Traon, P.-Y., Faugère, Y., Hernandez, F., Dorandeu, J., Mertz, F., Ablain, M., 2003. Can we merge Geosat follow-On with TOPEX/Poseidon and ERS-2 for an improved description of the ocean circulation? *J. Atmos. Oceanic Technol.* 20, 889–895.
- Liu, Z.Y., 1999. Planetary wave modes in the thermocline: non-Doppler-shift mode, advective mode, and Green mode. *Quart. J. Roy. Meteor. Soc.* 125, 1315–1339.
- Locarnini, R.A., Mishonov, A.V., Antonov, J.I., Boyer, T.P., Garcia, H.E., <<http://www.nodc.noaa.gov/OC5/indprod.html>>, 2006. World ocean atlas 2005, vol. 1: temperature. In: Levitus, S. (Ed.) NOAA Atlas NESDIS 61, US Gov. Printing Office, Washington, DC, 182 pp.
- Lumpkin, R., Flament, P., 2001. Lagrangian statistics of the central North Pacific. *J. Mar. Syst.* 29, 141–155.
- Maltrud, M.E., McClean, J.L., 2005. An eddy resolving global 1/10° ocean simulation. *Ocean Model.* 8, 31–54.
- Maximenko, N.A., Melnichenko, O.V., Niiler, P.P., Sasaki, H., 2008. Stationary mesoscale jet-like features in the ocean. *Geophys. Res. Lett.* 35, L08603. doi:[10.1029/2008GL033267](https://doi.org/10.1029/2008GL033267).
- McWilliams, J.C., Flierl, G.R., 1979. On the evolution of isolated, nonlinear vortices. *J. Phys. Oceanogr.* 9, 1155–1182.
- McWilliams, J.C., Brown, E.D., Bryden, H.L., Ebbesmeyer, C.C., Elliott, B.A., Heinmiller, R.H., Lien, Hua, B., Leaman, K.D., Lindstrom, E.J., Luyten, J.R., McDowell, S.E., Owens, W.B., Perkins, H., Price, J.F., Regier, L., Riser, S.C., Rossby, H.T., Sanford, T.B., Shen, C.Y., Taft, B.A., Van Leer, J.C., 1983. The local dynamics of eddies in the western North Atlantic. In: Robinson, A.R. (Ed.), *Eddies in Marine Science*. Springer-Verlag, Berlin, pp. 92–113.
- MODE Group, 1978. The mid-ocean dynamics experiment. *Deep-Sea Res.* 25, 859–910.
- Morrow, R., Birol, F., Griffin, D., Sudre, J., 2004. Divergent pathways of cyclonic and anti-cyclonic ocean eddies. *Geophys. Res. Lett.* 31. doi:[10.1029/2004GL020974](https://doi.org/10.1029/2004GL020974).
- Mouriño, B., Fernández, E., Etienne, H., Hernández, F., Giraud, S., 2003. Significance of cyclonic subtropical oceanic rings of magnitude (STORM) eddies for the carbon budget of the euphotic layer in the subtropical northeast Atlantic. *J. Geophys. Res.* 108, 3383. doi:[10.1029/2003JC001884](https://doi.org/10.1029/2003JC001884).
- Nof, D., Pichevin, T., Sprintall, J., 2002. “Teddies” and the origin of the Leeuwin Current. *J. Phys. Oceanogr.* 32, 2571–2588.
- Okubo, A., 1970. Horizontal dispersion of floatable particles in the vicinity of velocity singularities such as convergences. *Deep-Sea Res.* 17, 445–454.
- Osychny, V., Cornillon, P., 2004. Properties of Rossby waves in the North Atlantic estimated from satellite data. *J. Phys. Oceanogr.* 34, 61–76.
- Palacios, D.M., Bograd, S.J., 2005. A census of Tehuantepec and Papagayo eddies in the northeastern tropical Pacific. *Geophys. Res. Lett.* 32, L23606. doi:[10.1029/2005GL024324](https://doi.org/10.1029/2005GL024324).
- Parke, M.E., Born, G., Leben, R., McLaughlin, C., Tierney, C., 1998. Altimeter sampling characteristics using a single satellite. *J. Geophys. Res.* 103, 10513–10526.
- Pascual, A., Faugere, Y., Larnicol, G., Le Traon, P.-Y., 2006. Improved description of the ocean mesoscale variability by combining four satellite altimeters. *Geophys. Res. Lett.* 33. doi:[10.1029/2005GL024633](https://doi.org/10.1029/2005GL024633).

- Pedlosky, J., 1987. Geophysical Fluid Dynamics, second ed. Springer-Verlag.
- Penven, P., Echevin, V., Pasapera, J., Colas, F., Tam, J., 2005. Average circulation, seasonal cycle, and mesoscale dynamics of the Peru Current System: a modeling approach. *J. Geophys. Res.* 110, C10021. doi:[10.1029/2005JC002945](https://doi.org/10.1029/2005JC002945).
- Pingree, R., Sinha, B., 2001. Westward moving waves or eddies (storms) on the subtropical/Azores Front near 32.5°N? Interpretation of the Eulerian Currents and temperature records at moorings 155 (35.5°W) and 156 (34.4°W). *J. Mar. Syst.* 29, 239–276.
- Quarty, G.D., Buck, J.J.H., Stokosz, M.A., Coward, A.C., 2006. Eddies around Madagascar – the retroflection re-considered. *J. Mar. Syst.* 63, 115–129.
- Rhines, P.B., 1975. Waves and turbulence on a beta-plane. *J. Fluid Mech.* 69, 417–443.
- Rhines, P.B., 1979. Geostrophic turbulence. *Ann. Rev. Fluid Mech.* 11, 401–441.
- Robinson, A.R., 1983. Overview and summary of eddy science. In: Robinson, A.R. (Ed.), *Eddies in Marine Science*. Springer-Verlag, Berlin, pp. 3–15.
- Robinson, A.R., McWilliams, J.C., 1974. The baroclinic instability of the open ocean. *J. Phys. Oceanogr.* 4, 281–294.
- Samelson, R.M., 1992. Fluid exchange across a meandering jet. *J. Phys. Oceanogr.* 22, 431–440.
- Samelson, R.M., 2010. An effective- β vector for linear planetary waves on a weak mean flow. *Ocean Model.* 32, 170–174.
- Schlax, M.G., Chelton, D.B., 1992. Frequency domain diagnostics for linear smoothers. *J. Am. Stat. Assoc.* 87, 1070–1081.
- Schlax, M.G., Chelton, D.B., 1994a. Detecting aliased tidal errors in altimeter height measurements. *J. Geophys. Res.* 99, 12603–12612.
- Schlax, M.G., Chelton, D.B., 1994b. Aliased tidal errors in TOPEX/POSEIDON sea surface height data. *J. Geophys. Res.* 99, 24761–24775.
- Schlax, M.G., Chelton, D.B., 1996. Correction to “Aliased tidal errors in TOPEX/POSEIDON sea surface height data”. *J. Geophys. Res.* 101, 18451.
- Schlax, M.G., Chelton, D.B., 2008. The influence of mesoscale eddies on the detection of quasi-zonal jets in the ocean. *Geophys. Res. Lett.* 35, L24602. doi:[10.1029/2008GL035998](https://doi.org/10.1029/2008GL035998).
- Schouten, M., de Ruijter, W.P.M., van Leeuwen, P.J., Lutjeharms, J.R.E., 2000. Translation, decay and splitting of Agulhas rings in the southeastern Atlantic Ocean. *J. Geophys. Res.* 105, 21913–21926.
- Schouten, M.W., de Ruijter, W.P.M., van Leeuwen, P.J., Ridderinkhof, H., 2003. Eddies and variability in the Mozambique Channel. *Deep-Sea Res., Part II* 50, 1987–2003.
- Scott, R.B., Wang, F., 2005. Direct evidence of an oceanic inverse kinetic energy cascade from satellite altimetry. *J. Phys. Oceanogr.* 35, 1650–1666.
- Scott, R.B., Arbic, B.K., Holland, C.L., Sen, A., Qiu, B., 2008. Zonal versus meridional velocity variance in satellite observations and realistic and idealized ocean circulation models. *Ocean Model.* 23, 102–112.
- Smith, K.S., 2007a. Eddy amplitudes in baroclinic turbulence driven by nonzonal mean flow: Shear dispersion of potential vorticity. *J. Phys. Oceanogr.* 37, 1037–1050.
- Smith, K.S., 2007b. The geography of linear baroclinic instability in Earth's oceans. *J. Mar. Res.* 65, 655–683.
- Spall, M.A., 2000. Generation of strong mesoscale eddies by weak ocean gyres. *J. Mar. Res.* 58, 97–116.
- Stammer, D., 1997. Global characteristics of ocean variability estimated from regional TOPEX/POSEIDON altimeter measurements. *J. Phys. Oceanogr.* 27, 1743–1769.
- Stammer, D., 1998. On eddy characteristics, eddy transports, and mean flow properties. *J. Phys. Oceanogr.* 28, 727–739.
- Tai, C.-K., 2004. The resolving power of a single exact-repeat altimetric satellite or a coordinated constellation of satellites. *J. Atmos. Oceanic Technol.* 21, 810–818.
- Tai, C.-K., 2006. Aliasing of sea level sampled by a single exact-repeat altimetric satellite or a coordinated constellation of satellites: analytic aliasing formulas. *J. Atmos. Oceanic Technol.* 23, 252–267.
- Tai, C.-K., 2009. The temporal aliasing formulas for the tandem mission of Jason-1 and TOPEX/Poseidon. *J. Atmos. Oceanic Technol.* 26, 352–367.
- Tailleux, R., McWilliams, J.C., 2001. The effect of bottom pressure decoupling on the speed of extratropical, baroclinic Rossby waves. *J. Phys. Oceanogr.* 31, 1461–1476.
- Weiss, J., 1991. The dynamics of enstrophy transfer in two-dimensional hydrodynamics. *Physica D* 48, 273–294.
- Willett, C.S., Leben, R.R., Lavín, M.F., 2006. Eddies and tropical instability waves in the eastern tropical Pacific: a review. *Prog. Oceanogr.* 69, 218–238.
- Wunsch, C., 1981. Low-frequency variability of the sea. In: Warren, B.A., Wunsch, C. (Eds.), *Evolution of Physical Oceanography*. M.I.T. Press, Cambridge, MA, pp. 342–374.
- Yang, H., 2000. Evolution of long planetary wave packets in a continuously stratified ocean. *J. Phys. Oceanogr.* 30, 2111–2123.
- Yoshida, S., Qiu, B., Hacker, P., 2010. Wind-generated eddy characteristics in the lee of the island of Hawaii. *J. Geophys. Res.* 115, C03019. doi:[10.1029/2009JC005417](https://doi.org/10.1029/2009JC005417).
- Zamudio, L., Hurlbut, H.E., Metzger, E.J., Morey, S.L., O'Brien, J.J., Tilburg, C., Zavala-Hidalgo, J., 2006. Interannual variability of Tehuantepec eddies. *J. Geophys. Res.* 111, C05001. doi:[10.1029/2005JC003182](https://doi.org/10.1029/2005JC003182).